JOURNAL OF PETROLOGY | VOLUME 55 | NUMBER 7 | PAGES 1243–1286 | 2014 | doi:10.1093/petrology/egu024

Granulite-Facies Xenoliths in Rift Basalts of Northern Tanzania: Age, Composition and Origin of Archean Lower Crust

ADAM T. MANSUR[1], SHUKRANI MANYA[2], SEAN TIMPA[1] AND ROBERTA L. RUDNICK[1,2]*

[1]DEPARTMENT OF GEOLOGY, UNIVERSITY OF MARYLAND, COLLEGE PARK, MD 20742, USA

[2]GEOLOGY DEPARTMENT, UNIVERSITY OF DAR ES SALAAM, PO BOX 35052, DAR ES SALAAM, TANZANIA

RECEIVED AUGUST 12, 2013; ACCEPTED APRIL 11, 2014

Granulite xenoliths entrained within Quaternary rift basalts in northern Tanzania document the composition, equilibration conditions, age and petrogenesis of the present-day lower crust beneath the eastern margin of the Tanzanian Craton (Labait) and the adjacent Mozambique Belt (Lashaine and Naibor Soito). Mafic to intermediate Archean lithologies dominate throughout the suites (~2·66 Ga based on U–Pb zircon ages), demonstrating that deep-seated Archean lithosphere extends far to the east of the margin of the Tanzanian Craton within the Mozambique Belt. There is no evidence for significant additions to the crust via magmatic underplating since that time. Many of the lower crustal xenoliths share compositional similarities with lavas from the greenstone belts of the Tanzanian Craton, suggesting that they crystallized from similar magmas. Extreme depletions of highly incompatible elements (e.g. Cs, Rb, Th and U) in the granulites, relative to the lavas, coupled with unradiogenic $^{143}Nd/^{144}Nd$ (0·5114–0·5122) and $^{87}Sr/^{86}Sr$ (0·7040–0·7051), suggest that these depletions occurred coincident with or shortly after the rocks crystallized, possibly through partial melting associated with metamorphism. These samples may thus represent high-grade lower crustal complements to the greenstone belt lavas. Compared with the craton-margin samples, granulite xenoliths from within the Mozambique Belt record very high peak equilibration pressures at moderate temperatures (>1·2 to >1·7 GPa, 750–960°C, based on pseudosections), documenting their equilibration deep within thickened continental crust during the East African Orogeny, c. 560 Myr ago. These samples therefore offer an unusual window into the deepest reaches of the crust in a continental orogen. Despite the fact that the Mozambique Belt experienced significant crustal thickening followed by post-orogenic collapse, there is no evidence for loss of the deep lithosphere associated with these processes.

KEY WORDS: *granulite-facies xenoliths; major and trace element; Mozambique Belt; Tanzanian Craton; U–Pb zircon dates*

INTRODUCTION

Processes operating in the lower third of the continental crust, including partial melting, high-grade metamorphism, basaltic underplating and density foundering, play an important role in the differentiation of the crust, in regulating the transfer of material between the crust and mantle, and in providing heat for regional metamorphism. Understanding this part of the crust is therefore critical to answering questions about the formation and evolution of the continents, as well as the bulk composition of the continental crust.

Granulite-facies xenoliths, fragments of the lower continental crust transported to the surface via magmatism, offer an opportunity to constrain the age, origin and thermal history of the lower continental crust (e.g. Rudnick, 1992; Downes, 1993; Schmitz & Bowring, 2003*a*). Whereas a large number of studies have been carried out on lower crustal xenoliths from Proterozoic and younger regions [see summary by Rudnick & Gao (2003)], there are far fewer studies of xenoliths from Archean cratons, where

*Corresponding author. E-mail: rudnick@geol.umd.edu

© The Author 2014. Published by Oxford University Press. All rights reserved. For Permissions, please e-mail: journals.permissions@oup.com

Downloaded from http://petrology.oxfordjournals.org/ at University of Dar es Salaam on March 8, 2016

thick lithospheric keels inhibit deformation and generally preclude basaltic volcanism. Kimberlites and related ultrapotassic rocks erupted through cratons have proven the most fertile sources of cratonic crustal xenoliths to date, with studies from the Kaapvaal Craton (Rogers, 1977; Rogers & Hawkesworth, 1982; Huang *et al.*, 1995; Schmitz & Bowring, 2000, 2003*a*, 2003*b*), Wyoming Craton (Leeman *et al.*, 1985; Bolhar *et al.*, 2007; Blackburn *et al.*, 2012), Superior Craton (Zartman *et al.*, 2013), Baltic Shield (Kempton *et al.*, 1995, 2001; Markwick & Downes, 2000; Markwick *et al.*, 2001), Siberian Craton (Shatsky *et al.*, 2005; Koreshkova *et al.*, 2009) and the Dharwar Craton (Dessai & Vaselli, 1999; Dessai *et al.*, 2004). There are only two cratons where lower crustal xenoliths are reported to occur in alkali basalts: the North China Craton (Chen *et al.*, 2001; Liu *et al.*, 2001; Yu *et al.*, 2003; Zheng *et al.*, 2003; Huang *et al.*, 2004) and the Tanzanian Craton (Jones *et al.*, 1983*b*; Cohen *et al.*, 1984). In both of these cases, the basalts are manifestations of disruption of the cratonic lithosphere. In the North China Craton, Cenozoic basaltic magmatism followed decratonization that occurred in eastern China during the Mesozoic (e.g. Menzies *et al.*, 1993; Griffin *et al.*, 1998). In Tanzania, Quaternary basalts are a consequence of active rifting.

Granulite xenoliths were previously reported in several rift volcanoes erupted through the crust of northern Tanzania (Jones *et al.*, 1983*a*; Cohen *et al.*, 1984; Lee & Rudnick, 1999). This area includes the Tanzanian Craton and the polymetamorphic Mozambique Belt (Fig. 1). Lithosphere composing both the craton and metamorphic belt formed during the late Archean, but the two terranes record very different post-Archean histories. Whereas the Tanzanian Craton has not been significantly deformed since the Archean, the Mozambique Belt has experienced at least two cycles of collision and metamorphism, during the Usagaran (*c.* 2·0 Ga) and Neoproterozoic East African orogenies (e.g. Fritz *et al.*, 2005, 2009, and references therein), and also experienced metamorphism in the Archean, only 50–100 Myr after the majority of the crust formed (Johnson *et al.*, 2003). In addition, the whole area is currently experiencing extension and volcanism associated with the East African Rift (Dawson, 1992).

The goals of this study are to (1) document the composition and age of the lower crust in both the craton and the Mozambique Belt, (2) determine the processes by which the lower crust formed and compare the lower crustal history between these two contrasting sections of Archean crust, and (3) determine what effects, if any, the East African Rift is having on the deep crust in this region. Accordingly, we have undertaken a comprehensive study of granulite-facies xenoliths that occur in rift-related basalts in northern Tanzania. Using a broad array of techniques—including thermobarometry, pseudosection construction, U–Pb zircon dating, and whole-rock major-element, trace-element and Sr–Nd isotope geochemistry—we show that both sections of lower crust are underlain by intermediate to mafic rocks that formed in the Archean as crystallized magmas and their cumulates, including anorthosite. Very high pressures recorded in the granulites from the Mozambique Belt suggest their residence near the bottom of an orogenically thickened crust during the Neoproterozoic. We see no evidence for magmatic additions to the crust, nor for removal or thinning of the lower crust associated with either the present-day rift or Proterozoic orogeny.

GEOLOGICAL SETTING

The granulite xenoliths studied here are derived from both the Tanzanian Craton and from within the Neoproterozoic Mozambique Belt, which formed in the East African Orogeny (Fig. 1). We review the geology of these two regions in order.

The Tanzanian Craton formed during the late Archean (2·5–2·8 Ga). Granite–greenstone belts that crop out in the northern half of the craton include the Sukumaland Belt (emplaced *c.* 2820 Ma, Borg & Krogh, 1999; Manya & Maboko, 2003, 2008*b*; Kabete *et al.*, 2012, and references therein), the Iramba–Sekenke Belt (*c.* 2740 Ma, Manya & Maboko, 2008*a*), and the Musoma–Mara Belt (*c.* 2670 Ma, Manya *et al.*, 2006) (Fig. 1). Granitic magmatism is roughly synchronous in each belt (2550–2690 Ma) and is thought to reflect final stabilization of the craton via production of buoyant, felsic rocks (Manya & Maboko, 2003). Volcanic rocks in the greenstone belts are geochemically diverse and have been interpreted as forming in both arc (Musoma–Mara: Manya *et al.*, 2007; Mtoro *et al.*, 2009) and back-arc settings (Sukumaland and Iramba–Sekenke: Manya, 2004; Manya & Maboko, 2008*a*).

The Tanzanian Craton is underlain by a $\geq$150 km thick (Ritsema *et al.*, 1998; Lee & Rudnick, 1999; Weeraratne *et al.*, 2003) refractory, lithospheric keel that formed *c.* 2·8 Ga (Chesley *et al.*, 1999). This keel may have allowed the craton to resist post-Archean tectonic deformation (e.g. Brazier *et al.*, 2000). The cratonic crust is ~39 km thick (Last *et al.*, 1997; Tugume *et al.*, 2012), which is similar to the global average for the continental crust (41 km, Christensen & Mooney, 1995) and Archean shields (43 ± 6 km, Rudnick & Fountain, 1995). The lowermost crust exhibits high S-wave velocities (up to 4·1 km s^{-1}), suggesting a mafic bulk composition (Julia *et al.*, 2005).

To the east of the Tanzanian Craton lies the Proterozoic Mozambique Belt, which extends eastward to the continental margin (Fig. 1). The Mozambique Belt consists of high-grade rocks produced during the Usagaran (*c.* 2·0 Ga) and East African (*c.* 640 Ma) orogenies. The Usagaran Belt, which lies at the southeastern border of the craton, is interpreted to have formed from juvenile arc crust that amalgamated through strike-slip tectonics around 2·0 Ga (Möller *et al.*, 1995; Fritz *et al.*, 2005).

Downloaded from http://petrology.oxfordjournals.org/ at University of Dar es Salaam on March 8, 2016

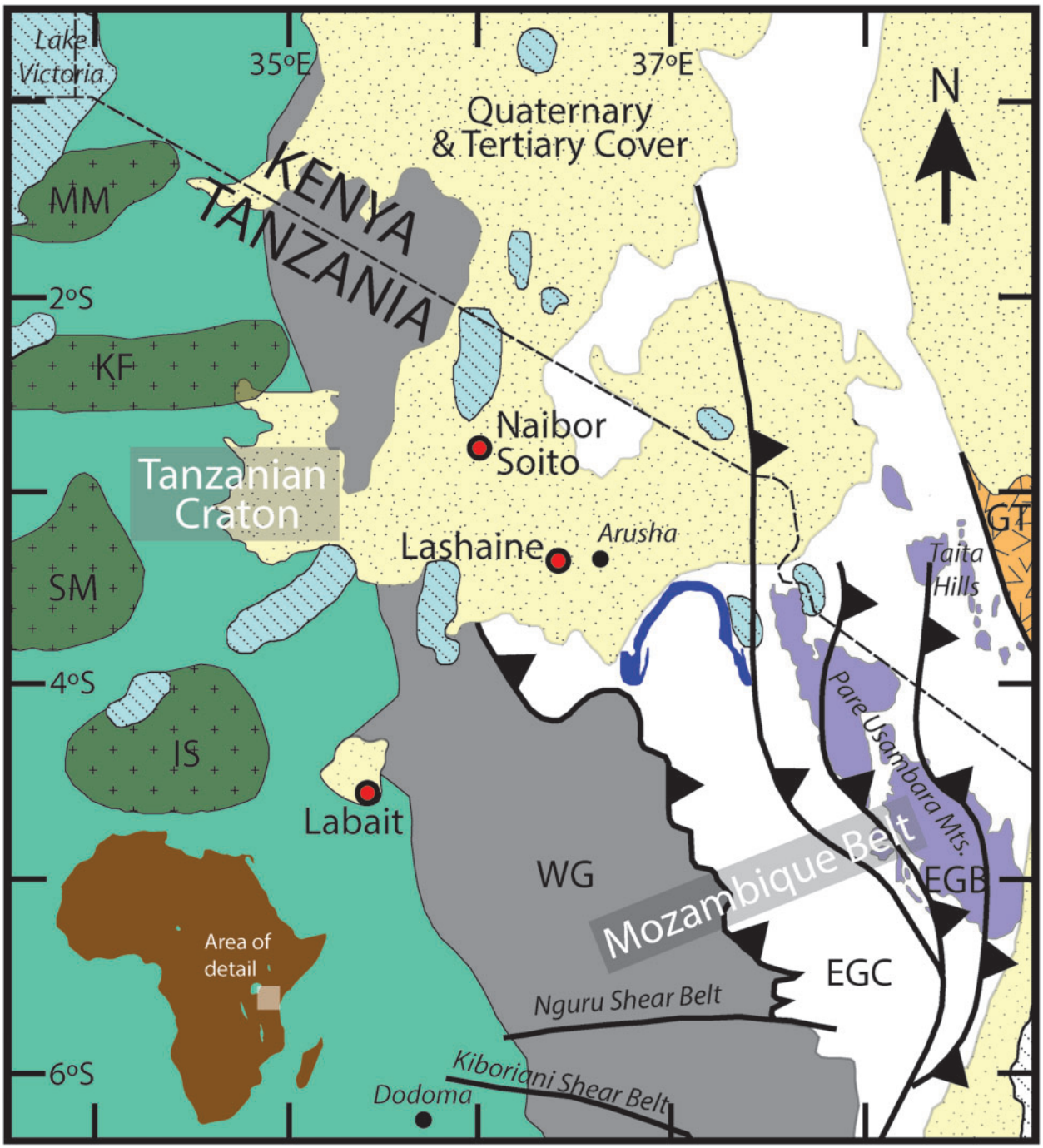


Fig. 1. Geological sketch map of Tanzania showing the location of the Tanzanian Craton (shades of green), Quaternary and Tertiary lavas and sediments (yellow), and the Mozambique Belt (gray, white, and purple). The latter consists of the Western Granulites (WG, dark gray), which are in fault contact with the Eastern Granulite Cover (EGC, white). The blue outcrop to the SE of Arusha consists of folded marble units. Outcrops of Eastern Granulite Basement (EGB, purple) occur in the Taita Hills, Kenya and the Pare-Usambara Mountains, Tanzania. GT (brown) is the Galana Terrane. General geological features after Fritz *et al.* (2009) and locations of greenstone belts (darker green in the craton) after Manya & Maboko (2008*a*). Greenstone belts: MM, Musoma–Mara; KF, Kilimafedha; SM, Sinyanga–Malita; IS, Iramba–Sekenke. The Sukumaland and Geita Greenstone Belts are located to the west of this map, directly south of the western portion of Lake Victoria. Locations of lower crustal xenolith suites (Naibor Soito, Lashaine and Labait) investigated here are shown as red circles.

Downloaded from http://petrology.oxfordjournals.org/ at University of Dar es Salaam on March 8, 2016

Although the northernmost extent of the Usagaran Belt is poorly known, the 2·0 Ga event extends at least as far north as Dodoma (Thomas *et al.*, 2013) (Fig. 1), but has not yet been recognized in metamorphic rocks of northern Tanzania (Tenczer *et al.*, 2014).

Most high-grade rocks in central and northern Tanzania are part of the East Africa Orogen, a 6000 km long metamorphic belt that marks a zone of continent–continent collision and a major suture in the Gondwana supercontinent (Stern, 1994, and references therein). Peak metamorphism across this orogen was diachronous from 750 to 540 Ma, with most Tanzanian rocks recording metamorphism at *c.* 640–540 Ma. In Tanzania, the orogen is divided into the Western and Eastern Granulites based on protolith age and pressure–temperature (P–T) path (e.g. Fritz *et al.*, 2005, 2009, and references therein) (Fig. 1).

The Western Granulites consist of Archean crust (2·5–2·9 Ga) reworked at amphibolite- to granulite-facies conditions (e.g. Thomas *et al.*, 2013). Syn-orogenic magmatism is absent and mineral reactions suggest a clockwise P–T path consistent with crustal thickening (e.g. Fritz *et al.*, 2009, and references therein). Although not determined over a wide area, peak metamorphism appears to have occurred at *c.* 540–565 Ma (Maboko, 2000; Cutten *et al.*, 2006; Blondes *et al.*, in preparation). In particular, Blondes *et al.* reported a highly precise $^{206}Pb/^{238}U$ thermal ionization mass spectrometry (TIMS) age for concordant metamorphic monazite from an Archean orthogneiss xenolith of 565 ± 1 Ma, which they took to mark peak metamorphism in the Western Granulites.

The Eastern Granulites consist of both Archean and younger meta-igneous rocks formed at mid-crustal depths in volcanic arcs located east of the craton margin prior to the Neoproterozoic collision. Protoliths of most of the Eastern Granulites are similar in age to juvenile material elsewhere in the East African Orogen (*c.* 700–1000 Ma). Metamorphic grade is higher in the Eastern Granulites than in the Western Granulites, which Fritz *et al.* (2005) interpreted to reflect westward propagation of thrust sheets onto the craton (as seen in the Eastern Granulites Cover in Fig. 1), accompanied by hinterland extension to expose the Eastern Granulites. Peak metamorphism was diachronous, ranging from 610 to 655 Ma (Möller *et al.*, 2000; Tenczer *et al.*, 2006), and probably occurred at the base of an antecedent arc, prior to final amalgamation of Gondwana, which occurred at *c.* 550 Ma based on paleomagnetic evidence (Meert *et al.*, 1995).

Like that of the Tanzanian Craton, the crust of the Mozambique Belt is ~38 km thick (Tugume *et al.*, 2012) and exhibits high velocities in the lower crust, which are interpreted to reflect a mafic composition (Julia *et al.*, 2005). The mantle lithosphere, as sampled by peridotite xenoliths, is refractory (Dawson & Smith, 1988; Rudnick *et al.*, 1993, 1994; Gibson *et al.*, 2013) and has Archean Re-depletion Os model ages (Burton *et al.*, 2000; J. Chesley, unpublished data). Based on the position of an S-wave low-velocity zone, the thickness of the lithosphere in the Mozambique Belt varies from 90 to 150 km (Julia *et al.*, 2005).

The variable thickness of the Mozambique Belt lithosphere may reflect incipient thinning associated with the East African Rift. The rift propagated into contact with the northern margin of the Tanzanian Craton by *c.* 12 Ma, splitting into western and eastern branches localized, for the most part, in the relatively weak crust of the metamorphic belts that border the craton (Dawson, 1992; Ritsema *et al.*, 1998; Nyblade & Brazier, 2002). Recent volcanic activity is characterized by eruptions of alkali-rich lava from small tuff cones and craters (Dawson, 1992). The lower crustal xenoliths described in this paper were collected from three tuff cones from the eastern branch of the rift, including Labait on the craton margin, and Lashaine and Naibor Soito within the Mozambique Belt (Fig. 1).

SAMPLES

Granulite xenoliths were selected for study with the aim of examining the range of compositions and rock types present at each locality. Samples from all three localities show evidence of mineral breakdown and alteration, including the formation of kelyphite on garnet (making garnet crystals appear black in plane-polarized light) and the formation of brown glass and/or zeolites along plagioclase grain boundaries. These are features associated with the entrainment and rapid ascent in the host basalts.

The mineralogy and texture of each sample is summarized in Table 1. Modal mineralogies, estimated by point counting for all of the samples for which geochemistry was determined, are provided in Table 2. Photographs of all Labait and Naibor samples, taken in the field, are provided in Fig. K of the electronic appendix.

Labait

The Labait tuff cone (04°34·028′S, 35° 25·876′E) is composed of olivine melilitite (Dawson *et al.*, 1997) that erupted in the Quaternary, based on an ~400 ka U–Pb age for metasomatic zircons within a Labait harzburgite xenolith (Rudnick *et al.*, 1999). The tuff contains abundant mantle and crustal xenoliths. Whereas the former have been investigated in several studies (Dawson *et al.*, 1997; Chesley *et al.*, 1999; Dawson, 1999; Lee & Rudnick, 1999; Rudnick *et al.*, 1999; Burton *et al.*, 2000; Vauchez *et al.*, 2005; Aulbach *et al.*, 2008, 2011; Koornneef *et al.*, 2009), this and associated studies (Bellucci *et al.*, 2011; Blondes *et al.*, in preparation) are the first investigation of the crustal xenoliths, which consist of granites, amphibolites and granulites; our collection focuses on the granulites. Of the 107 crustal xenoliths collected, 28 samples, representing the diversity observed within the granulite suite, were selected for thin sectioning and a further 13 of these were selected for geochemical analysis.

Downloaded from http://petrology.oxfordjournals.org/ at University of Dar es Salaam on March 8, 2016

Table 1: Sample classification, mineralogy and microstructure

Sample	Major phases	Accessory phases	Notes
Labait (4°34·028′S, 35°25·876′E)			
Two-pyroxene granulites			
LB04-04	pl–cpx–opx–ilm	ap, zrn	equigranular
LB04-09	pl–anti–opx–cpx–ilm	ap, qtz, rt	medium-grained pl and bimodal px, moderately altered along grain boundaries
LB04-12	pl–opx–cpx	bt, ilm	medium-grained pl and bimodal px, moderately altered along grain boundaries
LB04-16	anti–cpx–opx	ap, bt, ilm, zrn	medium-grained pl and bimodal px, moderately altered along grain boundaries
LB04-19	anti–opx–cpx–ilm	ap, mz, zrn	medium-grained pl and bimodal px, moderately altered along grain boundaries
LB04-34	anti–opx–cpx	ap, ilm, zrn	medium-grained pl and bimodal px, moderately altered along grain boundaries
LB04-36	pl–opx–cpx–qtz–ilm	ap, zrn	mottled medium-grained pl and bimodal px, moderately altered along grain boundaries
LB04-38	pl–opx–cpx	ap, ilm, mz, zrn	equigranular
LB04-41	anti–opx–cpx	ap, bt, ilm	medium-grained pl and bimodal px, moderately altered along grain boundaries
LB04-46	anti–ilm–opx–cpx	ap, zrn	mottled medium-grained pl and bimodal px, extensively altered along grain boundaries
LB04-50	anti–cpx–opx–ilm	ap	medium-grained pl and bimodal px, weakly foliated
LB04-52	anti–opx–cpx–ilm	ap, zrn	medium-grained pl and bimodal px, weakly foliated, little alteration
LB04-53	anti–opx–cpx–ilm	ap, zrn	medium-grained pl and bimodal px, weakly foliated
LB04-65	anti–cpx–opx–ilm	ap, zrn	compositionally banded polygonal aggregate with medium-grained pl, bimodal px, heavily altered along grain boundaries
LB04-93	anti–opx–cpx	ap, ilm	medium-grained pl and bimodal px, moderately foliated, little alteration
LB-48	anti–opx–cpx	ap, zrn	medium-grained pl and bimodal px
Hornblende-two-pyroxene granulites			
LB04-07	pl–hbl–cpx–opx–ilm	ap	equigranular, with millimeter-scale compositional bands defined by hbl
LB04-48	pl–opx–cpx–hbl	ap, bt, ilm, mz	equigranular, with millimeter-scale compositional bands defined by hbl
LB04-82	pl–cpx–opx–hbl–ilm	ap, bt, zrn	equigranular, with millimeter-scale compositional bands defined by hbl
Garnet–orthopyroxene granulites			
LB04-39	pl–gt–qtz–opx	ap, bt, rt, zrn	gt porphyroblasts in polygonal matrix of pl, opx and qtz, cpx is rare, extensively altered along grain boundaries
LB04-91	pl–gt–anti–qtz–opx	ap, rt, zrn	irregular, discontinuous bands of qtz and gt, qtz occurs only in bands
Anorthosite			
LB04-27	pl–gt–cpx	cor, mt, spl	polygonal plagioclase cut by veins of secondary mineralization replacing mafic phases
Lashaine (3°22·052′S, 36°25·457′E)			
Garnet–clinopyroxene granulites			
89-726	pl–cpx–gt	ap, cor, ky, rt, sc, sf, ttn	cpx atolls with gt coronae in plagioclase matrix
89-727	pl–cpx–gt	ap, ky	elongated cpx atolls with gt coronae in plagioclase matrix
89-729	pl–cpx–gt	rt, sc, ttn	mafic atolls and cpx megacrysts in pl-rich matrix
89-730	cpx–gt–pl–opx	ilm, rt	equigranular mosaic of pl, px and gt
89-731	pl–cpx–gt	rt, ttn	mafic atolls and cpx megacrysts in pl-rich matrix
89-732	pl–cpx–gt	ky, rt	cpx atolls with gt coronae in plagioclase matrix
89-734	cpx–gt–pl–opx	ap, rt	equigranular mosaic of pl, px and gt
89-735	pl–cpx–gt–ky		mafic atolls and cpx megacrysts in pl-rich matrix
89-739	pl–cpx–gt–opx	ky, rt	cpx atolls with gt coronae in plagioclase matrix
89-741	pl–cpx–gt–opx	ky	cpx atolls with gt coronae in plagioclase matrix
89-742	pl–cpx–gt–opx	ky, rt	cpx atolls with gt coronae in plagioclase matrix
89-744	pl–cpx–gt–opx	ap, rt	cpx atolls with gt coronae in plagioclase matrix
Biotite–garnet granulites			
89-733	pl–bt–cpx–opx–gt	ap, ilm, zrn	fine-grained, with a foliation defined by alignment of the biotite crystals
89-745	pl–bt–cpx–opx–gt	ilm, zrn	fine-grained, with radiating clusters of opaque biotite

(continued)

Downloaded from http://petrology.oxfordjournals.org/ at University of Dar es Salaam on March 8, 2016

Table 1: Continued

Sample	Major phases	Accessory phases	Notes
Naibor Soito (2°46·884′S, 36°0·831′E)			
Quartz-bearing granulites			
NS04-01	pl–qtz–anti–cpx–opx	ap, bt, gt, hbl, ilm, rt, zrn	irregular clusters of coarse qtz + pl + anti and embayed px in pl–qtz–opx groundmass, bt and rt associated with ilm
NS04-05	pl–cpx–qtz–opx	ap, bt, ilm, hbl, sf, zrn	banded, with irregular clusters of coarse qtz + pl and embayed px in pl + qtz–opx groundmass, bt associated with ilm, hbl rims px, late zeolite
NS04-13	(A) pl–qtz–opx–cpx–kf–gt (B) pl–opx–cpx–hbl–bt–gt	ap, ilm	foliated composite xenolith composed of felsic (A) and mafic (B) layer
NS04-53	qtz–pl–gt–kf–opx	ap, bt, ilm, zrn	granoblastic, with abundant felsic minerals
NS04-73	pl–cpx–opx–qtz–ilm	ap	slightly foliated, banded into mafic and felsic layers, with irregular clusters of qtz + pl and fine to coarse px in pl–qtz–px groundmass
NS04-83	pl–qtz–cpx–opx–ilm	ap, zrn	banded, equigranular, with scattered, embayed px
NS04-91	pl–cpx–opx–bt–qtz–gt	al, ap, ilm, hbl, zrn	irregular clusters of coarse qtz + pl and embayed px in pl–qtz–opx groundmass
NS04-93	pl–cpx–gt–hbl–opx	ap, ilm, zrn	compositionally banded into mafic- and felsic-rich layers, with irregular clusters of qtz + pl and fine to coarse px in pl–qtz–px groundmass
NS04-94	qtz–pl–cpx–opx	ap, ilm, sf, zrn	equigranular qtz and pl, dispersed band of px, sf-rich
NS04-96	pl–qtz–opx–cpx	ap, ilm	equigranular, with scattered, embayed px
NS04-98	pl–qtz–cpx–bt–opx	ap, ilm, zrn	equigranular, with scattered, embayed px
NS04-104	pl–qtz–opx–cpx	ap, ilm, zrn	equigranular, with scattered, embayed px
W3S-1	pl–qtz–gt–opx–cpx	ap, bt, rt, zrn	irregular clusters of coarse qtz + pl and fine, embayed px in pl–qtz–opx groundmass
W3S-2	pl–qtz–opx–cpx	ap, ilm, zrn	equigranular, with scattered, embayed px
Quartz-free granulites			
NS04-07	pl–cpx–opx–hbl–gt	ap, ilm	slightly foliated pyroxenes with interstitial pl, hbl rims px
NS04-16	pl–cpx–gt–hbl	ap, bt, ilm, sf, zrn	disaggregated cpx atolls with gt coronae in pl matrix, CO_2 fluid inclusions in cpx, hbl rims px, bt rims ilm, late zeolite and carbonate
NS04-27	pl–cpx–gt–hbl	ap, ilm, rt, sf, zrn	banded, equigranular, gts form elongate bands (former coronae?), hbl rims cpx and ilm
NS04-60	cpx–pl–gt–opx–hbl	ap, bt, ilm, rt, sf	slightly foliated px with interstitial pl, gt forms disrupted coronae, cpx vein, minor interstitial glass
NS04-61	pl–cpx–bt–opx–ilm–gt	ap, hbl	coarse pl and px, bt rims ilm and hbl rims cpx
NS04-80	pl–gt–cpx–hbl–opx–ilm	ap, rt	coarse, mosaic pl and px rimmed by gt coronae, hbl rims cpx
NS04-150	pl–hbl–cpx–opx–ilm	ap, bt, zrn	contains abundant hbl

Major phases listed in order of abundance. Accessory phases (defined as <1% by volume) listed alphabetically. Mineral abbreviations: anti, antiperthite; al, allanite; ap, apatite; bt, biotite; cor, corundum; cpx, clinopyroxene; ilm, ilmenite; gt, garnet; hbl, hornblende; kf, K-feldspar; ky, kyanite; mz, monazite; pl, plagioclase; opx, orthopyroxene; qtz, quartz; rt, rutile; sc, scapolite; sf, sulfide; ttn, titanite; zrn, zircon. Samples listed in bold font are those for which whole-rock compositions have been determined.

The majority of the Labait granulites are mafic, two-pyroxene granulites, many of which contain antiperthitic feldspars and a few of which contain hornblende (Table 1, Fig. 2). Two of the samples (LB04-39 and LB04-91) are garnet–orthopyroxene granulites and one sample, LB04-27, is a garnet-bearing anorthosite.

Two-pyroxene granulites

These consist of antiperthite (or plagioclase) + orthopyroxene + clinopyroxene + ilmenite ± biotite ± apatite ± zircon ± monazite. Anhedral feldspar (50–60%) and pyroxene (40–50%) together make up more than 90% of the modal mineralogy in these samples. Texturally, the two-pyroxene granulites are granoblastic (Fig. 2a and b), with alignment of pyroxene crystals defining a weak foliation in some samples (Fig. 2c and d). Most two-pyroxene granulites show alteration along grain boundaries and mottling of feldspar. The hornblende-bearing two-pyroxene granulites (LB04-07, LB04-48 and LB04-82) have major phase proportions similar to the two-pyroxene granulites, except for the presence of hornblende in ~1 mm thick bands. Hornblende is in textural equilibrium with the other major phases (Fig. 2g and h) and makes up ~10–25% of the rock (Table 2).

Garnet–orthopyroxene granulites

LB04-39 and LB04-91 consist of plagioclase, garnet, quartz and orthopyroxene (Fig. 2e–f). In LB04-39, garnet

Downloaded from http://petrology.oxfordjournals.org/ at University of Dar es Salaam on March 8, 2016

Table 2: Modal mineralogy (vol. %) for selected Tanzanian granulite xenoliths*

	Labait										
	Two-pyroxene granulites								2px–hbl gran.		Anor.
	LB04-09	LB04-19	LB04-36	LB04-46	LB04-52	LB04-53	LB04-65	LB04-93	LB04-07	LB04-82	LB04-27
feld	57	56	42	53	67	59	60	67	39	42	68
cpx	4	11	4	2	18	14	15	15	11	11	6
opx	6	18	6	8	4	15	10	9	10	8	–
gt	–	–	–	–	–	–	–	–	–	–	13
hbl	–	–	–	–	–	–	–	–	24	7	–
bt	–	–	–	–	–	–	–	–	–	tr	–
op	4	3	3	19	3	2	2	1	2	5	tr
qtz	1	–	7	–	–	–	–	–	–	–	–
ky	–	–	–	–	–	–	–	–	–	–	–
alt	28	13	39	19	8	10	13	7	13	28	13

	Labait		Lashaine									
	Gt–opx gran.		Garnet–clinopyroxene granulites								Bt gran.	
	LB04-39	LB04-91	89-726	89-727	89-729	89-730	89-731	89-732	89-734	89-735	89-733	89-745
feld	30	33	47	58	62	40	63	50	31	64	54	45
cpx	–	–	35	19	6	16	1	24	12	16	18	16
opx	3	2	–	–	–	8	–	–	15	–	8	2
gt	20	7	16	19	14	23	16	17	39	16	14	16
hbl	–	–	–	–	–	–	–	–	–	–	–	–
bt	tr	–	–	–	–	–	–	–	–	–	13	20
op	1	1	tr	tr	–	–	–	–	–	–	tr	2
qtz	8	3	–	–	–	–	–	–	–	–	–	–
ky	–	–	tr	tr	–	–	–	tr	–	3	–	–
alt	39	36	2	5	18	14	20	9	3	4	4	–

	Naibor Soito									
	Quartz granulites							Quartz-free granulites		
	NS04-01	NS04-05	NS04-13†	NS04-73	NS04-83	NS04-91	NS04-98	NS04-150	NS04-61	NS04-80
feld	63	66	60	57	71	67	62	53	41	35
cpx	9	12	4	16	5	19	6	9	35	9
opx	4	4	1	6	2	17	2	1	6	1
gt	1	–	3	–	–	3	–	–	1	17
hbl	tr	1	–	–	–	tr	–	34	tr	5
bt	tr	1	tr	–	–	6	3	tr	13	–
op	tr	1	–	4	1	tr	tr	1	3	1
qtz	12	7	26	4	15	3	21	–	–	–
ky	–	–	–	–	–	–	–	–	–	–
alt	10	10	4	13	6	1	9	2	4	2

*Modal mineralogy by volume for samples for which geochemical data were obtained. Modes are based on point counting between 600 and 800 points per thin section on a petrographic microscope. Mineral abbreviations as in Table 1; 'alt' represents amorphous material that is generally concentrated along grain boundaries, 'op' represents opaque minerals. Plagioclase and alkali feldspar modes are combined, owing to difficulty in distinguishing between them.
†Modes for this sample represent both bands that are present in the thin section.
—, mineral was not observed; tr, trace amounts (<1%) of the mineral are present.

Downloaded from http://petrology.oxfordjournals.org/ at University of Dar es Salaam on March 8, 2016

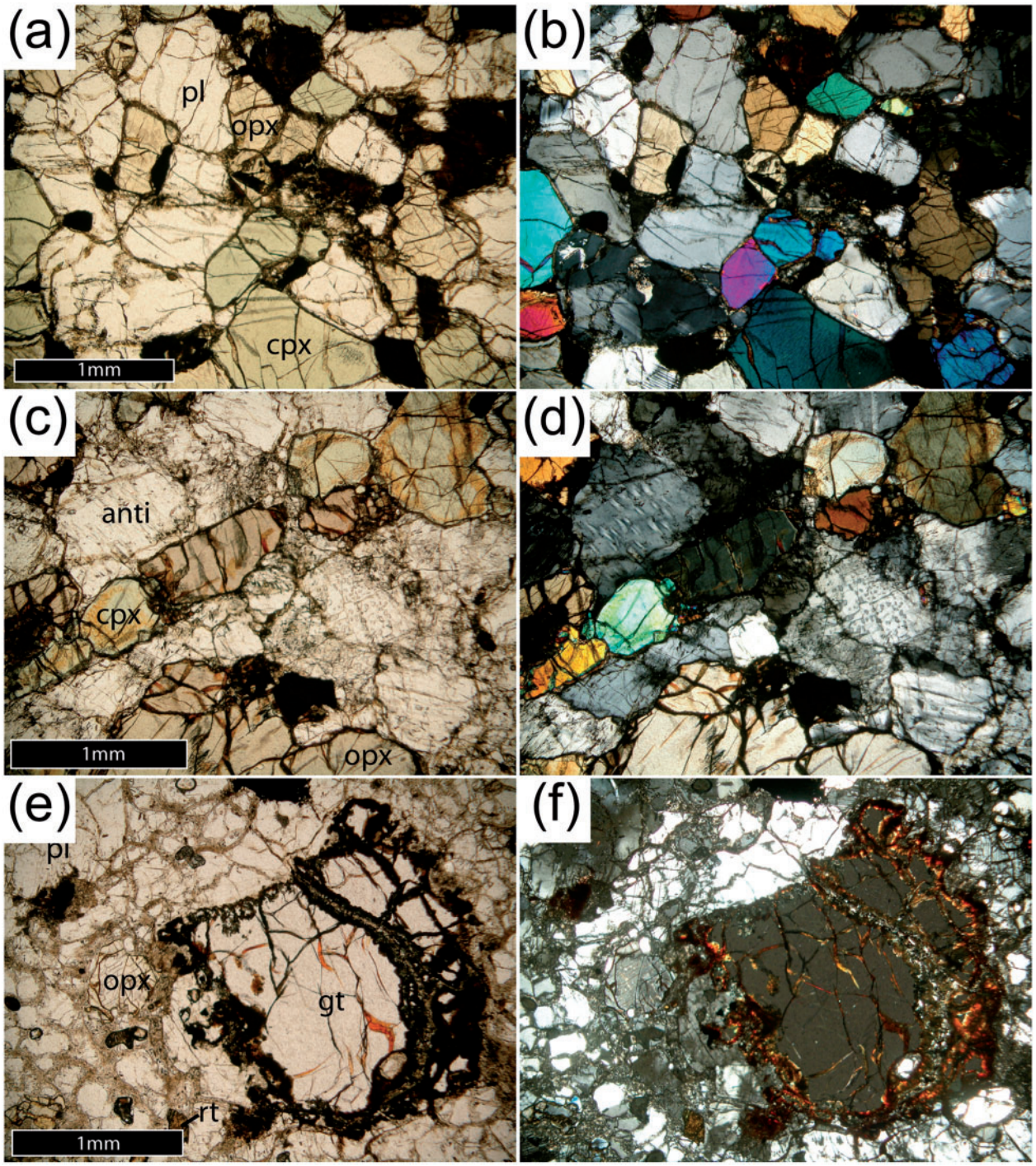


Fig. 2. Representative textures in granulite-facies xenoliths from Labait. All left-hand panels are in plane-polarized light; the right-hand panels are in crossed polars. Mineral abbreviations as in Table 1. (a, b) Two-pyroxene granulite LB04-52. Opaque phase is ilmenite. (c, d) Two-pyroxene granulite LB04-19 showing preferred orientation of pyroxenes. (e, f) Garnet–orthopyroxene granulite LB04-39. Garnet rims are kelyphite. (g, h) Hornblende two-pyroxene granulite LB04-82. Hornblende (brown in plane-polarized light) has a similar color to grain boundary alteration. The hornblende appears to be in textural equilibrium with the other phases in the rock. (i, j) Anorthosite LB04-27.

(continued)

Downloaded from http://petrology.oxfordjournals.org/ at University of Dar es Salaam on March 8, 2016

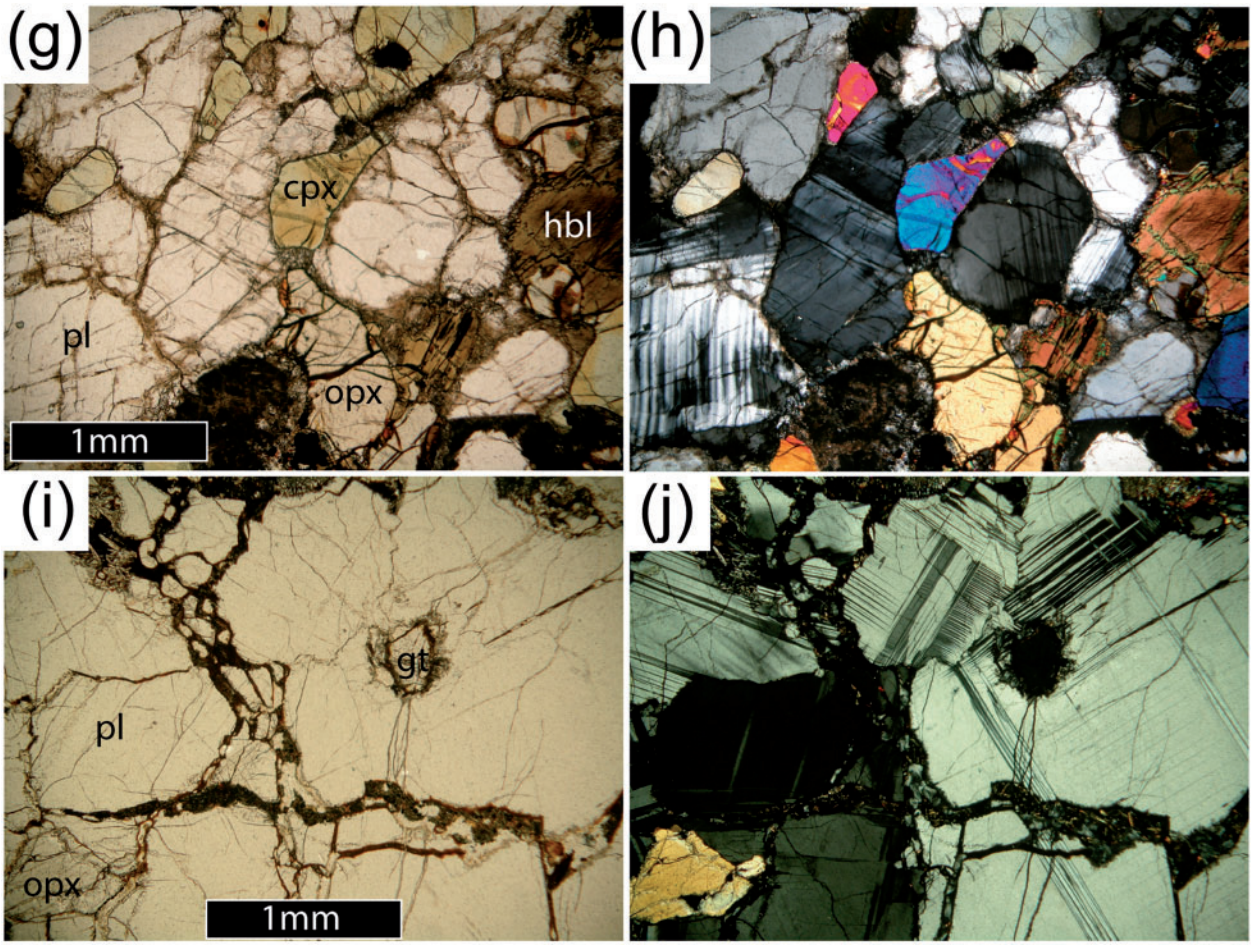


Fig. 2. Continued.

(40%) occurs as porphyroblasts (up to 5 mm in diameter) in a heterogeneous matrix of plagioclase (50%), orthopyroxene (10%) and minor quartz. Clinopyroxene is rare. LB04-91 consists of alternating millimeter-scale bands of garnet and plagioclase + quartz + orthopyroxene with minor antiperthite.

Anorthosite

LB04-27 consists of coarse, anhedral crystals of calcic plagioclase that form ~70% of the mode (Fig. 2i and j). The remainder consists of fine-grained alteration along grain boundaries and rare crystals of garnet, spinel and corundum.

Lashaine

The Lashaine tuff cone (3°22·052′S, 36°25·457E) consists of an early phase of ankaramitic scoria, which was followed by carbonatitic tuff (Cohen *et al.*, 1984). Mantle and crustal xenoliths from Lashaine have formed the basis of a number of previous investigations (Dawson *et al.*, 1970; Reid & Dawson, 1972; Dawson & Smith, 1973; Reid *et al.*, 1975; Rhodes & Dawson, 1975; Ridley & Dawson, 1975; Pike *et al.*, 1980; Jones *et al.*, 1983*b*; Cohen *et al.*, 1984; Rudnick *et al.*, 1994; Burton *et al.*, 2000; Dawson, 2002; Gibson *et al.*, 2013). Fourteen crustal xenoliths from Lashaine were examined in thin section (Table 1), eight of which were analyzed for their whole-rock compositions.

Garnet–clinopyroxene granulites

Twelve of the granulites consist of plagioclase + clinopyroxene + garnet ± orthopyroxene ± scapolite ± rutile ± kyanite ± apatite (Fig. 3a–h), which we refer to as the garnet–clinopyroxene granulites. These are similar to the Lashaine xenoliths described by Dawson (1977) and Jones *et al.* (1983*b*) and include the samples investigated by Moecher & Essene (1991). Plagioclase occurs as coarse (0·5–1 mm) polygonal crystals and makes up 30–65% of the mode; only three samples (89-726, 89-730 and 89-734) contain <50% plagioclase. Kyanite [identified by X-ray diffraction by Jones *et al.* (1983*b*)] is common as euhedral to rounded inclusions within plagioclase (Fig. 3k and l), and scapolite occurs at some plagioclase triple junctions.

Downloaded from http://petrology.oxfordjournals.org/ at University of Dar es Salaam on March 8, 2016

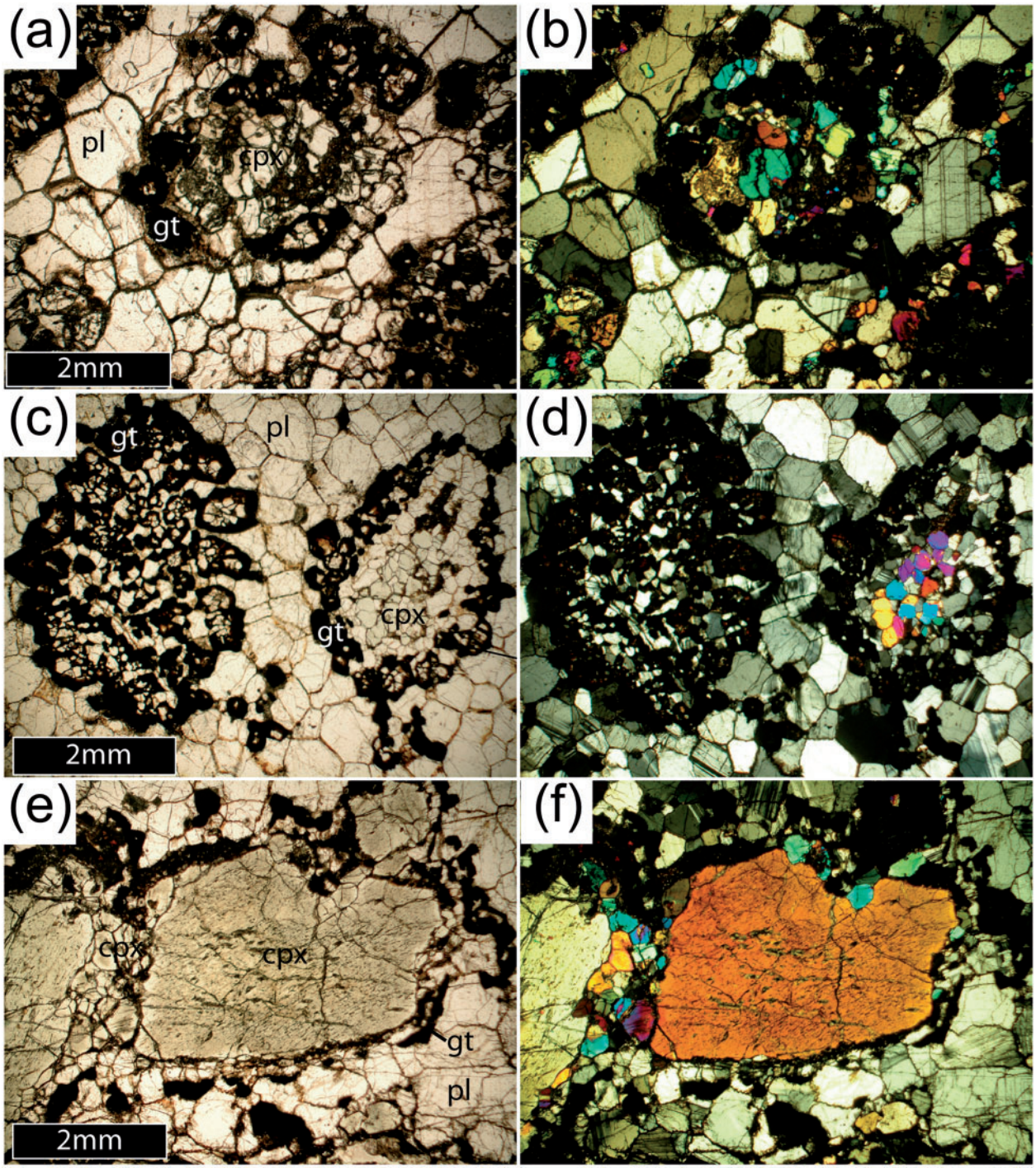


Fig. 3. Representative textures in granulite-facies xenoliths from Lashaine. All left-hand panels are in plane polarized light; right-hand panels are in crossed polars. Mineral abbreviations as in Table 1. Garnet in all images is partially to fully replaced by dark kelyphite. (a, b) Garnet–clinopyroxene granulite 89-727 showing atoll texture of garnet rimming clinopyroxene cluster. (c, d) Garnet–clinopyroxene granulite 89-729 showing atoll texture of garnet rimming plagioclase, rimming clinopyroxene cluster set in a mosaic plagioclase matrix. (e, f) Garnet–clinopyroxene granulite 89-729 showing atoll texture of garnet rimming large clinopyroxene crystal. (g, h) Garnet–clinopyroxene granulite 89-730 showing mosaic texture. (i, j) Biotite–garnet granulite 89-733. Biotites are completely altered to fine-grained opaque material. Equant opaque phase is ilmenite. (k) Euhedral kyanite inclusions within plagioclase in garnet clinopyroxene granulite 89-727. (l) Rounded kyanite inclusions within plagioclase and clinopyroxene in garnet clinopyroxene granulite 89-726.

(continued)

Downloaded from http://petrology.oxfordjournals.org/ at University of Dar es Salaam on March 8, 2016

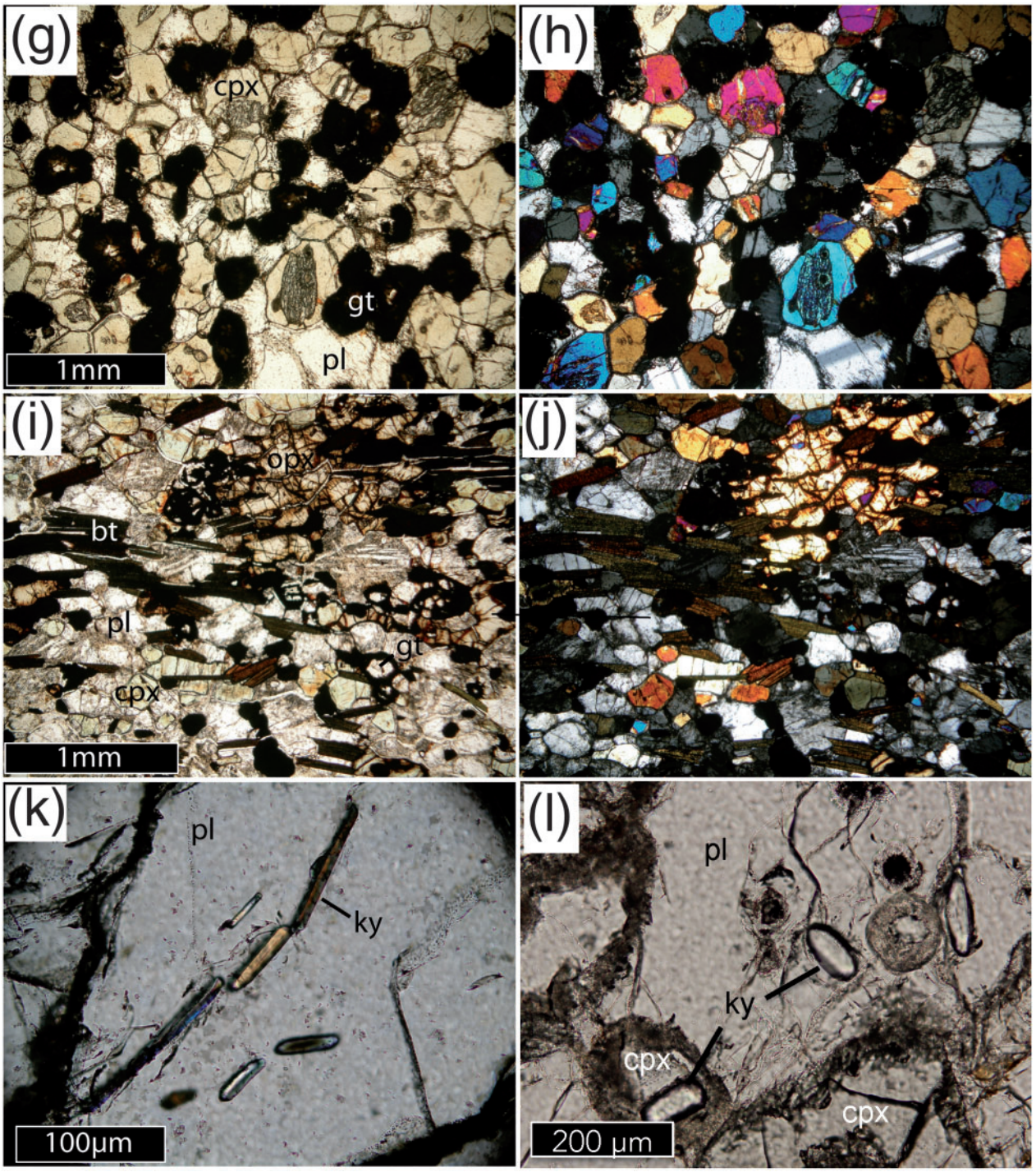


Fig. 3. Continued.

In samples with 50–65% modal plagioclase, garnet-ringed clinopyroxene aggregates form clusters within a polygonal matrix of plagioclase (Fig. 3a–d). In plagioclase-rich samples (>60% modal plagioclase, including 89-729, 89-731 and 89-735), clusters are small, isolated, and take one of three forms: (1) 2–5 mm aggregates of pale green, anhedral clinopyroxene crystals ringed by coronae of garnet ± plagioclase (Fig. 3c and d, right side); (2) 5–10 mm tabular clinopyroxene megacrysts ringed by discontinuous chains of garnet (Fig. 3e and f); (3) rare, 5 mm aggregates

Downloaded from http://petrology.oxfordjournals.org/ at University of Dar es Salaam on March 8, 2016

of garnet and plagioclase, which may represent edges of garnet–plagioclase coronae whose centers lie out of the plane of the thin section (Fig. 3c and d, left side of image). Jones *et al.* (1983*b*) noted that the pyroxene megacrysts are similar in size to the pyroxene aggregates and suggested that the mafic clusters originated via recrystallization of these megacrysts. As the volume occupied by mafic phases increases to 60–70%, clusters become larger and more interconnected, in some samples defining planes of foliation. In samples with only ~30–40% modal plagioclase (89-730 and 89-734), mafic atolls are absent, and the plagioclase, pyroxene and garnet occur in subequal proportions in a mosaic of ~0·2 mm crystals (Fig. 3g and h). Clinopyroxenes within the mafic clusters are commonly heavily altered and riddled with CO_2-rich fluid inclusions, giving the interior of the clusters a dark appearance (Fig. 3a).

Biotite–garnet granulites

Samples 89-733 and 89-745 contain biotite as a major phase and are distinct from xenoliths that have been described previously from Lashaine. The biotite–garnet granulites consist of plagioclase, biotite, clinopyroxene, orthopyroxene, garnet and ilmenite (Fig. 3i and j), with accessory apatite and zircon. Biotite forms red–brown to semi-opaque crystals up to 1 mm in length and occurs in textural equilibrium with other phases. In 89-733, platy mica crystals define a plane of foliation, whereas in 89-745, biotite forms radiating clusters and no foliation is present. Other phases are small (typically ~0·1 mm) and anhedral, their size limited by the biotite crystals. Orthopyroxene occurs as somewhat larger, embayed and commonly discolored crystals.

Naibor Soito

Naibor Soito (2°46·884′S, 36°0·831′E) (the name is based on information from local Maasai) is the westernmost member of an approximate east–west line of three small tuff cones that occur directly south of the mantle-xenolith localities of Pello Hill and Eledoi [described by Dawson & Smith (1988)]. The composition of the tuff has yet to be investigated, but nearby tuff cones erupted ankaramitic tuff (Cohen *et al.*, 1984). No mantle xenoliths have been observed at Naibor Soito, but crustal xenoliths are abundant; over 150 crustal xenoliths were collected from this locality. Of these, thin sections were made of 21 samples and 10 of these were analyzed for whole-rock chemistry.

Quartz-bearing xenoliths

Xenoliths from Naibor Soito differ from those from elsewhere in Tanzania in that they span a wider compositional range and can include quartz as a major phase. Quartz-bearing granulite-facies xenoliths are dominated by anhydrous, felsic domains, but also contain bands rich in both hydrous and anhydrous mafic phases. Felsic domains consist of coarse, anhedral crystals of plagioclase (60–70%), quartz (25–35%), orthopyroxene (5–10%), clinopyroxene (0–2%) and rare garnet (Fig. 4a–d). Alkali feldspar is present in samples with an intermediate whole-rock chemistry ($SiO_2 > 56$ wt %). Pyroxene forms chains of elongated, irregular crystals along boundaries between felsic phases (Fig. 4c and d). Clinopyroxene has a distinctly green color in plane-polarized light (Fig. 4c, g and i).

Mafic domains in the quartz-bearing xenoliths consist of plagioclase, pyroxene, hornblende, biotite, garnet and rare quartz. Hydrous phases are an important component of these mafic domains, in contrast to the felsic domains where they are rare or absent. In some samples, there is a tendency for biotite to rim ilmenite and hornblende to rim pyroxenes. Megacrysts of orthopyroxene (~1 mm) make up ~50% of the mafic domains and are commonly recrystallized to finer-grained orthopyroxene along their margins (Fig. 4e–h). With the exception of the pyroxene megacrysts, crystals are small (<0·1 mm), and the transition from felsic- to mafic-rich bands is generally marked by a pronounced fining of crystal sizes.

Quartz-free xenoliths

The quartz-free Naibor Soito xenoliths are massive and contain abundant pyroxene (both clinopyroxene and orthopyroxene), as well as plagiocase, garnet and ilmenite. In some quartz-free xenoliths corona textures similar to those observed in the Lashaine xenoliths are present; in these, medium-grained pyroxene aggregates are surrounded by rings of metamorphic garnet in a plagioclase matrix (Fig. 4i and j). In other samples the garnets form discontinuous trails that may represent disrupted coronae. Pyroxene is commonly recrystallized into fine crystals similar to those seen in the mafic bands of the quartz-bearing granulites, but larger, embayed pyroxene relicts also remain (Fig. 4i and j). One quartz-free xenolith (NS04-150) lacks coronae and is hornblende-rich. In other mafic samples hornblende is found rimming pyroxenes and biotite is found surrounding ilmenite. Common accessory phases include apatite, sulfide and zircon.

ANALYTICAL METHODS

Electron microprobe

Major element compositions of major phases, including plagioclase, alkali feldspar, clinopyroxene, orthopyroxene, garnet, biotite and hornblende, were determined using the JXA-8900 SuperProbe with WD/ED Combined Electron Probe Microanalyzer (EPMA) at the University of Maryland, College Park (UMCP). Operating conditions included a 15 keV accelerating voltage and a 10 nA cup current for feldspars and a 20 nA cup current for all other phases. Calibrations were achieved using natural mineral reference materials, with raw intensities corrected using the CIT-ZAF algorithm. Two-sigma relative standard

Downloaded from http://petrology.oxfordjournals.org/ at University of Dar es Salaam on March 8, 2016

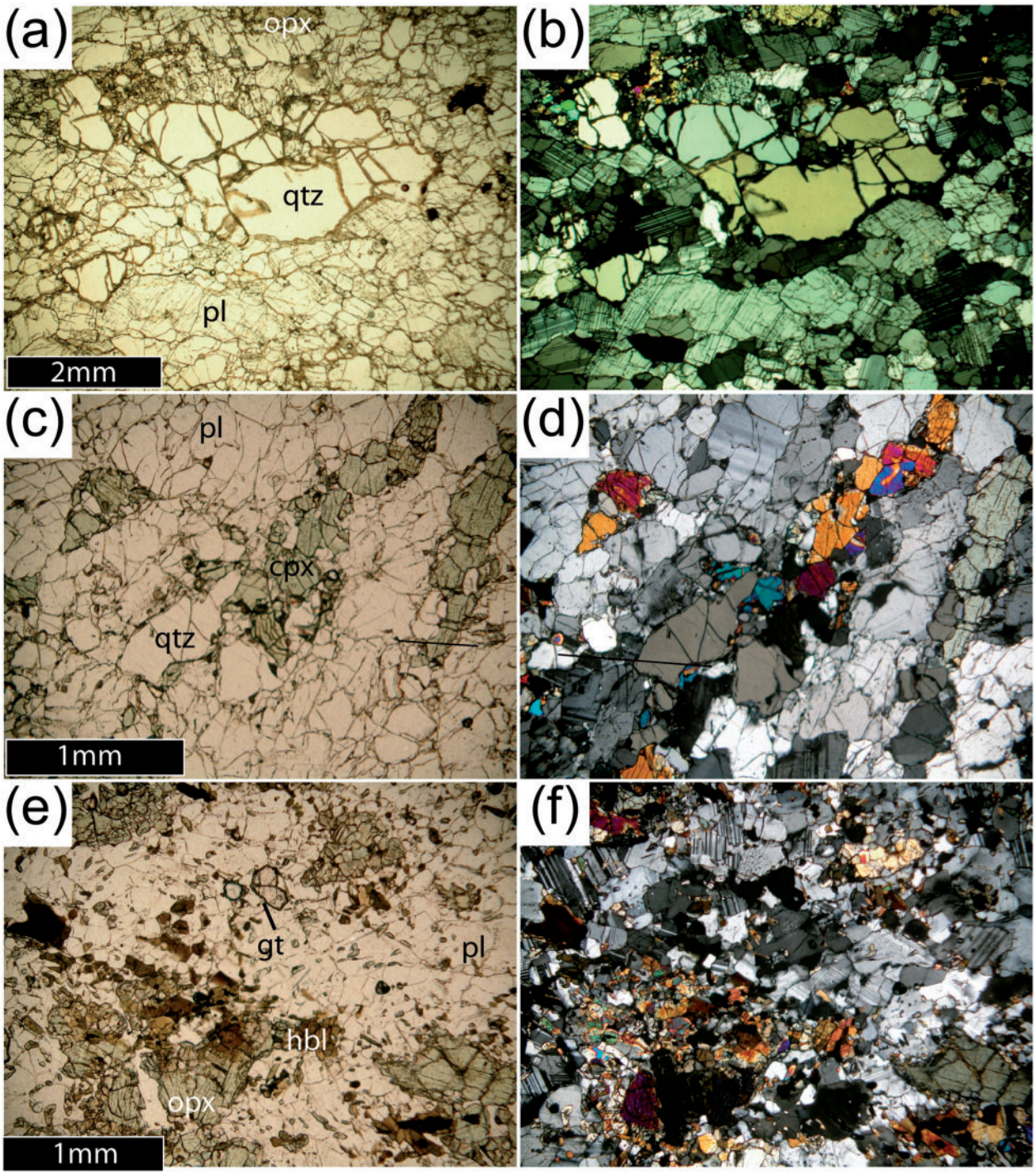


Fig. 4. Representative textures in granulite-facies xenoliths from Naibor Soito. All left-hand panels are in plane-polarized light; right-hand panels are in crossed polars. Mineral abbreviations as in Table 1. Garnet, where present, has thin rims of kelyphite. (a, b) Quartz-bearing granulite NS04-05; (c, d) quartz-bearing granulite NS04-13 showing alignment of clinopyroxene grains; (e, f) quartz-bearing granulite NS04-13; (g, h) quartz-bearing granulite NS04-91 showing orthopyroxene megacryst and bimodal grain size; (i, j) quartz-free granulite NS04-80 showing disrupted atoll texture.

(continued)

Downloaded from http://petrology.oxfordjournals.org/ at University of Dar es Salaam on March 8, 2016

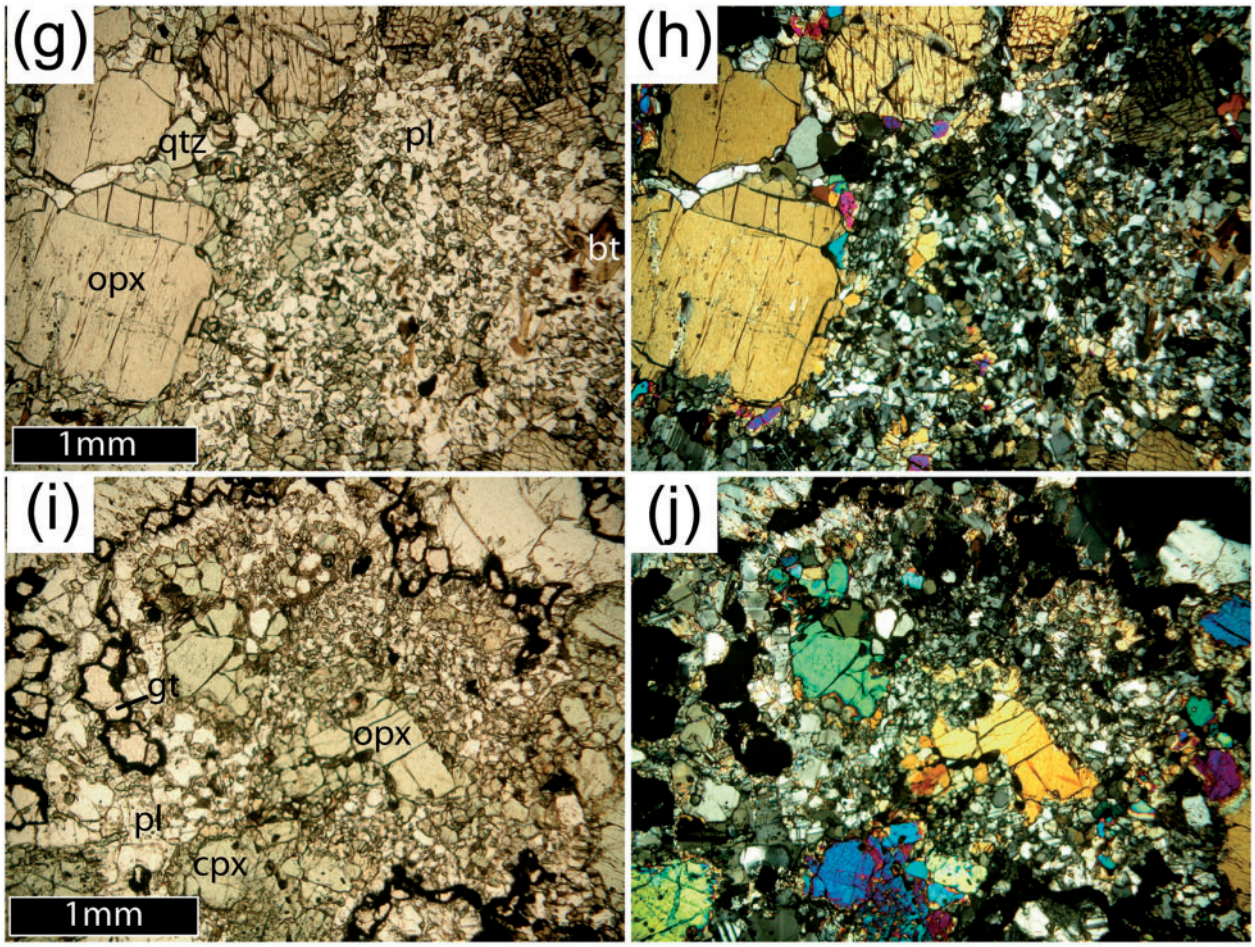


Fig. 4. Continued.

deviations for each phase are reported in the footnotes of the data tables (Tables A–F in the Supplementary Data Electronic Appendix; supplementary data are available for downloading at http://www.petrology.oxfordjournals.org) and are based on replicate analyses of the reference minerals. Reported compositions are averaged from 3–5 separate analyses from the same crystal domain. Phase chemistries for seven Lashaine xenoliths (89-726, 89-729, 89-730, 89-731, 89-733, 89-741, 89-744) are from unpublished energy-dispersive spectrometry (EDS) analyses performed by R. A. Sproule at the Australian National University as part of her vacation scholar project in 1991 [a description of the EDS method has been provided by Rudnick & Taylor (1991)]. Minerals from samples 89-727, 89-734, 89-739 and 89-742 were analyzed using both techniques and give comparable results. The newer data are reported.

Whole-rock chemical and isotope analyses

For the Labait and Naibor Soito xenoliths, samples were sawn in half and a thin-section billet was cut from a representative portion of the sample. Half of the sample was pulverized for geochemical analysis and the other half was preserved for future investigations. Banded samples (e.g. some Naibor Soito samples, Supplementary Data Fig. K) were cut perpendicular to the layers and all layers were incorporated into the sample that was pulverized. Samples were fragmented using a rock hammer, further reduced via a ceramic jaw crusher and unaltered chips were powdered in an agate ring mill. Powders were sent to Washington State University, Pullman (WSU) or Franklin and Marshall College (FMC) for major and trace element analysis by X-ray fluorescence (XRF). Total iron content from both laboratories is reported as Fe_2O_3. Long-term, 2σ precision at the WSU laboratory is better than 2% for most major elements and better than 20% for most trace elements at $\geq$20 ppm concentrations (see http://www.sees.wsu.edu/Geolab/note/xrf.html). Long-term, 2σ precision at the FMC laboratory is better than 1% for major elements and better than 10% for trace elements excepting Cr (25%), La and Pb (15%),

Downloaded from http://petrology.oxfordjournals.org/ at University of Dar es Salaam on March 8, 2016

and Th (70%, 2σ precision). Accuracy, based on analyses of BHVO-1 and QLO-1, is within 5% of nominal values for major elements and within 10% for trace elements at concentrations ≥10 ppm (see http://www.fandm.edu/x7992).

Trace element compositions for some samples were also analyzed by inductively coupled plasma mass spectrometry (ICP-MS) using a ThermoFinnigan Element 2 at the University of Maryland. Between 20 and 40 mg of sample powder were dissolved in distilled $HF–HNO_3$ in steel-jacketed Parr bombs at >160°C. Dissolved material was dried and treated with distilled HNO_3 and HCl until optically clear. Solutions were diluted 100–1000 times and spiked with In prior to analysis. Concentrations were determined using a standard-bracketing method, with BHVO-1 used as the primary standard. Precision (2σ) and accuracy on replicate analyses of AGV-1 and GSP-1 are better than 20% for most elements (Table G in Electronic Appendix).

A subset of the xenoliths was analyzed to determine their Sr–Nd isotopic compositions. Solutions were prepared as above, except most samples were spiked with solutions enriched in ^{84}Sr (80·6% in spike), ^{150}Nd (97·6%) and ^{149}Sm (97·7%) prior to dissolution. Rough cuts of each element were separated using cation-exchange columns and purified using element-specific resins.

Sr cuts were evaporated with TaO onto Re filaments and measured on the VG Sector 54 TIMS system at Maryland. $^{87}Sr/^{86}Sr$ were normalized to $^{86}Sr/^{88}Sr = 0·1194$. SRM987 yielded a mean value of $0·710243 \pm 28$ (2σ, $n = 18$) over all analytical sessions.

Sm and Nd were analyzed using the Nu Plasma multi-collector (MC)-ICP-MS system at Maryland. $^{143}Nd/^{144}Nd$ ratios were normalized to a $^{146}Nd/^{144}Nd = 0·7219$ and standardized to the value of the AMES-Nd standard measured during each analytical session. AMES yielded a mean value of $0·512194 \pm 52$ (2σ, $n = 94$) over all analytical sessions.

U–Pb zircon dating by laser ablation (LA)-ICP-MS

U–Pb ages for zircons from six samples were obtained using a New Wave 213 μm Nd:YAG laser coupled to an Element 2 ICP-MS system at UMCP. Zircons were separated using conventional magnetic and heavy liquid techniques, then mounted, polished and imaged using cathodoluminescence (CL) to reveal internal zoning (see Supplementary Data Fig. J for CL images). U–Pb ratios and ages were calculated using the standard-bracketing procedure of Chang *et al.* (2006), which uses a slope-intercept method to correct time-integrated fractionation of U–Pb ratios and external standardization to correct instrumental mass bias. Harvard zircon 91500 (*c.* 1060 Ma, Wiedenbeck *et al.*, 1995) was employed as the external standard and was measured twice for every block of five samples. A typical analysis used a beam with a 45% energy flux at 10 Hz to produce a spot 40 μm in diameter. Eight masses were monitored: 202, 204, 206, 207, 208, 232, 235 and 238. Background counts on ^{206}Pb, ^{207}Pb and ^{208}Pb were <30 c.p.s. Counts on ^{204}Pb were generally <50 c.p.s., and no common Pb correction was applied. Single analyses were inspected to ensure data quality, and secondary zircon standards were measured during each session (Supplementary Data Table H in Electronic Appendix). MCC12S-15E, a zircon separate from the *c.* 1780 Ma Mullen Creek Mafic Complex (Premo & Loucks, 2000), yielded an average $^{207}Pb/^{206}Pb$ age of 1779 ± 19 Ma (2σ, $n = 8$). Temora 1 (416·8 ± 0·2 Ma, Black *et al.*, 2003) yielded an average $^{206}Pb/^{238}U$ age of 414 ± 31 Ma (2σ, $n = 34$).

RESULTS

Mineral chemistry

Feldspar

Plagioclase is present in all samples as either a major phase or as domains in antiperthite. Plagioclase has compositions of $An_{32–52}Ab_{47–64}Or_{0–6}$ at Labait (excluding the anorthosite, which contains anorthite of $An_{89}Ab_{11}$), $An_{25–48}Ab_{50–68}Or_{2–11}$ at Naibor Soito, and $An_{22–45}Ab_{58–76}Or_{2–5}$ at Lashaine (Supplementary Data Electronic Appendix Table A). On average, plagioclase compositions are dominated by sodic feldspar. Whereas plagioclase crystals in the Labait granulites do not show resolvable core-to-rim zoning in major elements, plagioclase grains in both the Lashaine and Naibor Soito samples are zoned to higher An contents on the rims. In the coronal granulites from these localities there is no apparent difference between crystals inside and outside coronae. Plagioclase compositions at Naibor Soito and Lashaine reflect whole-rock chemistry. In the Naibor Soito suite, the orthoclase component is generally high relative to plagioclase in the other suites and increases as whole-rock chemistry becomes more felsic. In the Lashaine suite, the anorthite component generally increases from the pyroxene-rich ($An_{22–26}$) to the plagioclase-rich xenoliths (An_{40}). Only the Labait anorthosite xenolith LB04-27 contains anorthite-rich plagioclase ($An_{87–89}Ab_{11–12}$), a composition similar to plagioclase from Archean anorthosite complexes (Ashwal, 1993).

Alkali feldspar occurs as exsolution lamellae in antiperthite in xenoliths from Labait ($An_{1–3}Ab_{7–23}Or_{73–91}$) and as crystals in intermediate xenoliths from Naibor Soito ($An_6Ab_{31–34}Or_{60–64}$). BaO contents in alkali feldspar are high (up to 1·7 wt % at Labait, and 1·3 wt % at Naibor Soito) (see Supplementary Data Electronic Appendix Table B).

Pyroxene

Pyroxene compositions are summarized in Supplementary Data Tables C and D in the Electronic Appendix.

Downloaded from http://petrology.oxfordjournals.org/ at University of Dar es Salaam on March 8, 2016

Pyroxenes are classified using the Ca–Fe–Mg system described by Morimoto *et al.* (1988). Clinopyroxenes in the Labait granulites are diopside or Mg-rich augite ($En_{36–40}Fs_{4–18}Wo_{46–55}$), with a low jadeite component (<1 mol %) and show core-to-rim chemical zoning corresponding to discoloration of clinopyroxene rims. Two zoning patterns are observed: (1) in the two-pyroxene granulites and garnet–orthopyroxene granulite, rimward zoning to lower FeO and TiO_2 and higher CaO; (2) in the hornblende-bearing two-pyroxene granulites, rimward zoning to higher Al_2O_3 and lower CaO. By contrast, clinopyroxenes from the Naibor Soito and Lashaine suites are homogeneous. In the Naibor Soito xenoliths, clinopyroxenes are iron-rich augite ($En_{34–40}Fs_{14–23}Wo_{43–47}$), with a low jadeite component (<1 mol %). In the Lashaine xenoliths, pyroxene composition varies with rock type: crystals in garnet–clinopyroxene granulites are relatively iron-poor diopside ($En_{40–44}Fs_{7–11}Wo_{47–53}$) with a high jadeite component (up to 16 mol %), whereas clinopyroxene in the biotite–garnet granulite is relatively iron-rich, jadeite-poor and resembles the augites from Naibor Soito.

Orthopyroxene is present in most Labait and Naibor Soito xenoliths, but is mostly absent from the Lashaine samples. Orthopyroxenes from Labait ($En_{52–66}Fs_{34–46}Wo_{0–4}$) and Naibor Soito ($En_{46–61}Fs_{37–54}Wo_{1–3}$) are hypersthene, with orthopyroxenes in the intermediate Naibor Soito samples ranging to more iron-rich compositions (see Supplementary Data Electronic Appendix Table D). Orthopyroxenes in the Labait two-pyroxene granulites have lower Ca contents at their rims. Rare orthopyroxenes in the Lashaine xenoliths span a wide range of compositions that correlate with rock type; orthopyroxenes in the biotite–garnet granulites are more iron-rich than those in the garnet–clinopyroxene granulites and resemble those from Naibor Soito.

Garnet

Garnet, which is unzoned, occurs in most samples from Naibor Soito and Lashaine, but only rarely within the Labait suite. Garnet compositions tend to reflect the whole-rock chemistry. Garnet in the anorthosite LB04-27 is grossular-rich ($Pyr_{51}Alm_{29}Grs_{20}$) relative to that in garnet–orthopyroxene granulite LB04-39 ($Pyr_{49}Alm_{39}Grs_{12}$); garnet compositions in the Naibor Soito xenoliths are almandine-rich ($Pyr_{25–34}Alm_{50–65}Grs_{15–19}$) (see Supplementary Data Electronic Appendix Table E). Likewise, garnets in the Lashaine garnet–clinopyroxene granulites are grossular-rich ($Pyr_{30–48}Alm_{29–55}Grs_{13–26}$), but those from biotite–garnet granulite 89-733 are the most almandine-rich garnets in all of the samples ($Pyr_{11}Alm_{70}Grs_{19}$).

Hydrous phases

Hornblende and biotite are common as minor phases and rare as major phases in the Tanzanian xenoliths. Concentrations of TiO_2 and F in biotite from Labait and Lashaine are typically high (2·1–5·6 wt % and 0·5–1·7 wt %, respectively; see Supplementary Data Electronic Appendix Table F), consistent with the partitioning of these elements into hydrous minerals previously observed in granulite-facies rocks (Gilbert *et al.*, 1982; Guidotti, 1984). The biotite composition in one of the Lashaine biotite–garnet granulites, 89-733, is titanium- and iron-rich and resembles some of the biotites seen in the Naibor Soito granulites. Fluorine contents in biotite and hornblende in the Naibor Soito xenoliths are relatively low (0·2–0·4 wt %), which may suggest their formation during retrograde metamorphism, consistent with textural evidence for their secondary origin.

Conditions of metamorphism

Metamorphic equilibration conditions experienced by the samples were evaluated using equilibrium assemblage diagrams (i.e. pseudosections) as well as cation-exchange thermobarometers. The former are useful for evaluating peak metamorphic conditions and, possibly, the P–T paths (in the cases where reactions are indicated from petrography), whereas the latter may be useful for discerning final equilibration temperatures, particularly using mineral rim compositions.

Equilibrium assemblage diagrams were calculated using the Theriak/Domino software (de Capitani & Petrakakis, 2010), using the Holland & Powell (1998) thermodynamic database (dataset tcds55, updated in November 2003) and the default solution models found in the Theriak/Domino software. Bulk-rock compositions determined by XRF and converted from oxides to moles were used for these calculations. Equilibration temperatures were estimated using the Brey & Köhler (1990) two-pyroxene thermometer (T_{BKN}) and the Krogh-Ravna (2000) garnet–clinopyroxene thermometer (T_{KR}). Nominal uncertainties are at least ± 50°C (2σ). Temperatures were calculated using an assumed pressure of 1 GPa. Equilibration pressures were estimated using the Al-in-opx barometer (P_{BKN}) calibrated by Brey & Köhler (1990). This calculation is sensitive to the contribution of Fe^{3+}, which was calculated here using the charge balance method described by Droop (1987). Nominal errors on this calculation are ±0·6 GPa (2σ) (Brey & Köhler, 1990).

Labait

Equilibrium assemblage diagrams are not particularly illuminating when it comes to the Labait two-pyroxene granulites, as the phase assemblage of orthopyroxene–clinopyroxene–feldspar persists over a wide region of P–T space for all observed bulk compositions, generally at temperatures above 750°C and at pressures below 1·0–1·25 GPa. However, the presence of antiperthitic feldspars in a number of samples, presumably exsolved from original ternary feldspars (Table 1, Fig. 2), indicates very high equilibration temperatures of >1000°C

Downloaded from http://petrology.oxfordjournals.org/ at University of Dar es Salaam on March 8, 2016

(e.g. Green & Usdansky, 1986; Fuhrman & Lindsley, 1988; Stipska & Powell, 2005), possibly relict from their igneous parentage. Compositional zoning in the pyroxenes also indicates significant cooling. Cores preserve relatively high temperatures (550–800°C), whereas rims indicate equilibration at 480–670°C (Table 3). By contrast, compositional zoning in two of the three hornblende-bearing two-pyroxene granulites indicates heating of the samples, with cores preserving temperatures of 650–700°C and rims recording temperatures of 780–850°C (Table 3).

The phase assemblages in the garnet–orthopyroxene granulites are more conducive to estimating conditions of peak metamorphism; equilibration pressures are between 1·0 and 1·65 GPa (30–50 km depth—all depth estimates provided here assume an average crustal density of 2800 kg m^{-3}) at similarly high temperatures (830–1050°C), consistent with the presence of exsolved ternary feldspars in these samples (Fig. 5a). The garnet anorthosite also equilibrated at very high pressures (between 1·1 and 1·75 GPa, 33–52 km) and temperatures (>1050°C) (Fig. 5b). These samples therefore appear to have equilibrated near the Moho of a normal thickness crust or in the lower portion of a thickened crust.

Lashaine

The typical assemblage in the garnet–clinopyroxene granulites of garnet–plagioclase–clinopyroxene–kyanite (Table 1) occurs over a rather restricted P–T interval from 850 to >1200°C and >1·7 GPa, or >51 km depth (see Fig. 5c, for sample 89-727; other garnet–clinopyroxene granulites show similar P–T conditions). However, the thermodynamic calculations suggest that the equilibrium assemblage should also contain quartz, and quartz is not observed in any of the Lashaine samples. This, coupled with the common coronal textures observed in these samples (garnet surrounding clinopyroxene, Fig. 3) suggests that the assemblage is not in equilibrium. Nevertheless, the presence of euhedral kyanite suggests a minimum pressure constraint of 1·6 GPa at ~800°C (Fig. 5c).

Lashaine biotite–garnet granulites (89-733 and 89-745) have equilibrium textures and the mineral assemblages suggest formation at significantly lower pressures (1·3–1·75 GPa) than the garnet–clinopyroxene granulites, at temperatures of 800–950°C (Fig. 5d). Thermobarometry yields even lower pressure–temperature conditions (0·8 GPa and 600°C; Table 3).

Naibor Soito

Interpretation of the peak metamorphic conditions for the Naibor Soito granulites hinges upon whether the biotite is primary or secondary. If the latter, equilibration occurred at higher P and T than if the biotite is primary (e.g. Fig. 5f). Textural evidence suggests that biotite is secondary in some samples where it rims ilmenite (e.g. quartz-free granulite NS04-61), but not in all samples (Table 1). We

Table 3: P–T equilibration conditions for the Tanzanian xenoliths calculated using Fe^{2+}–Mg–Ca exchange thermobarometry

Sample	Type	Cores	Rims			
		For 1 GPa	For 1 GPa		For P_{BKN}	
		T_{BKN}	T_{KR}	T_{BKN}	T_{BKN}	P_{BKN}
Labait						
LB04-04	2px gran	780	–	670	–	–
LB04-12	2px gran	760	–	550	–	–
LB04-16	2px gran	690	–	560	–	–
LB04-19	2px gran	710	–	530	–	–
LB04-34	2px gran	650	–	600	–	–
LB04-38	2px gran	750	–	510	–	–
LB04-41	2px gran	550	–	660	–	–
LB04-50	2px gran	660	–	570	–	–
LB04-52	2px gran	630	–	480	–	–
LB04-53	2px gran	610	–	540	–	–
LB04-93	2px gran	800	–	600	–	–
LB-48	2px gran	770		660	–	–
LB04-07	2px-hbl gran	700	–	850	–	–
LB04-48	2px-hbl gran	660	–	780	–	–
LB04-82	2px-hbl gran	650	–	640	–	–
LB04-27	Anorthosite		830*			
Lashaine						
GPC528†	Gt-cpx gran	–	810	–	–	–
GPC727†	Gt-cpx gran	–	810	–	–	–
GPC728†	Gt-cpx gran	–	780	–	–	–
GPC798†	Gt-cpx gran	–	820	–	–	–
GW808†	Gt-cpx gran	–	780	820	870	2·8
89-727	Gt-cpx gran	–	790	–	–	–
89-729	Gt-cpx gran	–	840	–	–	–
89-730	Gt-cpx gran	–	840	–	–	–
89-731	Gt-cpx gran	–	740	–	–	–
89-734	Gt-cpx gran	–	660	670	700	2·1
89-739	Gt-cpx gran	–	820	–	–	–
89-739	Gt-cpx gran	–	800	–	–	–
89-741	Gt-cpx gran	–	750	800	820	1·7
89-742	Gt-cpx gran	–	830	–	–	–
89-744	Gt-cpx gran	–	810	870	–	–
89-733	Bt gran	–	600	600	600	0·80
89-745	Bt gran	–				
Naibor Soito						
NS04-13	Qtz gran	850	910	830	880	2·6
NS04-91	Qtz gran	830	850	830	870	1·7
NS04-93	Qtz gran	820	940	840	820	1·3
NS04-96	Qtz gran	840		850		
NS04-104	Qtz gran	820		830		
W3S-2	Qtz gran	840		850		
NS04-61	Qtz-free gran	820	910	840	870	2·2
NS04-80	Qtz-free gran	820	890	810	850	1·3

*Calculated using the composition of kelyphite, as no original garnet is preserved.
†Calculated using mineral compositions published by Jones *et al.* (1983*b*).

Downloaded from http://petrology.oxfordjournals.org/ at University of Dar es Salaam on March 8, 2016

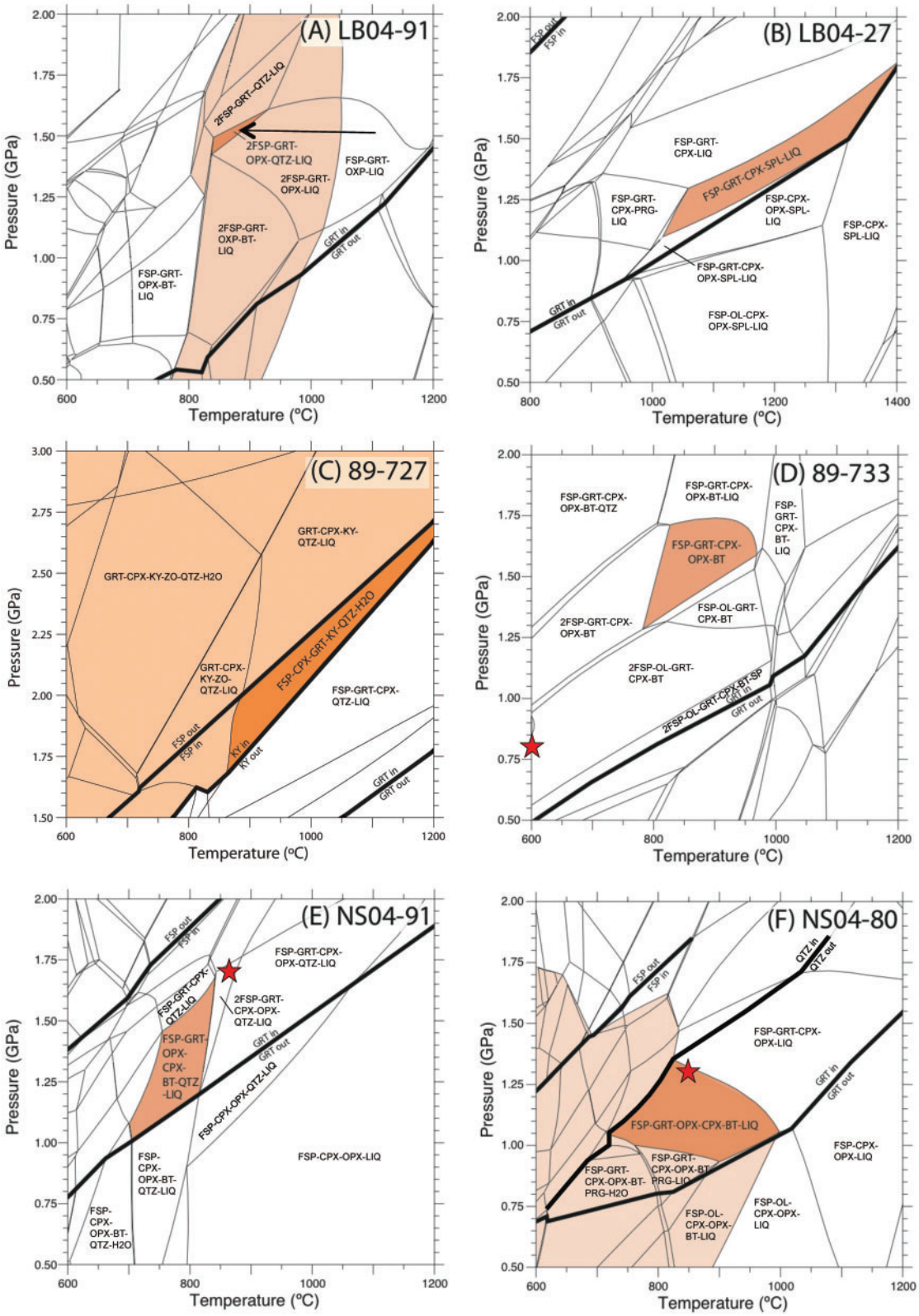


Fig. 5. Pseudosections for selected granulite-facies xenoliths, showing the stability field (dark orange) for the phase assemblage observed in the sample. Major stability fields are labeled; a full listing of stability fields can be found in Fig. L in the Supplementary Data. Dark orange field

(continued)

Downloaded from http://petrology.oxfordjournals.org/ at University of Dar es Salaam on March 8, 2016

therefore assume biotite is primary unless obvious rimming relations are evident. Equilibrium phase assemblage calculations for several of the quartz-bearing granulites, where biotite appears primary, indicate peak metamorphism at 700–850°C and 1·0–1·6 GPa (30–48 km, Fig. 5e). Thermobarometry results for some samples return similar equilibration conditions (Table 3, Fig. 5e); however, the very high pressures indicated for a few samples (e.g. 2·6 GPa for NS04-13) are not supported by the phase assemblage, which should be a kyanite-bearing eclogite at such high pressures (see Supplementary Data Figure M).

In the quartz-free granulites, biotite, if it occurs, generally rims ilmenite (Table 1). These samples therefore typically record higher P–T conditions than the quartz-bearing granulites (e.g. 830 to >1200°C, 1·1–2·0 GPa, 33–60 km, Fig. 5f). Like the quartz-bearing granulites, the phase assemblages observed in the quartz-free granulites do not support the very high equilibration pressure determined for some samples (e.g. 2·2 GPa for NS04-61).

Major and trace elements

Mg-number is calculated as $100\,Mg/(Mg + \sum Fe)$ where Fe and Mg are molar concentrations. Where denoted by the subscript N, trace-element ratios are normalized to chondritic abundances from McDonough & Sun (1995). Major element oxide concentrations cited in the text and plotted in the figures are normalized to 100% anhydrous.

Labait

The major and trace element compositions of the Labait xenoliths are reported in Table 4 and Figs 6–9. Xenoliths from Labait have mafic to intermediate compositions and display compositional variations that correlate with sample type, as described below.

Two-pyroxene granulites. Excluding LB04-46 (see below), these samples have SiO_2 concentrations of 54–57 wt % and Mg-numbers of 47–62. SiO_2/Al_2O_3 ratios, which can be greatly fractionated during crystal accumulation (Kempton & Harmon, 1992), are similar to those of basaltic and andesitic melts that have not experienced crystal accumulation (2·8–3·4) (Fig. 7). Ni and Cr contents are relatively high (107–253 ppm and 65–287 ppm, respectively), as is Sr (521–1042 ppm). Ba concentrations are exceedingly high (630–6730 ppm). The samples are moderately enriched in the light rare earth elements (LREE) [$(La/Yb)_N = 5$–17] and depleted in Nb and Ti (Figs 8 and 9). La/Nb ratios are variable but generally high (1·3–7·2), and Eu anomalies are weak or absent ($Eu/Eu^* = 0·8$–1·2). Despite the LREE, K, Sr and Ba enrichments, the samples are strongly depleted in the highly incompatible elements Cs, Th and U (Fig. 9). Major and trace element compositions are similar to those of high-Mg andesites from the Musoma–Mara Greenstone Belt (Manya *et al.*, 2007) (Fig. 9).

Sample LB04-46 has unusually low SiO_2 (51·5 wt %) and Mg-number (35), and has a SiO_2/Al_2O_3 ratio falling to the left of the field of igneous rocks in Fig. 7. These features are consistent with oxide accumulation and the high modal abundance of opaque phases in this sample (Table 2).

Hornblende two-pyroxene granulites. Relative to the anhydrous two-pyroxene granulites, the hornblende two-pyroxene granulites (LB04-07 and LB04-82) have lower concentrations of SiO_2 (48·7–49·7 wt %), but have similar SiO_2/Al_2O_3 ratios (3·0–3·1) and Mg-numbers (52–56). They have relatively high contents of Fe_2O_3, MgO and

Fig. 5. Continued
generally corresponds to the observed phase assemblage in the sample. Red stars indicate equilibration conditions from thermobarmetry (Table 3), where available. Mineral abbreviations from Kretz (1983), and FSP, feldspar; LIQ, liquid. (a) Labait garnet–orthopyroxene granulite LB04-91, which has an equilibrium assemblage of garnet–orthopyroxene–antiperthitic feldspar and quartz (Table 1), shown by the dark orange field. Pale orange field depicts the region where two feldspars coexist. Arrow indicates possible cooling path from single-feldspar field to two-feldspar field. Bold black line is the garnet-in reaction. Modeled composition (mol %): Si(60)Al(29·7)Fe(8·68) Mg(7·89) Ca(6·22)Na(8·31)K(2·49) H(5)O. (b) Labait anorthosite LB04-27. Equilibrium assemblage contains plagioclase–garnet–clinopyroxene and spinel (Table 1, dark orange field). Bold black line is the garnet-in reaction. Modeled composition (mol %): Si(60)Al(46·96) Fe(3·96)Mg(7·80)Ca(22·40)Na(3·48)H(2)O. (c) Lashaine garnet–clinopyroxene granulite 89-727. This sample contains plagioclase–clinopyroxene–garnet–kyanite, but without quartz (Table 1). Stability fields of kyanite, garnet and feldspar are indicated by bold lines. Pale orange region also marks the kyanite stability field. Garnets form coronae around clinopyroxene (Fig. 3), suggesting garnet growth at the expense of clinopyroxene during burial (see Fig. O in the Supplementary Data for possible P–T path). Modeled composition (mol %): Si(60)Al(26·7)Fe(4·16)Mg(9·89)Ca(12·7)Na(8·35)H(2)O. (d) Lashaine biotite–garnet granulite 89-733. Both biotite–garnet granulites contain plagioclase–biotite–clinopyroxene–orthopyroxene–garnet (Table 1) in apparent textural equilibrium (Fig. 3i, j). Red star is P–T conditions calculated from thermobarometry for this sample (Table 3). The latter does not plot within the mineral stability field. Modeled composition (mol %): Si(60)Al(20·3)Fe(15·3)Mg(9·34)Ca(11·3)Na(6·87)K(3·81)H(2)O. (e) Naibor Soito quartz-bearing granulite NS04-91, which has an equilibrium mineral assemblage of plagioclase–quartz–orthopyroxene–clinopyroxene–garnet–biotite–hornblende (Table 1). Red star is the calculated P–T from thermobarometry for this sample (Table 3), which plots slightly outside the mineral stability field. Feldspar-out and garnet-out reactions are indicated. Modeled composition (mol %): Si(60)Al(19·8)Fe(6·56)Mg(9·89)Ca(8·50)Na(8·11)K(1·19)H(5)O. (f) Naibor Soito quartz-free granulite NS04-80, which has an equilibrium mineral assemblage of plagioclase–clinopyroxene–orthopyroxene–biotite–garnet. The hornblende in this sample (Table 1) rims clinopyroxene and is interpreted as secondary. Garnet-in, quartz-in and feldspar-out reactions are marked as bold black lines. Stability field of biotite is shown as pale orange. Red star is the calculated P–T from thermobarometry for this sample (Table 3), which plots within the equilibrium mineral stability field. Modeled composition (mol %): Si(60)Al(20·0) Fe(9·88)Mg(14·6) Ca(15·2) Na(5·38)K(0·75)H(5)O.

Downloaded from http://petrology.oxfordjournals.org/ at University of Dar es Salaam on March 8, 2016

Table 4: Major and trace element concentrations of the Tanzanian granulite xenoliths

	Labait										
	Two-pyroxene granulites								2px-hbl gran.		Anor.
	LB04-09	LB04-19	LB04-36	LB04-46	LB04-52	LB04-53	LB04-65	LB04-93	LB04-07	LB04-82	LB04-27
SiO_2	53·60	51·63	52·37	48·01	51·15	52·07	52·87	53·67	47·23	48·19	43·53
TiO_2	0·78	0·90	0·81	2·98	0·88	0·85	0·96	0·92	0·97	1·31	0·23
Al_2O_3	17·44	16·00	17·94	16·85	15·66	15·21	15·63	16·41	15·03	15·87	28·91
Fe_2O_3	6·42	8·16	7·10	10·45	8·66	7·97	8·10	7·90	12·07	12·26	3·82
MnO	0·11	0·13	0·11	0·10	0·14	0·12	0·12	0·13	0·21	0·19	0·06
MgO	3·73	6·75	3·19	2·90	7·12	6·67	4·35	5·95	7·89	6·71	3·31
CaO	5·66	6·53	6·34	4·78	6·55	6·86	7·70	6·36	10·23	7·81	15·17
Na_2O	4·07	3·17	2·93	3·96	3·12	3·45	3·67	3·66	2·45	3·26	1·30
K_2O	1·90	1·54	2·58	2·13	1·29	1·56	1·76	2·06	0·84	1·02	0·38
P_2O_5	0·25	0·29	0·16	1·01	0·35	0·31	0·21	0·33	0·09	0·42	0·10
LOI	2·78	1·65	4·86	2·48	1·13	1·54	1·97	1·02	1·06	1·49	1·63
Trace	0·98	0·83	0·24	0·89	0·87	0·78	0·50	0·38	0·27	0·37	0·24
Total	97·74	97·58	98·63	96·53	96·93	97·38	97·85	98·78	98·33	98·90	98·68
Mg-no.	53·5	62·1	47·1	35·5	62·0	62·4	51·5	59·9	56·4	52·0	63·2
SiO_2/Al_2O_3	3·1	3·2	2·9	2·8	3·3	3·4	3·4	3·3	3·1	3·0	1·5
XRF											
Sc[1]	15	22	17	11	25	24	27	21	39	35	13
V[1]	114	138	92	147	162	159	163	154	263	209	80
Cr[1]	78	254	65	40	287	284	161	228	265	138	48
Ni[1]	253	197	107	410	205	169	122	194	202	102	97
Cu[1]	b.d.	25	18	42	33	44	25	32	51	25	18
Zn[1]	81	98	72	125	109	101	98	97	102	166	33
Ga[1]	25	21	19	23	21	18	21	22	18	26	19
Rb[1]	22	25	75	21	14	22	27	20	11	17	11
Sr[1]	1042	735	521	723	547	722	703	849	524	1044	436
Y	12	16	19	16	16	15	20	13	26	28	4
Zr[1]	121	124	268	525	80	92	193	109	53	111	29
Nb	3	4	8	20	4	4	7	9	5	10	7
Ba[1]	6726	5448	631	5243	5957	4935	2546	1345	531	927	1211
La	18	19	16	61	20	30	19	12	b.d.	32	b.d.
Ce	40	49	27	141	44	61	45	37	14	80	b.d.
Nd	22	29	15	77	32	36	33	21	11	46	7
Pb[1]	10	8	b.d.	14	6	9	6	9	b.d.	7	b.d.
Th	3	b.d.	b.d.	b.d.	b.d.	b.d.	b.d.	b.d.	b.d.	b.d.	b.d.
ICP-MS											
Sc	–	9·75	2·86	–	18·0	19·6	19·5	17·4	22·2	29·3	8·49
V	–	139	88·4	–	117	140	150	156	234	194	89·4
Cr	–	256	74·2	–	262	263	145	221	229	137	96·9
Co[1]	–	33·6	18·8	–	34·1	28·3	25·2	28·9	42·6	32·2	19·7
Cu	–	20·4	45·1	–	31·4	33·4	38·8	260	37·7	15·5	18·5
Rb	–	23·3	59·0	–	14·0	21·2	24·5	18·7	10·0	15·3	10·4
Sr	–	688	462	–	573	701	672	868	440	960	462
Y[1]	–	14·1	15·9	–	15·8	12·9	17·5	11·8	20·1	23·9	2·96

(continued)

Downloaded from http://petrology.oxfordjournals.org/ at University of Dar es Salaam on March 8, 2016

Table 4: Continued

	Labait										
	Two-pyroxene granulites								2px–hbl gran.		Anor.
	LB04-09	LB04-19	LB04-36	LB04-46	LB04-52	LB04-53	LB04-65	LB04-93	LB04-07	LB04-82	LB04-27
ICP-MS (continued)											
Zr	–	83	120	–	67	78	110	87	50	80	27
Nb[1]	–	4·59	10·3	–	3·20	3·90	6·33	11·2	4·37	11·4	–
Cs	–	0·10	0·036	–	0·033	0·057	0·046	0·078	0·020	0·016	0·23
Ba	–	5521	1331	–	11399	8771	4359	2417	458	1354	1659
La[1]	–	23·2	13·9	–	19·3	28·0	15·7	14·9	6·0	30·8	3·65
Ce[1]	–	55·6	28·0	–	48·4	62·4	42·3	33·8	16·7	76·2	7·24
Pr[1]	–	6·79	3·55	–	7·21	8·38	6·35	4·39	2·46	10·52	0·84
Nd[1]	–	29·7	15·2	–	33·1	36·0	29·4	19·7	11·3	44·6	3·37
Sm[1]	–	6·10	3·67	–	7·01	6·97	6·48	4·25	3·04	9·56	0·68
Eu[1]	–	2·2	1·3	–	1·7	1·7	1·6	1·6	1·0	2·0	0·3
Gd[1]	–	5·03	4·02	–	5·67	5·41	5·43	3·64	3·69	8·19	0·73
Tb[1]	–	0·67	0·63	–	0·74	0·68	0·74	0·49	0·64	1·10	0·10
Dy[1]	–	3·35	3·73	–	3·60	3·14	3·72	2·51	4·12	5·40	0·54
Ho[1]	–	0·61	0·73	–	0·66	0·54	0·68	0·47	0·86	0·96	0·10
Er[1]	–	1·67	2·07	–	1·79	1·44	1·81	1·28	2·54	2·58	0·30
Tm[1]	–	0·22	0·29	–	0·23	0·18	0·23	0·17	0·37	0·33	0·04
Yb[1]	–	1·40	1·89	–	1·43	1·09	1·42	1·08	2·43	2·06	0·26
Lu[1]	–	0·20	0·27	–	0·20	0·15	0·19	0·15	0·35	0·28	0·036
Hf[1]	–	2·21	2·77	–	1·92	2·08	2·72	2·15	1·53	2·34	0·51
Pb	–	10·60	3·59	–	6·94	9·53	7·19	12·60	2·59	7·30	1·32
Th[1]	–	0·091	0·077	–	0·11	0·093	0·16	0·11	0·23	1·57	0·27
U[1]	–	0·037	0·089	–	0·044	0·027	0·084	0·16	0·12	0·28	0·12
K/Rb	720	510	286	858	787	578	548	862	648	513	280
Rb/Cs	–	259	2078	–	419	396	579	252	539	1048	50
Ba/Rb	306	217	8·4	255	437	220	95·5	67·9	49·3	56·0	106
Ti/V	41	39	53	122	33	32	35	36	22	38	17
Th/U	–	2·5	0·9	–	2·6	3·5	1·9	0·7	2·0	5·6	2·2
Sr/Y	86	46	28	46	34	48	35	64	20	37	114
La/Nb	–	5·1	1·4	–	6·0	7·2	2·5	1·3	1·4	2·7	–
La/Yb_n	–	11·3	5·0	–	9·2	17·4	7·5	9·4	1·7	10·2	9·7
La/Sm_n	–	2·4	2·4	–	1·7	2·5	1·5	2·2	1·2	2·0	3·3
Gd/Yb_n	–	2·9	1·7	–	3·2	4·0	3·1	2·7	1·2	3·2	2·3
Eu/Eu*	–	1·2	1·0	–	0·8	0·9	0·8	1·2	0·9	0·7	1·5

(continued)

Downloaded from http://petrology.oxfordjournals.org/ at University of Dar es Salaam on March 8, 2016

Table 4: Continued

	Labait		Lashaine									
	Gt-opx gran.		Gt-cpx granulites								Bt-Gt gran.	
	LB04-39	LB04-91	89-726	89-727	89-729	89-730	89-731	89-732	89-734	89-735	89-733	89-745
SiO_2	51·73	50·43	50·96	51·60	52·46	49·28	52·43	52·62	47·33	53·41	46·31	46·55
TiO_2	0·84	1·18	0·36	0·30	0·36	0·52	0·39	0·33	0·81	0·17	3·15	2·71
Al_2O_3	18·37	21·18	17·69	19·47	22·67	16·56	22·56	19·65	15·51	22·31	13·28	13·03
Fe_2O_3	8·36	9·69	4·82	4·76	4·26	9·16	4·20	4·62	14·86	3·36	15·72	14·76
MnO	0·13	0·17	0·09	0·10	0·06	0·16	0·06	0·07	0·19	0·05	0·23	0·22
MgO	5·39	4·45	6·40	5·71	2·86	8·01	2·91	5·01	8·39	4·11	4·83	5·24
CaO	4·95	4·88	11·99	10·20	9·53	10·99	9·48	10·86	9·14	8·61	8·11	7·90
Na_2O	2·40	3·60	3·45	3·70	4·46	3·03	4·45	3·98	2·25	4·94	2·74	3·21
K_2O	2·42	1·64	0·53	0·84	0·63	0·46	0·64	0·76	0·22	0·74	2·30	2·81
P_2O_5	0·21	0·08	0·10	0·04	0·05	0·03	0·06	0·12	0·06	0·16	0·59	0·51
LOI	3·43	1·04	2·26	2·57	1·98	1·32	1·96	2·39	1·84	1·83	1·91	2·23
Trace	0·45	0·39	0·30	0·30	0·23	0·26	0·24	–	–	–	0·30	0·30
Total	98·69	98·74	98·93	99·59	99·54	99·79	99·37	100·41	100·60	99·69	99·47	99·48
Mg-no.	56·1	47·6	72·5	70·4	68·2	63·4	57·9	68·2	52·8	70·8	37·9	41·3
SiO_2/Al_2O_3	2·8	2·4	2·9	2·7	2·3	3·0	2·3	2·7	3·1	2·4	3·5	3·6
XRF												
Sc[1]	29	26	24	17	9	32	10	19	32	10	30	29
V[1]	171	190	125	86	40	233	42	95	281	46	261	230
Cr[1]	382	320	395	219	31	334	35	212	399	112	119	195
Ni[1]	278	165	230	133	18	153	19	123	285	62	74	93
Cu[1]	66	120	145	70	b.d.	52	29	75	46	17	121	109
Zn[1]	95	151	30	34	23	52	43	40	100	39	157	140
Ga[1]	19	30	15	17	18	16	17	15	17	17	21	20
Rb[1]	69	28	14	25	17	8	16	18	7	9	75	67
Sr[1]	502	886	1160	1365	1417	927	1440	1506	119	1760	371	279
Y	29	22	7	5	b.d.	5	2	4	17	b.d.	48	44
Zr[1]	117	253	11	12	6	13	7	37	10	39	280	242
Nb	8	15	b.d.	3	b.d.	3	b.d.	5	4	4	22	18
Ba[1]	1904	859	192	408	301	192	315	478	35	410	676	752
La	16	30	b.d.	b.d.	b.d.	b.d.	b.d.	b.d.	10	b.d.	31	33
Ce	29	47	13	12	b.d.	b.d.	b.d.	b.d.	b.d.	14	80	71
Nd	12	15	7	7	b.d.	b.d.	b.d.	b.d.	b.d.	b.d.	43	39
Pb[1]	12	12	b.d.	6	5	5	4	b.d.	b.d.	b.d.	13	14
Th	b.d.	b.d.	b.d.	3	3	b.d.	3	b.d.	b.d.	b.d.	6	5
ICP-MS												
Sc	15·4	24·2	21·0	3·29	5·55	18·4	–	14·8	28·5	6·01	15·7	29·0
V	126	196	140	74·1	48·7	206	–	94·2	245	53·2	235	224
Cr	253	324	414	181	74·8	247	–	215	318	163	132	197
Co[1]	33·1	36·1	27·9	24·9	19·8	41·1	–	25·4	60·4	17·2	42·2	42·9
Cu	55·6	116	130	145	8·9	92·4	–	75·7	44·5	16·7	110	112
Rb	44·6	26·4	14·6	17·1	15·9	7·74	–	19·2	7·33	9·62	67·0	67·3
Sr	441	838	1186	996	1456	825	–	1696	239	1789	332	482
Y[1]	25·1	22·1	5·83	2·90	1·08	3·73	–	4·21	13·6	1·77	39·3	36·5

(continued)

Downloaded from http://petrology.oxfordjournals.org/ at University of Dar es Salaam on March 8, 2016

Table 4: Continued

	Labait		Lashaine									
	Gt-opx gran.		Gt-cpx granulites								Bt-Gt gran.	
	LB04-39	LB04-91	89-726	89-727	89-729	89-730	89-731	89-732	89-734	89-735	89-733	89-745
ICP-MS (continued)												
Zr	108	143	11·1	12·3	5·96	11·1	–	30·9	29·2	6·84	280	260
Nb[1]	7·29	9·96	0·72	4·16	–	3·81	–	–	–	–	25·6	–
Cs	0·29	0·12	0·057	0·043	0·19	0·079	–	0·037	0·18	0·042	2·09	0·72
Ba	2565	1488	213	598	416	184	–	649	54	470	630	1013
La[1]	13·4	24·9	3·35	4·81	2·07	2·80	–	4·60	3·20	3·73	34·0	34·4
Ce[1]	25·9	41·8	6·75	7·66	3·01	5·32	–	7·61	4·75	4·65	83·0	68·3
Pr[1]	2·36	3·98	0·97	0·97	0·46	0·75	–	1·14	0·77	0·57	10·1	–
Nd[1]	8·86	14·1	4·62	4·03	1·94	3·29	–	4·95	3·69	2·09	42·3	42·5
Sm[1]	2·45	3·17	1·26	0·89	0·39	0·83	–	1·18	1·29	0·35	9·43	8·94
Eu[1]	1·2	1·6	0·7	0·6	0·6	0·5	–	0·7	0·6	0·5	2·4	2·2
Gd[1]	3·78	4·13	1·44	0·90	0·38	0·95	–	1·26	2·02	0·36	9·47	8·93
Tb[1]	0·67	0·66	0·22	0·13	0·048	0·15	–	0·19	0·41	0·045	1·47	1·41
Dy[1]	4·51	3·92	1·26	0·73	0·24	0·88	–	1·03	2·79	0·24	8·49	8·10
Ho[1]	0·95	0·77	0·24	0·14	0·041	0·17	–	0·19	0·60	0·05	1·67	1·58
Er[1]	2·77	2·20	0·63	0·36	0·10	0·47	–	0·50	1·78	0·13	4·78	4·66
Tm[1]	0·41	0·32	0·082	0·047	0·012	0·063	–	0·064	0·27	0·018	0·67	0·65
Yb[1]	2·77	2·16	0·52	0·29	0·075	0·40	–	0·40	1·78	0·12	4·37	4·18
Lu[1]	0·40	0·33	0·069	0·040	0·010	0·056	–	0·054	0·26	0·018	0·62	0·60
Hf[1]	2·43	3·66	0·42	0·36	0·14	0·41	–	0·65	0·92	0·16	6·75	6·60
Pb	16·3	16·2	3·07	4·02	3·55	3·40	–	4·58	4·69	2·63	17·8	12·2
Th[1]	0·10	0·32	0·07	0·22	0·12	0·17	–	0·27	0·25	0·20	6·87	10·15
U[1]	0·11	0·26	0·15	0·050	0·042	0·055	–	0·11	0·04	0·08	1·69	1·83
K/Rb	290	494	319	283	308	481	326	345	277	698	256	347
Rb/Cs	239	225	245	576	91	102	–	496	36	209	36	93
Ba/Rb	27·4	31·1	13·8	16·6	17·6	24	19·3	26·1	5·3	47	9·1	11·2
Ti/V	29	37	17	21	21	54	56	22	13	17	73	71
Th/U	0·9	1·3	0·5	4·4	2·8	3·2	–	2·4	7·0	2·6	4·1	5·6
Sr/Y	17	39	170	286	1306	184	734	430	7	994	8	6
La/Nb	1·8	2·5	4·7	1·2	–	0·7	–	–	–	–	1·3	–
La/Yb_n	3·3	7·8	4·4	11·1	18·9	4·7	–	7·8	1·2	21·4	5·3	5·6
La/Sm_n	3·4	4·9	1·7	3·4	3·3	2·1	–	2·4	1·6	6·6	2·2	2·4
Gd/Yb_n	1·1	1·5	2·3	2·5	4·1	1·9	–	2·6	0·9	2·4	1·8	1·7
Eu/Eu*	1·2	1·4	1·6	1·9	4·6	1·6	–	1·8	1·2	3·9	0·8	0·8

(continued)

Downloaded from http://petrology.oxfordjournals.org/ at University of Dar es Salaam on March 8, 2016

Table 4: Continued

	Naibor Soito									
	Quartz granulites							Quartz-free granulites		
	NS04-01	NS04-05	NS04-13	NS04-73	NS04-83	NS04-91	NS04-98	NS04-150	NS04-61	NS04-80
SiO_2	56·20	53·70	65·30	57·88	61·26	55·54	56·40	49·01	50·08	49·52
TiO_2	0·78	0·67	0·14	0·69	0·47	0·78	0·78	0·86	1·01	0·67
Al_2O_3	16·19	17·47	16·49	16·37	17·07	15·56	15·12	15·88	13·68	14·02
Fe_2O_3	5·51	6·16	1·81	5·76	3·66	8·07	7·44	9·01	11·59	10·84
MnO	0·14	0·08	0·03	0·08	0·06	0·18	0·14	0·14	0·21	0·21
MgO	3·00	4·46	1·55	2·68	1·59	6·14	4·85	6·49	7·58	8·07
CaO	6·89	6·04	5·61	6·73	5·77	7·35	7·15	8·27	9·86	11·70
Na_2O	3·56	4·60	4·82	4·61	5·41	3·87	4·27	3·94	2·62	2·29
K_2O	2·37	1·41	0·98	0·96	0·91	0·86	1·00	1·30	0·83	0·48
P_2O_5	0·38	0·39	0·07	0·22	0·29	0·18	0·21	0·68	0·24	0·22
LOI	1·91	2·39	0·57	1·74	1·51	0·35	1·17	1·86	0·81	0·79
Trace	0·24	0·35	0·14	0·20	0·19	0·20	0·21	0·42	0·23	0·19
Total	97·16	97·72	97·53	97·92	98·18	99·09	98·75	97·86	98·75	99·00
Mg-no.	51·9	58·9	62·8	47·9	46·2	60·1	56·4	58·8	56·4	59·6
SiO_2/Al_2O_3	3·5	3·1	4·0	3·5	3·6	3·6	3·7	3·1	3·7	3·5
XRF										
Sc[1]	18	13	6	13	8	23	28	26	42	46
V[1]	115	105	23	99	57	140	129	170	249	242
Cr[1]	76	108	22	24	10	164	118	233	252	307
Ni[1]	40	50	19	24	20	65	79	84	117	95
Cu[1]	b.d.	33	b.d.	17	b.d.	23	27	22	36	33
Zn[1]	86	105	19	73	49	112	101	118	90	83
Ga[1]	20	20	17	20	19	20	22	23	15	14
Rb[1]	51	23	3	18	15	5	7	25	16	9
Sr[1]	503	1054	399	783	734	315	473	1146	597	241
Y	21	6	2	8	4	15	23	27	20	18
Zr[1]	196	322	34	170	143	189	176	200	68	42
Nb	8	4	b.d.	3	3	7	10	6	5	5
Ba[1]	697	1001	658	356	454	392	374	1120	207	328
La	27	23	9	11	10	33	26	56	b.d.	b.d.
Ce	46	39	b.d.	26	25	62	57	117	22	18
Nd	22	16	b.d.	12	9	25	30	63	13	9
Pb[1]	9	8	8	4	5	5	6	8	4	b.d.
Th	b.d.	b.d.	b.d.	b.d.	b.d.	b.d.	b.d.	3	b.d.	b.d.
ICP-MS										
Sc	13·8	11·2	2·73	10·6	6·05	21·7	26·8	–	43·1	49·8
V	119	92·5	25·6	115	70·7	149	110	–	270	223
Cr	97·1	108	43·8	41·1	31·9	188	128	–	275	322
Co[1]	23·4	20·4	6·4	14·1	9·7	35·9	25·9	–	50·2	51·4
Cu	8·0	31·6	11·2	19·2	7·8	27·4	27·3	–	41·6	33·7
Rb	25·6	19·1	2·12	13·1	15·7	5·25	6·41	–	17·0	10·8
Sr	470	892	373	789	785	329	490	–	652	264
Y[1]	20·9	5·17	1·51	8·89	4·17	15·0	23·9	–	20·7	18·2

(continued)

Downloaded from http://petrology.oxfordjournals.org/ at University of Dar es Salaam on March 8, 2016

Table 4: Continued

	Naibor Soito									
	Quartz granulites							Quartz-free granulites		
	NS04-01	NS04-05	NS04-13	NS04-73	NS04-83	NS04-91	NS04-98	NS04-150	NS04-61	NS04-80
ICP-MS (continued)										
Zr	125	35	20	64	112	62	44	–	50	31
Nb[1]	7·39	4·77	0·73	4·36	4·61	7·56	12·1	–	6·91	6·22
Cs	0·11	0·060	0·015	0·087	0·032	0·029	0·032	–	0·18	0·077
Ba	601	1262	727	365	552	443	421	–	233	383
La[1]	25·0	21·9	4·94	12·7	12·6	33·3	27·5	–	10·2	7·8
Ce[1]	49·8	38·1	7·08	24·2	21·7	67·6	57·6	–	22·2	15·1
Pr[1]	5·78	4·24	0·64	3·25	2·52	7·79	7·41	–	3·24	2·06
Nd[1]	22·1	15·5	2·30	13·2	9·34	27·5	30·2	–	13·9	9·04
Sm[1]	4·57	2·43	0·37	2·56	1·54	4·44	6·40	–	3·37	2·37
Eu[1]	1·4	1·8	0·8	1·2	0·9	1·2	1·1	–	1·0	0·8
Gd[1]	4·99	2·55	0·46	2·62	1·64	4·90	6·39	–	3·50	2·64
Tb[1]	0·69	0·24	0·050	0·33	0·18	0·55	0·87	–	0·60	0·48
Dy[1]	3·86	1·00	0·26	1·70	0·82	2·80	4·67	–	3·67	3·10
Ho[1]	0·77	0·18	0·052	0·32	0·15	0·55	0·88	–	0·75	0·66
Er[1]	2·18	0·57	0·16	0·92	0·43	1·60	2·42	–	2·15	1·93
Tm[1]	–	–	–	–	–	–	–	–	–	–
Yb[1]	1·96	0·51	0·14	0·77	0·35	1·42	2·02	–	2·04	1·94
Lu[1]	0·28	0·074	0·021	0·11	0·049	0·20	0·28	–	0·29	0·28
Hf[1]	3·11	0·85	0·52	1·70	2·44	1·70	1·43	–	1·61	1·14
Pb	7·58	8·44	8·76	3·84	4·84	7·26	8·02	–	3·77	2·46
Th[1]	1·67	0·12	0·069	0·13	0·058	1·23	0·93	–	0·36	0·42
U[1]	0·89	0·20	0·051	0·14	0·26	0·12	0·17	–	0·27	0·23
K/Rb	383	505	2567	433	490	1501	1240	432	427	449
Rb/Cs	481	387	210	213	480	163	209	–	87	116
Ba/Rb	14	43	207	19	30	82	56	45	13	37
Ti/V	41	38	38	42	49	33	36	30	24	17
Th/U	1·9	0·6	1·4	1·0	0·2	10·2	5·5	–	1·3	1·8
Sr/Y	23	183	182	93	182	21	20	42	30	13
La/Nb	3·4	4·6	6·8	2·9	2·7	4·4	2·3	–	1·5	1·3
La/Yb_n	8·7	29·3	23·4	11·3	24·7	16·0	9·3	–	3·4	2·7
La/Sm_n	3·4	5·6	8·2	3·1	5·1	4·7	2·7	–	1·9	2·1
Gd/Yb_n	2·1	4·1	2·6	2·8	3·8	2·8	2·6	–	1·4	1·1
Eu/Eu*	0·9	2·2	6·1	1·4	1·7	0·8	0·5	–	0·9	0·9

[1]Preferred value.
–, element was not measured. LOI, loss on ignition. Mg-number = $100\,Mg/(Mg + Fe_T)$, using molar concentrations, and where Fe_T is total Fe. b.d., element present in concentrations below the lower limit of determination. $Eu/Eu^* = Eu_n/(Sm_n + Gd_n)^{0.5}$, where subscript 'n' denotes chondrite-normalized value.

CaO, and lower K_2O (0·8–1·2 wt %), and overlap in major element compositions with basalts from the Tanzanian Craton greenstone belts (Fig. 6). Like the anhydrous two-pyroxene granulites, concentrations of Ni (102–202 ppm) and Cr (138–265 ppm) are high and concentrations of Cs, Th, U, Nb and Ti are depleted relative to adjacent elements (La/Nb = 1·4–2·7). However, Th and U show variable depletions that are not as severe as in the anhydrous two-pyroxene granulites. REE patterns for the hornblende-bearing granulites are also distinct (Fig. 8). LB04-07 has a

Downloaded from http://petrology.oxfordjournals.org/ at University of Dar es Salaam on March 8, 2016

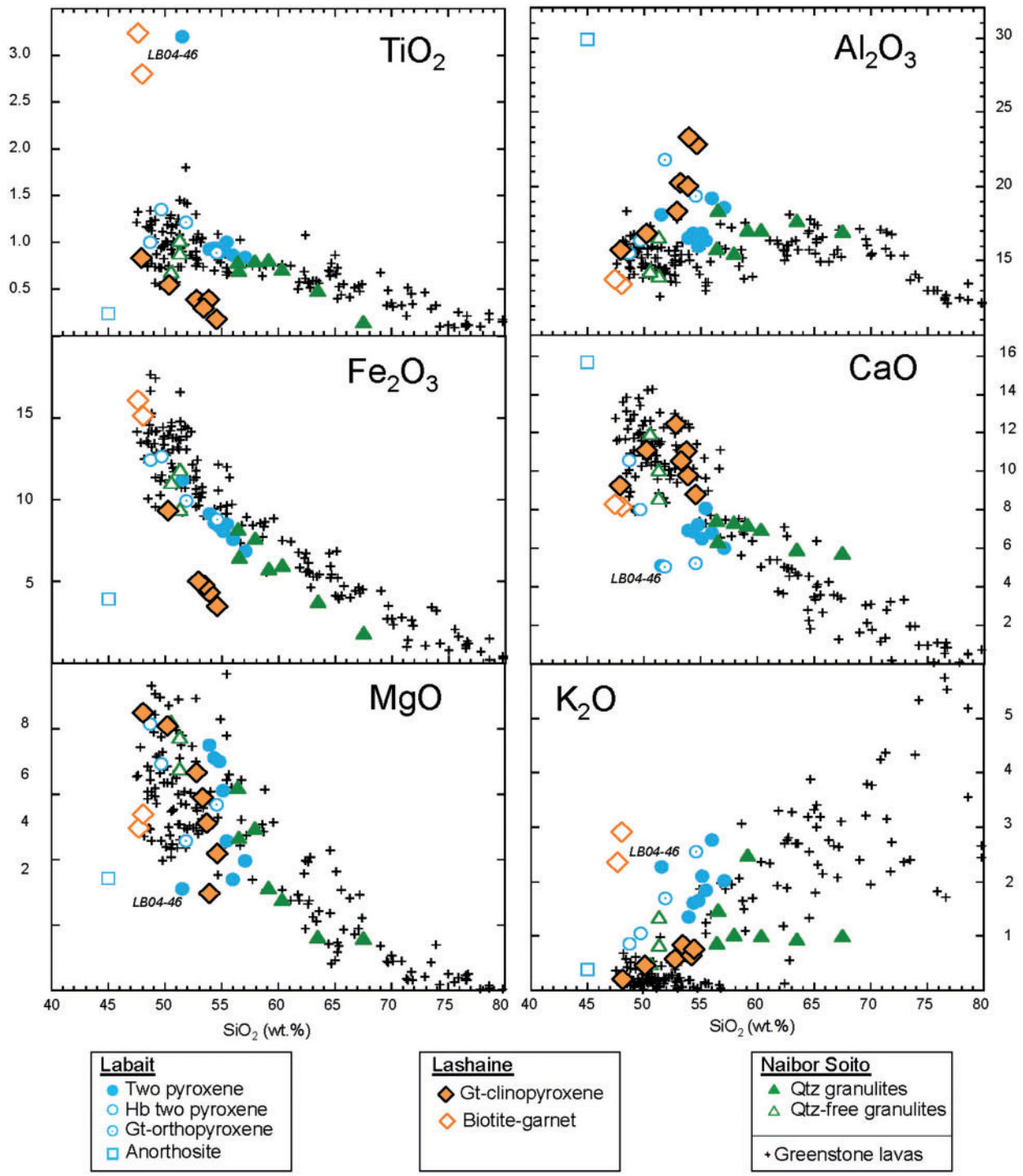


Fig. 6. Harker variation diagrams for major oxides showing whole-rock granulite xenoliths compared with lavas from the Tanzanian Craton. Lava data are from Manya (2004), Manya & Maboko (2008*a*, 2008*b*) and Mtoro *et al.* (2009). Sample LB04-46 is a Labait two-pyroxene granulite that is oxide-rich and probably experienced cumulate enrichment of oxide and apatite.

flat REE pattern [$(La/Yb)_N = 1{\cdot}7$] with no Eu anomaly, similar to those of the greenstone belt basalts, whereas LB04-82 is LREE-enriched [$(La/Yb)_N = 10{\cdot}2$] and has a negative Eu anomaly.

Garnet–orthopyroxene granulites. LB04-39 and LB04-91 have similar SiO_2 and Mg-numbers to the two-pyroxene granulites ($SiO_2 = 51$–55 wt %, Mg-number = 48–56), but have higher contents of Al_2O_3 (19·4–21·8 wt %, compared with

Downloaded from http://petrology.oxfordjournals.org/ at University of Dar es Salaam on March 8, 2016

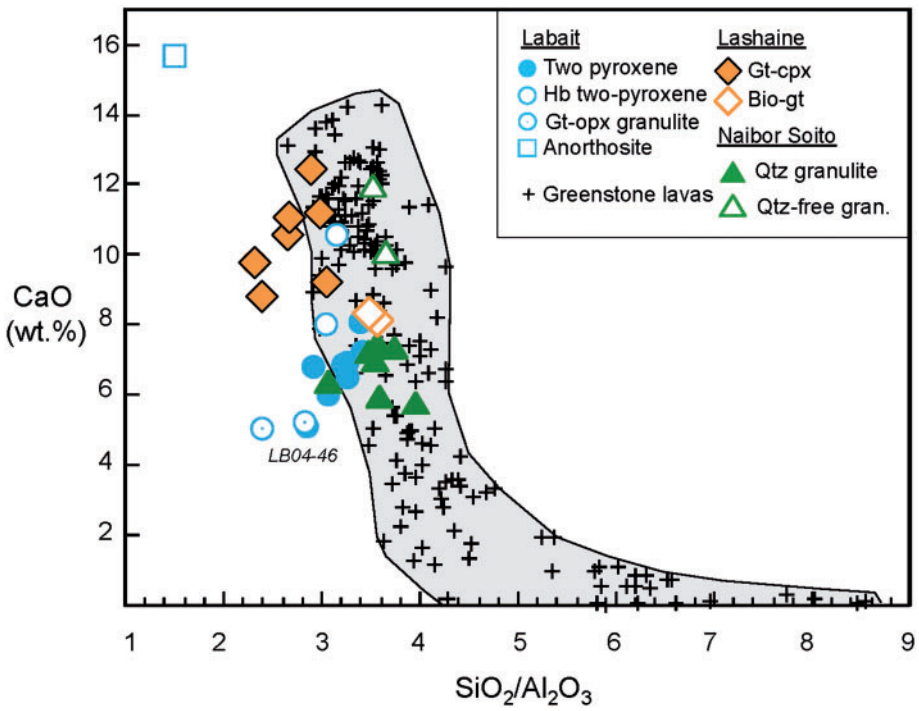


Fig. 7. SiO_2/Al_2O_3 vs CaO (wt %) for the whole-rock granulite xenoliths compared with lavas from the Tanzanian Craton. The SiO_2/Al_2O_3 ratio can be used to discriminate cumulates from lavas (Kempton & Harmon, 1992). All data are normalized to 100% anhydrous. Data sources are the same as for Fig. 5.

16·0–19·2 wt %), Y and the heavy REE (HREE), and lower CaO contents (~5·1 compared with 6·0–8·1 wt %) (Figs 6, 8 and 9). Low SiO_2/Al_2O_3 ratios suggest crystal accumulation (Fig. 7) (Kempton & Harmon, 1992). Incompatible trace element patterns are comparable with those of the two-pyroxene granulites, showing LREE enrichment [$(La/Yb)_N = 3·3–7·8$], strong enrichment in Sr (500–890 ppm), K_2O (1·6–2·4 wt %) and Ba (860–1900 ppm), and depletion in Nb and Ti ($La/Nb_N = 1·8–2·5$). Cs, Th and U are also depleted relative to elements of similar incompatibility, but not to the degree seen in the anhydrous two-pyroxene granulites. Nickel (165–278 ppm) and Cr (320–385 ppm) concentrations are also high. Both garnet–orthopyroxene granulites have small, positive Eu anomalies ($Eu/Eu^* = 1·2–1·4$) and flat HREE patterns ($Gd/Yb_N = 1·1–1·5$).

Anorthosite. LB04-27 is compositionally distinct from any other Tanzanian lower crustal xenolith considered here. It has high concentrations of Al_2O_3 and CaO and low concentrations of TiO_2, Fe_2O_3, MgO, Na_2O and K_2O relative to the two-pyroxene granulites, but its Mg-number (63) is similar. Concentrations of Ni, Cr, Sr, Y and the REE are low, and the trace element pattern for this sample has positive Sr and Eu anomalies (Fig. 9). Its Ba content is high, but not extreme (1210 ppm).

Lashaine

Major and trace element compositions of the Lashaine xenoliths are reported in Table 4 and plotted in Figs 6, 7, 10 and 11.

Garnet–clinopyroxene granulites. These samples are mafic ($SiO_2 = 47·9–54·6$ wt %, Mg-number = 53–72) and their compositions reflect the modal proportions of plagioclase and clinopyroxene in each sample (Table 2); the most plagioclase-rich samples have the highest SiO_2 contents and the lowest concentrations of Fe, Mg and most incompatible trace elements. Compared with the greenstone belt lavas from the Tanzanian Craton, the Lashaine garnet–clinopyroxene granulites range to higher Al_2O_3, lower TiO_2 and Fe_2O_3, and lower SiO_2/Al_2O_3 ratios (2·3–3·1, Figs 6 and 7). Incompatible trace element abundances are also relatively low, with the exceptions of Sr and Eu, which define large, positive anomalies on normalized incompatible element patterns for these samples ($Eu/Eu^* = 1·2–4·6$, Fig. 11). These features reflect their likely origin as plagioclase-bearing cumulates. Trace element patterns are otherwise qualitatively similar to those in the Labait two-pyroxene granulites; most samples are LREE-enriched, with $(La/Yb)_N$ of 4·4–21·4, and are depleted in Cs, Th and U (Fig. 11). The highest $(La/Yb)_N$ values occur in the most plagioclase-rich samples, consistent with plagioclase accumulation.

Biotite–garnet granulites. Samples 89-733 and 89-745, although mafic, are distinct from the other granulites at Lashaine, Labait or Naibor Soito. They have very low Mg-numbers (38–41), very high TiO_2, P_2O_5 and K_2O (for their SiO_2 contents), and relatively high Fe_2O_3 (Fig. 6).

Downloaded from http://petrology.oxfordjournals.org/ at University of Dar es Salaam on March 8, 2016

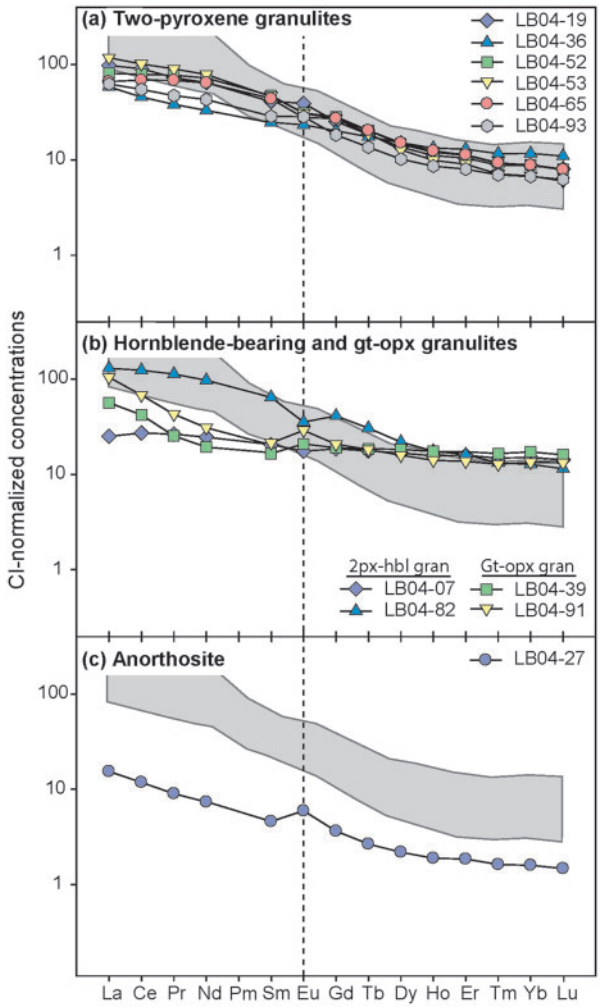


Fig. 8. Chondrite-normalized REE patterns of Labait granulite xenoliths. Gray field in the background shows the range of data for high-Mg andesites from the Musoma–Mara Greenstone Belt (Manya *et al.*, 2007). Chondrite values from McDonough & Sun (1995).

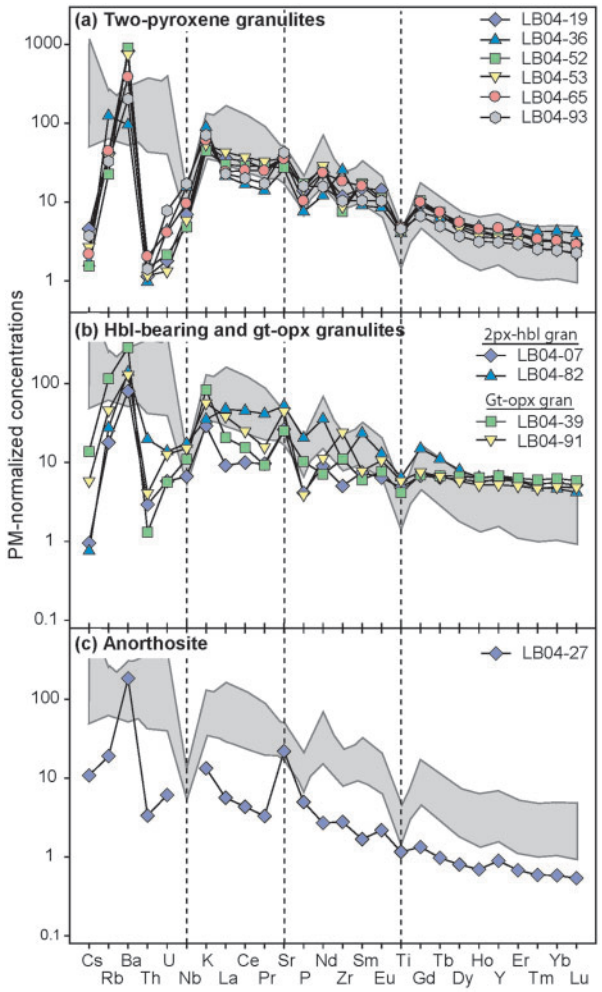


Fig. 9. Primitive mantle normalized trace element patterns for Labait granulite xenoliths compared with high-magnesium andesites from the Musoma–Mara Greenstone Belt (gray field; Manya *et al.*, 2007). Primitive mantle values are from McDonough & Sun (1995).

Their SiO_2/Al_2O_3 ratios are similar to those in basaltic melts (3·4–3·5) (Fig. 7) and their major element compositions fall within the field of alkaline basalts (see Supplementary Data Fig. N). Incompatible trace element contents are very high, including Cs, Th and U (Fig. 11); these are depleted in all other granulites in this study. Trace element patterns in the biotite–garnet granulites are smooth and LREE-enriched [$(La/Yb)_N = 5·3–5·6$], with small negative Nb ($La/Nb = 1·3–1·5$), Sr and Eu anomalies ($Eu/Eu^* = 0·8$). Ti/V ratios are very high (71–73), distinct from most other Tanzanian granulites, but similar to modern ocean-island basalts (Shervais, 1982).

Naibor Soito

Major and trace element compositions of the Naibor Soito xenoliths are reported in Table 4 and plotted in Figs 6, 7, 12 and 13. Like the Labait two-pyroxene granulites, samples from this locality are mafic to intermediate in composition and have major element compositions similar to those of the greenstone belt lavas (Fig. 6). Concentrations of most trace elements, including Ni (19–79 ppm), Cr (10–164 ppm), Y (2–23 ppm) and Yb (0·14–13·0 ppm), span a wide range and correlate with SiO_2 and MgO, following the differentiation trends seen in the lavas.

Quartz-bearing granulites. Wide ranges in trace element abundances are apparent in the quartz-bearing xenoliths (Figs 12 and 13). On the REE diagram, Eu anomalies range from negative to strongly positive ($Eu/Eu^* = 0·5–6·1$), with the largest anomaly occurring in the most evolved sample, NS04-13 (Fig. 12). Despite the wide range of concentrations, the trace element patterns of the quartz-bearing granulites share several key features with

Downloaded from http://petrology.oxfordjournals.org/ at University of Dar es Salaam on March 8, 2016

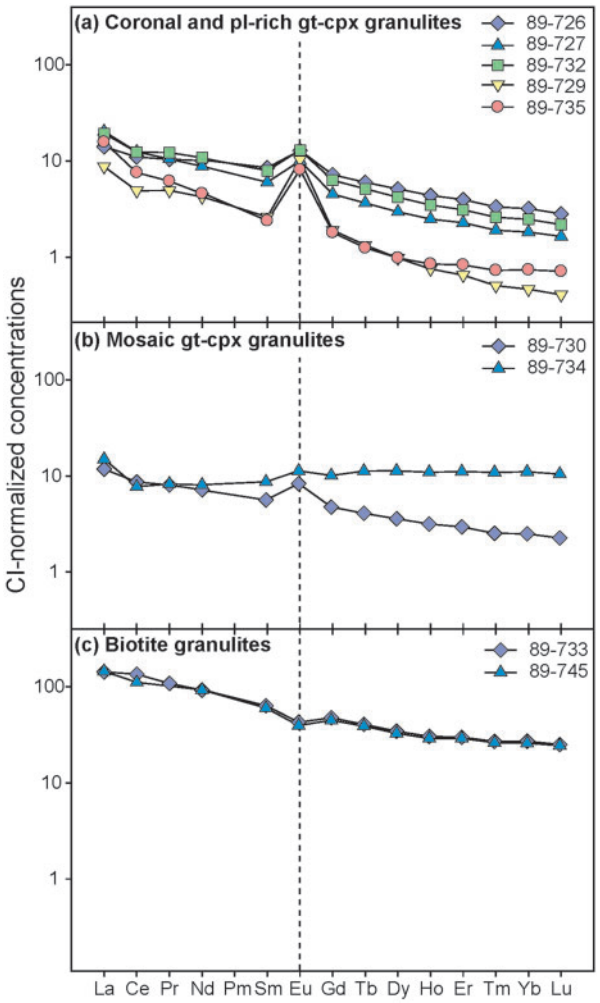


Fig. 10. Chondrite-normalized REE patterns of Lashaine granulite xenoliths. Chondrite values from McDonough & Sun (1995).

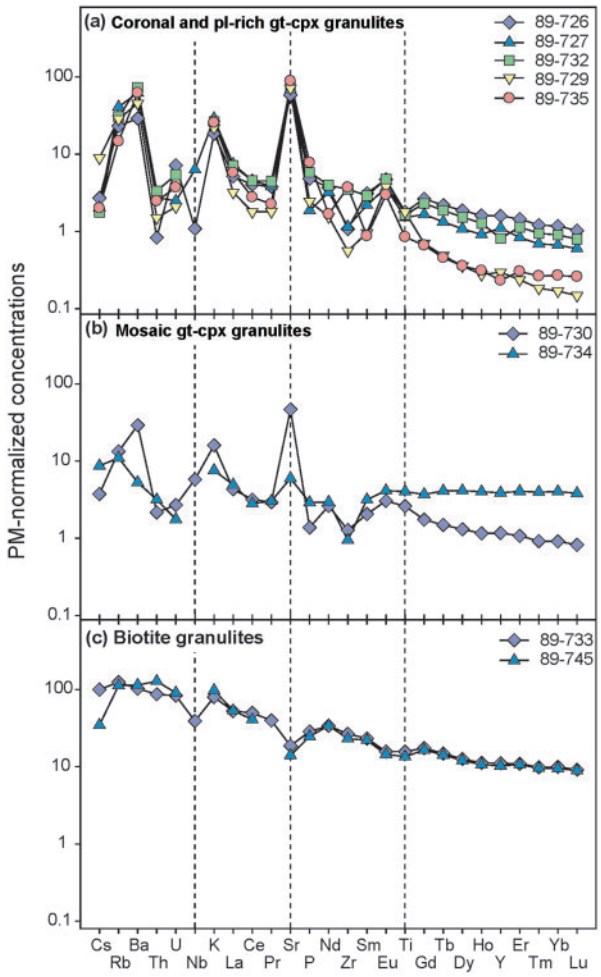


Fig. 11. Primitive mantle normalized trace element patterns for Lashaine granulite xenoliths. Primitive mantle values are from McDonough & Sun (1995).

the Labait two-pyroxene granulites, including enrichment of the LREE [$(La/Yb)_N = 8{\cdot}7–29{\cdot}3$], relative enrichment of Sr, relative depletion of Cs, Th, U, Nb and Ta, and high, variable La/Nb ratios (2·3–6·8) (Fig. 13). Ba concentrations are high, but are not extreme (356–1120 ppm).

Quartz-free granulites. Relative to the quartz-bearing granulites, the quartz-free granulites (NS04-61 and NS04-80) have lower SiO_2 (50·5–51·3 wt %), but comparable Mg-numbers (56–60). They also fall on the trends described above for the quartz-bearing granulites, plotting at the high TiO_2–Fe_2O_3–MgO–CaO, low Al_2O_3–Na_2O–K_2O end of the trends (Fig. 6). SiO_2/Al_2O_3 ratios (3·5–3·7) are similar to those in basaltic or andesitic melts (Kempton & Harmon, 1992) (Fig. 7). The quartz-free granulites have relatively high Ni (95–117 ppm) and Cr (252–307 ppm) contents, but low Ba contents (207–328 ppm). Concentrations of most other trace elements fall within the range defined by the quartz-bearing granulites. Trace element patterns for the quartz-free granulites are relatively flat [$(La/Yb)_N = 2{\cdot}7–3{\cdot}4$, Figs 12 and 13], but the samples are enriched in Sr. Relative depletions in Nb and Ti are very small. La/Nb ratios range from 1·3 to 1·5, similar to those in mid-ocean ridge or ocean-island basalts (Sun & McDonough, 1989).

Sr–Nd isotopes

Present-day whole-rock Sr isotopic compositions in most xenoliths are relatively unradiogenic ($\leq 0{\cdot}706$), with the exception of the two biotite–garnet granulites from Lashaine (89-733 and 89-745) and one quartz-bearing granulite from Naibor Soito, which range to higher values (0·711–0·721) (Table 5, Fig. 14a). $^{87}Rb/^{86}Sr$ ratios show a moderate spread (0·014–0·68), but do not correlate with variability in $^{87}Sr/^{86}Sr$.

Whole-rock Nd isotopic compositions are highly variable, but most samples have negative ε_{Nd} and fall on a

Downloaded from http://petrology.oxfordjournals.org/ at University of Dar es Salaam on March 8, 2016

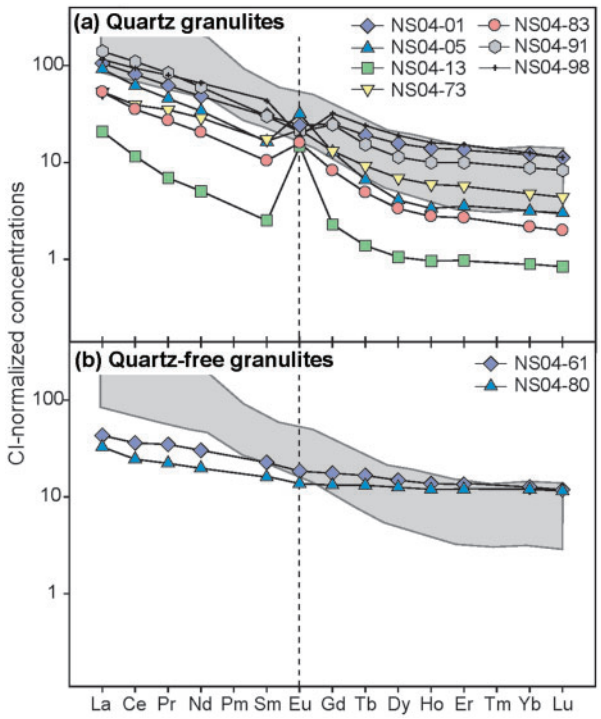


Fig. 12. Chondrite-normalized REE patterns of Naibor Soito granulite xenoliths. Gray field in the background shows range of data for high-Mg andesites from the Musoma–Mara Greenstone Belt (Manya *et al.*, 2007). Chondrite values from McDonough & Sun (1995).

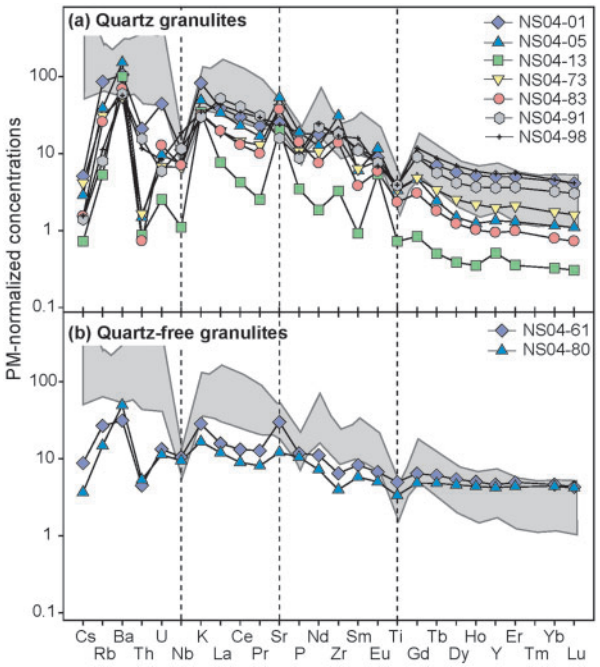


Fig. 13. Primitive mantle normalized trace element patterns for Naibor Soito granulite xenoliths compared with high-magnesium andesites from the Musoma–Mara Greenstone Belt (gray field; Manya *et al.*, 2007). Primitive mantle values are from McDonough & Sun (1995).

near-vertical array on a plot of $^{87}Sr/^{86}Sr$ vs $^{143}Nd/^{144}Nd$ (Fig. 14a). The Labait anorthosite, LB04-27, has a curiously high ε_{Nd} of +9, considering that it is LREE-enriched ($^{147}Sm/^{144}Nd = 0{\cdot}133$); below we discuss the possibility that the REE patterns of low REE abundance samples (this sample and the Lashaine garnet–clinopyroxene granulites) may be influenced by interaction with the host lava. There are no Sm–Nd isochrons within any of the suites, although samples from the Labait and Naibor Soito show strongly correlated trends on an isochron diagram (Fig. 14b), consistent with an Archean age. T_{DM} model ages for Labait and Naibor Soito samples are ancient (2·3–3·4 Ga, Table 5). In samples with >10 ppm Nd, which would be less susceptible to overprinting by the host basalt, the range in model ages is smaller (2·7–3·0 Ga). In contrast, Lashaine granulites show more scatter on the isochron diagram and a correspondingly broader range in T_{DM} (1·5–2·8 Ga), with the two biotite–garnet granulites having identical T_{DM} ages of 2·8 Ga.

Zircon geochronology

Zircon U–Pb ratios and associated ages for the Labait and Naibor Soito xenoliths are provided in Figs 15–16 and Supplementary Data Electronic Appendix Table I. All uncertainties shown in the data table, figures, and quoted in the text are 2σ. Cathodoluminesence (CL) images of analyzed zircons are provided in Supplementary Data Electronic Appendix J. Because the method used here does not allow concentrations to be calculated, Table I includes the average number of counts per second measured during ablation for masses 206 (Pb), 207 (Pb) and 238 (U). These data give a qualitative sense of the differences in concentrations between zircons.

All zircons dated here are Archean, and $^{207}Pb/^{206}Pb$ ratios therefore provide the best estimate of their ages. Where Pb/U ratios are reliable (i.e. when U concentrations are relatively high), concordant ages or concordia plots have been calculated using ISOPLOT/EX, v.3.00 (Ludwig, 2003). Concordant ages were calculated for all zircons that were discordant by <2%. In zircons with significant lead loss, $^{207}Pb/^{206}Pb$ ages skew to younger ages. These zircons are excluded without comment from the ranges of the ages presented below, but are included in Figs 15–16 and the data table (Supplementary Data Electronic Appendix Table I). Errors are typically of the order of 20–80 Ma (1–4%, 2σ).

No zircons from the Lashaine xenoliths were analyzed for this study. However, Blondes *et al.* (in preparation) determined Pan-African and highly discordant older Precambrian ages by LA-ICP-MS for minute zircons observed in thin sections of the two Lashaine biotite–garnet granulites (89-733 and 89-745).

Downloaded from http://petrology.oxfordjournals.org/ at University of Dar es Salaam on March 8, 2016

Table 5: Sr–Nd isotope data for selected Tanzanian granulite xenoliths

Sample	Type	$^{87}Sr/^{86}Sr$	$^{87}Rb/^{86}Sr$	$^{143}Nd/^{144}Nd$	$^{147}Sm/^{144}Nd$	Sr (ppm)	Rb (ppm)	Nd (ppm)	Sm (ppm)	ε_{Nd} 0 Ma	ε_{Nd} 2·66 Ga	T_{DM}(Ga)
Labait												
LB04-19	2px	0·703979 ± 10	0·10	0·511452 ± 7	0·133	735	*25·1*	26·6	5·6	−23·1	−1·7	2·9
LB04-36	2px	0·704797 ± 99	0·41	–	–	*521*	*74·8*	–	–	–	–	–
LB04-52	2px	0·703909 ± 14	0·067	0·511539 ± 7	0·135	569	*13·6*	30·3	6·5	−21·4	−0·8	2·9
LB04-07	2px-hbl	0·705147 ± 20	0·058	0·512222 ± 10	0·170	*524*	*10·8*	*11·3*	*3·0*	−8·1	+0·8	2·8
LB04-82	2px-hbl	0·704131 ± 15	0·048	0·511607 ± 8	0·139	969	*16·5*	44·2	9·8	−20·1	−0·7	2·9
LB04-39	Gt-opx	0·704834 ± 12	0·39	0·512081 ± 6	0·173	504	*69·4*	9·8	2·7	−10·9	−2·9	3·4
LB04-91	Gt-opx	0·703987 ± 12	0·092	0·511683 ± 6	0·143	847	*27·6*	14·1	3·2	−18·6	−0·8	2·9
LB04-27	anorth	0·703718 ± 13	0·074	0·513109 ± 25	0·133	436	*11·4*	3·5	0·74	+9·2	+31	–
Lashaine												
89-733	Bt-gt	0·716532 ± 16	0·57	0·511689 ± 7	0·140	*371*	*74·6*	*42·3*	*9·4*	−18·5	+0·3	2·8
89-745	Bt-gt	0·721067 ± 23	0·68	0·511761 ± 9	0·145	281	*67·4*	*37·3*	8·6	−17·1	+0·3	2·8
89-726	Gt-cpx	0·704055 ± 42	0·034	0·512288 ± 38	0·172	*1160*	*13·9*	*4·6*	*1·3*	−6·8	+1·4	2·7
89-727	Gt-cpx	0·704002 ± 20	0·051	–	–	*1365*	*24·5*	–	–	–	–	–
89-729	Gt-cpx	0·703665 ± 17	0·034	0·51170 ± 18	0·127	*1417*	*17·1*	*1·9*	*0·39*	−18·4	+5·2	2·4
89-730	Gt-cpx	0·703834 ± 12	0·024	0·512445 ± 72	0·158	*927*	*8*	*2·7*	*0·68*	−3·8	+9·3	1·7
89-734	Gt-cpx	0·702490 ± 12	0·16	–	–	*119*	*6·6*	–	–	–	–	–
89-735	Gt-cpx	0·704200 ± 18	0·014	–	–	*1760*	*8·8*	–	–	–	–	–
BD-727	Gt-cpx	0·70414 ± 5	0·032	0·51210 ± 2	0·161	1226	13·7	3·72	0·9875	−10·5	+1·5	2·7
BD-528	Gt-cpx	0·70415 ± 5	0·033	0·51229 ± 3	0·142	1359	15·6	4·492	1·053	−6·8	+11·6	1·7
BD-798	Gt-cpx	0·70359 ± 4	0·044	0·51154 ± 3	0·110	1333	20·1	1·825	0·3305	−21·4	+7·6	2·2
BD-526	Gt-cpx	0·70429 ± 5	0·016	0·51216 ± 4	0·152	1441	7·9	3·943	0·9929	−9·3	+5·7	2·2
BD-728	Gt-cpx	0·70405 ± 3	0·061	0·51236 ± 4	0·141	1222	25·6	5·518	1·287	−5·4	+13·3	1·5
BD-786	Gt-cpx	0·70434 ± 4	0·093	0·51209 ± 2	0·147	1182	4·2	4·221	1·029	−10·7	+6	2·2
Naibor Soito												
NS04-01	Qtz	0·711056 ± 27	0·29	0·511311 ± 17	0·130	503	*51·3*	–	–	−25·9	−3·6	3·1
NS04-05	Qtz	0·702671 ± 12	0·073	0·510970 ± 9	0·097	896	*23·2*	12·8	2·0	−32·5	+0·7	2·7
NS04-13	Qtz	0·705456 ± 11	0·024	0·511328 ± 29	0·102	371	*3·2*	2·4	0·38	−25·6	+6·3	2·3
NS04-73	Qtz	–	–	0·511254 ± 20	0·122	–	–	–	–	−27·0	−2	2·9
NS04-83	Qtz	0·703268 ± 18	0·075	0·511078 ± 10	0·102	692	*18·5*	7·8	1·3	−30·4	+1·2	2·7
NS04-91	Qtz	0·705486 ± 13	0·044	0·511042 ± 8	0·104	308	*4·8*	24·3	4·0	−31·1	1·2	2·7
NS04-98	Qtz	–	–	0·511623 ± 6	0·133	–	–	–	–	−19·8	0	2·7
NS04-150	Qtz-free	0·703028 ± 17	0·062		–	1146	*25*	–	–	–	–	–
NS04-61	Qtz-free	0·703837 ± 20	0·075	0·511873 ± 8	0·156	603	*16·1*	12·2	3·0	−14·9	−1·2	3·0
NS04-80	Qtz-free	0·703231 ± 20	0·10	0·512273 ± 11	0·167	246	*8·9*	7·9	2·1	−7·1	2·9	2·5

All Lashaine samples with 'BD' prefix are from Cohen *et al.* (1984). Values in italics are concentration data from XRF (Sr and Rb) or ICP-MS (Nd and Sm). All other values were measured via isotope dilution. Errors on isotope ratios are 2 × standard error of the mean. T_{DM} calculated using the following values for DM: $^{147}Sm/^{144}Nd = 0·22$, $^{143}Nd/^{144}Nd = 0·51315$.

Downloaded from http://petrology.oxfordjournals.org/ at University of Dar es Salaam on March 8, 2016

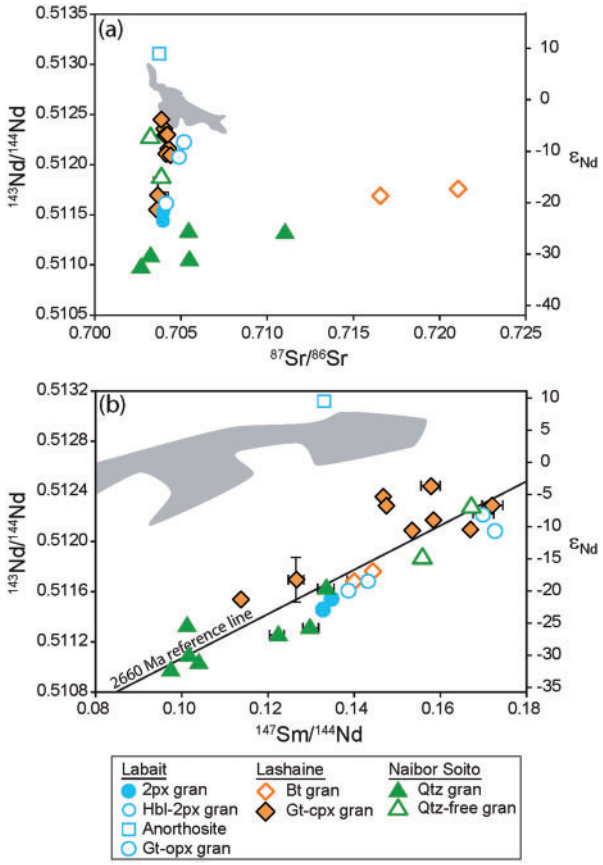


Fig. 14. (a) $^{87}Sr/^{86}Sr$ vs $^{143}Nd/^{144}Nd$ for Tanzanian granulite xenoliths, including data from Cohen *et al.* (1984). (b) Sm–Nd isochron plot for Tanzanian granulite xenoliths. Fields for East African Rift basalts (gray) after Aulbach *et al.* (2011).

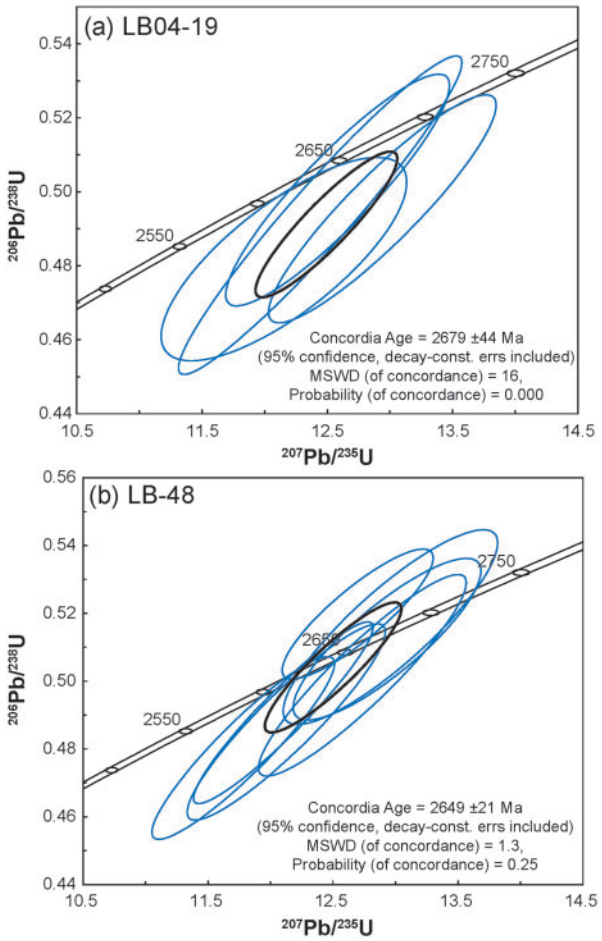


Fig. 15. Concordia plot for concordant zircons from Labait xenoliths: (a) LB04-19; (b) LB-48.

Labait

LB04-19 (two-pyroxene granulite). Zircons from this sample are transparent, multi-faceted, spherical or oblate, with aspect ratios near one and diameters typically <200 μm (see Supplementary Data Fig. J for CL images). Internal zoning is visible in approximately one-third of the zircons imaged by CL. The most common structure consists of a dark, polygonal core (~50 μm) surrounded by (a) ~20–40 μm wide bands of alternating light and dark gray or (b) featureless rims. A few zircons contain broad, oscillatory zones or sector zoning. Cores displaying these textures are typically surrounded by 10–40 μm thick, featureless rims.

Uranium concentrations in the zircons in LB04-19 are low relative to those in the Naibor Soito zircons. Few analyses produced sufficient counts of ^{238}U to calculate Pb/U ratios. Four concordant or near-concordant analyses give a pooled age of 2679 ± 44 Ma (Fig. 15a and Supplementary Data Electronic Appendix, Table I). Most $^{207}Pb/^{206}Pb$ ages for zircons with low U overlap with this (Supplementary Data Electronic Appendix Table I) and yield a weighted mean $^{207}Pb/^{206}Pb$ age of 2677 ± 25 Ma (excluding zircon 3.1, which is ~60 Myr older). A few zircons yield younger $^{207}Pb/^{206}Pb$ ages (<2600 Ma).

For comparison, U–Pb isotope dilution (ID)-TIMS analyses of single zircons from this sample yield a weighted mean $^{207}Pb/^{206}Pb$ age of 2644·1 ± 0·9 Ma (Blondes *et al.*, in preparation).

LB-48 (two-pyroxene granulite). Zircons from LB-48 are similar in morphology and size to those from LB04-19 (see Supplementary Data Fig. J). Most imaged zircons are featureless in CL or preserve only broad internal zoning; for example, cores of uniform texture surrounded by featureless rims. A small number of zircons contain cores (30–50 μm in diameter) that are relatively bright in CL and display oscillatory zoning, features typical of igneous zircons. Featureless rims on these crystals have very low U concentrations, resulting in large errors on rim analyses for crystals 42 and 49.

As in the previous sample, low U concentrations hampered the calculation of Pb/U ratios, and only seven

Downloaded from http://petrology.oxfordjournals.org/ at University of Dar es Salaam on March 8, 2016

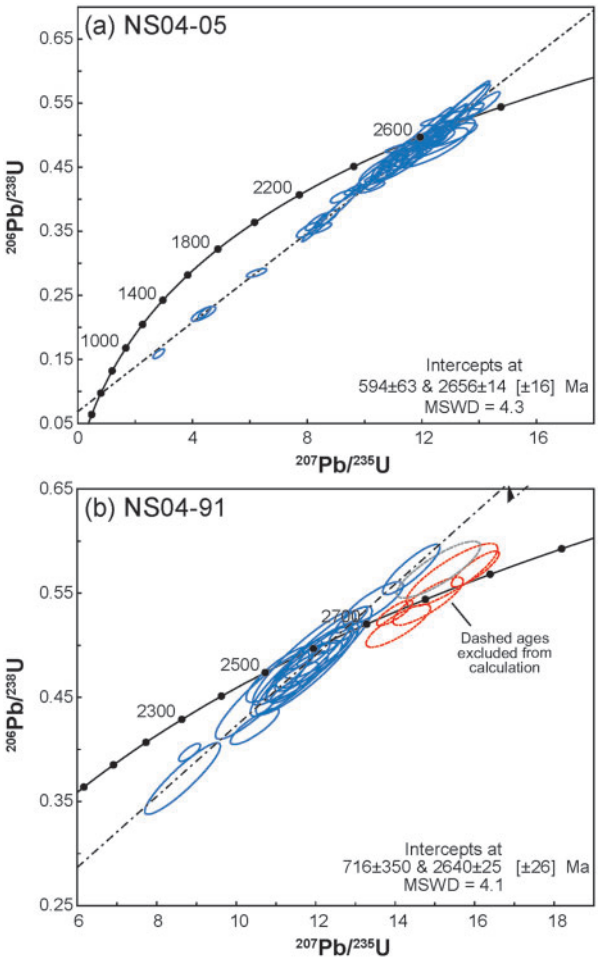


Fig. 16. Concordia plot for zircons from Naibor Soito xenoliths: (a) NS04-05; (b) NS04-91.

analyses provided sufficient counts to calculate these ratios, of which four were spots within the bright, zoned domains. This material yielded concordant $^{207}Pb/^{206}Pb$ ages for four crystals, ranging from 2646 to 2684 Ma, yielding a pooled $^{207}Pb/^{206}Pb$ age of 2649 ± 21 Ma (Fig. 15b). $^{207}Pb/^{206}Pb$ ages for other zircons, including domains consistent with either an igneous or metamorphic origin, generally overlap with this age, and yield a weighted mean $^{207}Pb/^{206}Pb$ age of 2653 ± 13 Ma.

Naibor Soito

NS04-05 (quartz-bearing granulite). In contrast to zircons from the Labait xenoliths, most zircons from this sample are prismatic with rounded terminations (see Supplementary Data Fig. J). Most crystals are 200–500 μm long and 100–200 μm wide, with aspect ratios between two and three. Despite morphologies consistent with an igneous origin, internal zoning visible in CL is rare and, where present, subtle. Distinct cores and rims are limited to a small number of crystals with dark polygonal or rod-shaped domains similar to those observed in LB04-19.

Zircons from Naibor Soito have high U concentrations relative to the Labait zircons, allowing Pb/U ratios to be calculated for most crystals. Many of these crystals are >2% discordant, but 13 concordant spots from this sample give ages ranging from 2528 to 2711 Ma. $^{207}Pb/^{206}Pb$ ages define a similar range (2504–2711 Ma), peaking around 2650 Ma. Among grains that display internal zoning in CL, ages from different domains are generally indistinguishable. Dark zones in crystals 17, 35 and 36, however, give discordant ages younger than the surrounding zircon.

A discordia including all analyses from this sample yields an upper intercept age of 2656 ± 14 Ma and a lower intercept age of 594 ± 63 Ma (Fig. 16a). The lower intercept age overlaps the timing of Pan-African metamorphism in Tanzania, although it is too imprecise to determine whether it represents the 540–565 Myr span of metamorphic ages seen in the Western Granulites or the 610–655 Myr span of metamorphic ages seen in the Eastern Granulites.

NS04-91 (quartz-bearing granulite). Most zircons from this sample are multi-faceted spheres, with diameters of 100–250 μm, but some are prismatic with similar dimensions to those from NS04-05 (see Supplementary Data Fig. J). Internal zoning within both morphologies is common, including both minor gradations similar to those in the previous sample and distinct core–rim relationships, and, unlike the previous sample, differences between core and rim $^{207}Pb/^{206}Pb$ ages are preserved in some cases.

The $^{207}Pb/^{206}Pb$ ages of zircons in NS04-91 cluster in two broad groups, one that ranges from 2750 to 2800 Ma, the other from 2550 to 2675 Ma (Fig. 16b, red and blue data, respectively). For concordant zircons, the ranges of ages are identical. The *c.* 2800 Ma spots are rare and occur almost exclusively in zircon cores, whereas the younger ages are not restricted to a given crystal domain or structure and are more prevalent. Three types of core–rim relationships corresponding to domains visible in CL are preserved: (1) *c.* 2800 Ma, bright, prismatic cores surrounded by 2620–2680 Ma rims (as in crystals 12, 19, 21 and 26; see Supplementary Data Fig. J); (2) a *c.* 2630 Ma core surrounded by a 2540–2570 Ma rim (crystal 3, Supplementary Data Fig. J); (3) a *c.* 2630 Ma core surrounded by a rim of identical age (crystal 29, Supplementary Data Fig. J). Crystals younger than *c.* 2800 Ma may be prismatic, oblate, or spherical. A U–Pb concordia plot for the *c.* 2650 Ma zircons gives an upper intercept age of 2640 ± 25 Ma and a very imprecise lower intercept age of 716 ± 350 Ma, similar to the concordia intercept ages in NS04-05 (Fig. 16). In comparison, U–Pb ID-TIMS ages for single zircons from this sample yield a weighted $^{207}Pb/^{206}Pb$ age of 2658 ± 1 Ma (Blondes *et al.*, in preparation).

Downloaded from http://petrology.oxfordjournals.org/ at University of Dar es Salaam on March 8, 2016

W3S-2 (quartz-bearing granulite). Zircons from this sample are mostly round to oblate, commonly unzoned, but sometimes contain dark, polygonal crystal cores (see Supplementary Data Fig. J). *In situ* ages are available for only two zircons from this sample. These zircons (11 and 13) give identical, concordant ages of 2636 ± 29 Ma and 2629 ± 22 Ma, respectively. These ages are within uncertainty of a $^{207}Pb/^{206}Pb$ weighted upper intercept age of 2643·2 ± 0·4 Ma measured for single zircons from this sample using ID-TIMS (Blondes *et al.*, in preparation).

DISCUSSION

Xenolith derivation depths and thermal conditions in the lower crust

Thermobarometry calculations and pseudosections for the Tanzanian lower crustal xenoliths, coupled with thermochronological studies (Bellucci *et al.*, 2011; Blondes *et al.*, in preparation), document the peak metamorphic conditions and cooling history of the deep crust beneath the Tanzanian Craton and Mozambique Belt. Exsolved ternary feldspars and zoned pyroxenes in the cratonic Labait two-pyroxene granulites reflect cooling from very high, probably igneous temperatures, to relatively low temperatures in the deep crust. Although pressures of equilibration are more difficult to estimate, some constraints are provided by compositional zoning in pyroxenes and accessory phase thermochronology. If it is assumed that the Labait two-pyroxene granulites cooled to a typical cratonic geotherm (e.g. 40 mW m^{-2} surface heat flow), then the lowest temperature recorded in pyroxene rims (480°C, Table 3) would correspond to a depth of ~45 km [using the 'preferred' geotherm of Hasterok & Chapman (2011)]. Moreover, Blondes *et al.* (in preparation) showed that rutile and apatite within these xenoliths contain no radiogenic Pb, despite having significant U contents. This means that the samples resided above the closure temperature for Pb diffusion in rutile and apatite at the time the samples were entrained in the host basalt. Using the typical grain dimensions, Blondes *et al.* (in preparation) calculated a closure temperature of ~430°C for Pb diffusion in apatite, which corresponds to a depth of ~39 km. Thus, the derivation depths of the two-pyroxene granulites, although not well defined via phase equilibria, may lie between 39 and 45 km; that is, within the present-day lowermost crust. Peak metamorphic conditions recorded by the Labait garnet–orthopyroxene granulites (e.g. LB04-91, 830–1050°C, 1·1–1·6 GPa, 33–48 km, Fig. 5a) and the anorthosite (LB04-27, 1050–1400°C, 1·1–1·8 GPa, 33–54 km, Fig. 5b) overlap with those of the two-pyroxene granulites, but range to somewhat higher pressures, suggesting their derivation from the lowermost crust or possibly the uppermost lithospheric mantle (e.g. if they formed by intrusion within the mantle lithosphere). The presence of exsolved ternary feldspar in the garnet–orthopyroxene granulite suggests cooling from high temperatures at minimum depths of ~43 km (see arrow in Fig. 5a), and the preservation of Archean Pb–Pb feldspar isochrons for this sample suggests that this portion of the lower crust or uppermost mantle cooled to below ~600°C and has remained cool since the Archean (Bellucci *et al.*, 2011). The only evidence for heating in the Labait granulites is found in the hornblende-bearing granulites, whose pyroxenes typically record higher temperatures on their rims (640–850°C) than in their cores (650–700°C, Table 3). This heating may reflect infiltration of the fluid that formed hornblende in these samples; however, the timing of this event is unknown.

In summary, the lower crust of the Tanzanian Craton experienced granulite-facies metamorphism followed by near-isobaric cooling in the Archean. It appears that, with the possible exception of the hornblende-bearing granulites, the East African Orogeny, as well as the East African Rift, had little thermal imprint on the lower crust of the craton.

In contrast to those of the Tanzanian craton, granulite-facies xenoliths in the Mozambique Belt record a very wide range in peak metamorphic conditions and distinctive cooling paths. The highest pressures are recorded in Lashaine garnet–clinopyroxene granulites, where the presence of kyanite requires minimum pressures of equilibration of ~1·6 GPa (greater than 48 km depth at temperatures of 800°C or above), and where the field of coexisting garnet–clinopyroxene–kyanite occurs at pressures of 1·7–2·25 GPa at temperatures less than 1000°C (51–68 km, Table 3, Fig. 5c). This is well below the present-day Moho, which lies at ~38 km (Tugume *et al.*, 2012). These high pressures, coupled with the coronal textures of garnet rimming clinopyroxene and plagioclase (Fig. 3), suggest that these samples entered the garnet and kyanite stability fields through burial during the East African Orogeny (see Supplementary Data Fig. O for possible P–T path). Such a counter-clockwise P–T path could be produced in the lower crust of the lower plate of a continent–continent collision (Ellis, 1987). The decompression path following peak metamorphism is not preserved, although Paleozoic ages recorded in titanite from these samples (Blondes *et al.*, in preparation) suggest slow cooling (~1°C Ma^{-1}) following Pan-African metamorphism, which is consistent with derivation of these samples from the lowermost crust of the orogen. Furthermore, the absence of radiogenic Pb in apatites from these samples suggests their derivation from the present-day lower crust, where the samples reside above the closure temperature for Pb diffusion in apatite (Blondes *et al.*, in preparation).

In contrast to the garnet–clinopyroxene granulites, both biotite–garnet granulites from Lashaine have equilibrated textures and experienced peak metamorphism at lower

Downloaded from http://petrology.oxfordjournals.org/ at University of Dar es Salaam on March 8, 2016

pressures (1·3–1·75 GPa, Fig. 5d), suggesting that these samples formed at considerably shallower depths (39–52 km) within the orogenically thickened crust. The presence of radiogenic Pb in apatites from these samples, yielding ages of ~470 Ma (Blondes *et al.*, in preparation), demonstrates that these samples resided below ~430°C prior to their entrainment in the host basalts. On the basis of these results, it appears that the biotite–garnet granulites derive from the present-day middle crust.

Granulites from Naibor Soito, within the Mozambique Belt, show peak metamorphic conditions consistent with their derivation from the lower crust of a thickened orogen (Fig. 5e and f: 1·0 GPa, 30 km to ~1·7 GPa, ~56 km). Secondary biotite in some samples suggests a possible counterclockwise cooling path (Fig. 5f). Although peak pressures in the Naibor Soito samples are not as high as those seen in the Lashaine garnet–clinopyroxene granulites, the Naibor Soito samples nevertheless appear to have equilibrated below the present-day Moho, suggesting that they too formed in an orogenically thickened crust. The absence of radiogenic Pb in apatite and rutile from these samples also indicates their derivation from the present-day lower crust (Blondes *et al.*, in preparation).

In summary, the lower crust of the Mozambique Belt experienced granulite-facies metamorphism in the deeper section of an orogenically thickened crust (from 30 to ~70 km depth) followed by uplift associated with crustal thinning. The Lashaine garnet–clinopyroxene granulites and Naibor Soito granulites were derived from the present-day lower crust, whereas the compositionally and mineralogically distinct Lashaine biotite–garnet granulites appear to be derived from the present-day middle crust.

Age of the lower crust in northern Tanzania

Two groups of Archean ages are documented in the granulite xenoliths. (1) Morphologically diverse zircons from the Labait and Naibor Soito granulites exhibit a narrow range of upper-intercept and concordant U–Pb ages from 2·64 to 2·68 Ga. (2) A few prismatic zircons from Naibor Soito give older ages (2·75–2·80 Ga). In addition, T_{DM} ages for whole-rock granulites from these localities span a similar age range to the older, prismatic zircons (2·7–3·0 Ga when limited to samples with >10 ppm Nd, Table 5). No zircons from the Lashaine xenoliths were analyzed, but these are also likely to have formed in the Archean. The biotite–garnet granulites give T_{DM} ages of 2·8 Ga, whereas T_{DM} ages for the garnet–clinopyroxene granulites range to much younger values (1·5–2·7 Ga, Table 5) as a result of contamination by the host basalt (see below).

The ages of the granulites are similar to those measured in meta-igneous rocks from the surface of the Mozambique Belt as well as the Tanzanian Craton. For example, the older U–Pb zircon ages of ~2·75 Ga in the granulites are also observed in strongly deformed gray orthogneiss and charnockites that crop out close to the craton boundary near Dodoma; however, these samples have a significant ~1·9 Ga overprint (Thomas *et al.*, 2013) that is not seen in the granulite xenoliths, nor surface samples from northern Tanzania (Tenczer *et al.*, 2014). Biotite-orthogneisses of the Western Granulites of northern Tanzania yield concordant U–Pb zircon dates of 2·70 ± 5 and 2·72 ± 5 Ga (Tenczer *et al.*, 2014). Similar ages are observed on the craton: zircon from a rhyolite from the Musoma–Mara greenstone belt gave a 2·754 ± 1 Ga U–Pb age, and whole-rock Sm–Nd isochrons for lavas are 2·74 ± 2 Ga (Mtoro *et al.*, 2009). Similarly, a whole-rock Sm–Nd isochron for lavas from the Iramba–Sekenke greenstone belt is 2·74 ± 3 Ga (Manya & Maboko, 2008*a*) (see Fig. 1 for locations of these greenstone belts).

The younger, 2·64–2·66 Ga U–Pb ages for the oblate to spherical, faceted zircons in both the Naibor Soito and Labait granulites overlap with concordant U–Pb zircon ages from a paragneiss (2·61 ± 2 Ga) and a meta-granodiorite (2·65 ± 4 Ga) in the Western Granulites of northern Tanzania (Tenczer *et al.*, 2014). They are also within uncertainty of U–Pb zircon ages for andesites and dacites from the Musoma–Mara Greenstone Belt of 2·67–2·68 Ga, upper intercept ages (2·65 ± 4 Ga) for post-orogenic granites from the same greenstone belt (Manya *et al.*, 2006), and $^{207}Pb/^{206}Pb$ zircon ages (2·62–2·66 Ga) for post-orogenic granites from the Geita greenstone belt (Sanislav *et al.*, 2014) These ~2·64 Ga ages are younger than the main phase of basaltic volcanism in the greenstone belts and may reflect granulite-facies metamorphism in the deep crust, given the morphologies of the zircons.

Post-Archean events are poorly recorded in the U–Pb systematics of zircons from the granulite xenoliths [see Blondes *et al.* (in preparation) for U–Pb thermochronological evidence for post-orogenic cooling of the lower crust of the Mozambique Belt following the East African Orogeny]. Some zircons from the Naibor Soito granulites are discordant, with imprecise Neoproterozoic lower intercepts (NS04-05, NS04-91, Fig. 16). Such discordancy suggests enhanced Pb diffusivity from radiation-damaged sites (e.g. Mezger & Krogstad, 1997), and the zircons may have experienced Pb loss during a Pan-African thermal event, despite the absence of any visible metamorphic rims (see Supplementary Data Fig. J). If so, this discordance implies that the Naibor Soito granulites cooled below the annealing temperature of zircon prior to granulite-facies metamorphism in the Pan-African, allowing radiation damage to accumulate following their original crystallization in the Archean.

In summary, the U–Pb zircon ages reported here for the Northern Tanzanian lower crust, both on- and off-craton, imply its formation in the Archean. Our data provide no strong evidence for later basaltic underplating or metamorphism of the lower crust underlying either the craton

Downloaded from http://petrology.oxfordjournals.org/ at University of Dar es Salaam on March 8, 2016

or metamorphic belt, suggesting that the lower crust was first metamorphosed to granulite-facies conditions shortly after its formation in the Archean. Later, high-grade metamorphism during the East African Orogeny is best documented in a companion study on thermochronology (Blondes *et al.*, in preparation).

Influence of alteration and host-rock infiltration on whole-rock trace element composition

Addition of incompatible trace elements along grain boundaries in lower crustal xenoliths may obscure their primary compositions (e.g. Condie *et al.*, 2004). Host lava infiltration and open-system grain-boundary alteration are likely to have the greatest influence on the whole-rock compositions of samples that have intrinsically low primary concentrations of incompatible elements. Such infiltration will have little impact on major element compositions.

Within the suites investigated here, samples with intrinsically low incompatible trace element abundances occur primarily at Lashaine (the garnet–clinopyroxene granulites), but also include the anorthosite from Labait (LB04-27, Fig. 2i and j). The incompatible elements in these samples, except for Rb, K, Ba and Sr, are present in concentrations less than 10 times the primitive mantle abundances (Figs 9 and 11). *In situ* analyses of the Labait anorthosite demonstrate that incompatible element concentrations in the grain boundary alteration are two to four orders of magnitude higher than those in the plagioclase (Fig. 17), suggesting that the whole-rock REE pattern and Sm–Nd isotope composition of this sample have been compromised.

Although *in situ* trace-element analyses have not been performed on minerals in the Lashaine garnet–clinopyroxene granulites, their whole-rock compositions are also likely to have been influenced by alteration. This may explain their scatter on the Sm–Nd isochron plot (Fig. 14b) and the scatter of their T_{DM} ages compared with those of the biotite–garnet granulites (which have very high incompatible element concentrations) and samples from other locations. A bulk mixing calculation suggests that the spread in the Sm–Nd data can be produced by 2–5% host basalt addition to relatively Nd-poor lower crust sampled by these xenoliths (Fig. 18).

A more dramatic example of selective enrichment is the extreme Ba concentrations found in the two-pyroxene granulites from Labait (530–6700 pm, with most samples containing >1000 ppm, Table 4). Such high Ba concentrations are rare in both basaltic rocks and granulite xenoliths. The phase chemistry and modal compositions of these samples suggest that the high Ba is unlikely to be a primary feature of the xenoliths, as a rock made up of 60% ternary feldspar, 10% of which is alkali feldspar containing 1·5% BaO (Supplementary Data Electronic Appendix Table B), can accommodate only ~800 ppm Ba in its primary minerals. This is significantly lower than most of the measured whole-rock concentrations, suggesting that Ba must be hosted along grain boundaries and is therefore a relatively recent addition to the samples. Because the Labait melilitite is Ba-poor (<200 ppm Ba, Dawson, 1999) relative to the xenoliths, contamination by the host magma is not responsible for the high Ba concentrations in the xenoliths. Given the presence of Ba-rich glass (up to 16 wt % BaO) and secondary minerals (e.g. zeolites) within melt pockets in some Labait peridotitic xenoliths (Dawson, 1999), which formed from rift-related magmas or fluids, we speculate that the high Ba in the granulite-facies xenoliths has a similar origin.

Formation of the lower crust

The Tanzanian granulite xenoliths formed from igneous protoliths: crystallized melts, cumulates, or residues, which recrystallized at high pressure and temperature to form the observed mineral assemblages within a few tens of million years of intrusion. In this section we use the whole-rock compositions of the samples to infer their petrogenesis.

Labait

The major element compositions, LREE-enriched trace element patterns, high Ni contents and moderate SiO_2/Al_2O_3 ratios of the two-pyroxene granulites suggest that their protoliths were Archean basaltic to andesitic melts (Table 4, Figs 6–9). Moreover, their relatively evolved compositions (up to 57 wt % SiO_2), high La/Nb ratios (1·3–7·1), and negative Nb and Ti anomalies (Fig. 9) are probably primary features of the rocks (as La, Nb and Ti are generally shown to be immobile during regional metamorphism), suggesting their formation in a convergent margin setting. A similar setting has been proposed for some greenstone belt basalts and high-Mg andesites from the Tanzanian Craton (Manya, 2004; Manya *et al.*, 2007; Manya & Maboko, 2008*a*, 2008*b*; Mtoro *et al.*, 2009), and the Labait samples may represent the lower crustal equivalent of these lavas, given their generally similar major element compositions (Figs 6 and 7). However, the Labait granulite compositions are distinct from the greenstone belt lavas in having somewhat lower CaO and higher K_2O concentrations (Figs 6 and 7). High Ni concentrations suggest that assimilation of pre-existing crust was minor, although negative initial ε_{Nd} values in most samples (Table 5) suggest that some assimilation occurred. Striking depletions in Cs, Rb, Th and U (Fig. 9) may have been produced by removal of a small-volume melt during high-grade metamorphism, as there is no evidence for a cumulate origin of these rocks, such as a positive Eu anomaly (Fig. 8), and such low concentrations (e.g. <0·1 ppm Cs, Th and U) are not seen in any common

Downloaded from http://petrology.oxfordjournals.org/ at University of Dar es Salaam on March 8, 2016

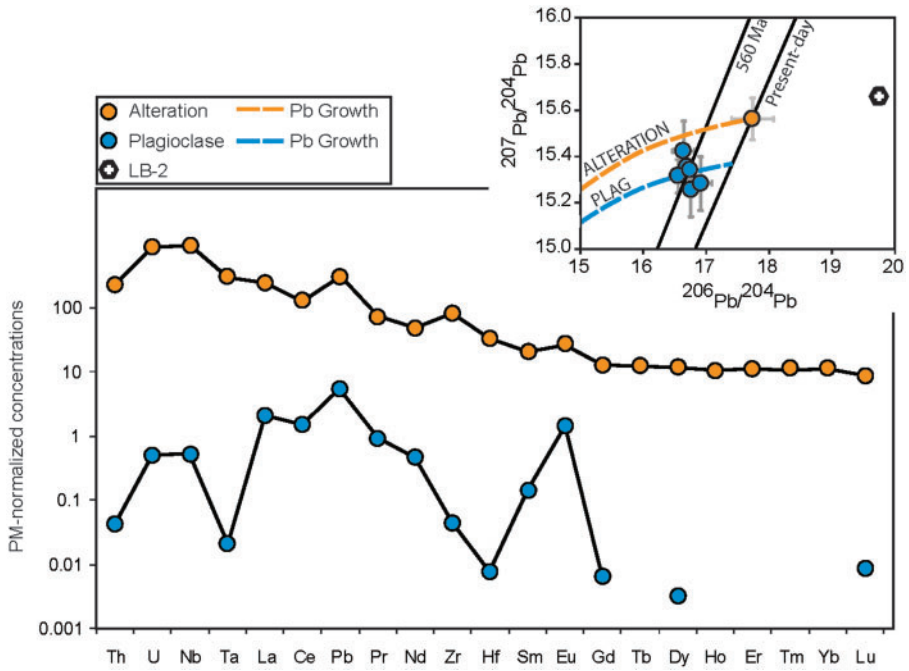


Fig. 17. *In situ* trace element analyses of plagioclase and grain boundary 'alteration' in the Labait anorthosite LB04-27. Phases analysed by LA-ICP-MS by J. Bellucci using a New Wave UP-213 Nd-YAG laser on an Element 2 ICP-MS system and ^{43}Ca as the internal standard [see Bellucci (2011) for additional information on methods]. Inset shows the Pb isotope data for plagioclase (Bellucci *et al.*, 2011), grain boundary alteration and the host basalt, LB-2. Both present-day and 560 Ma geochrons are shown for reference. Dashed curves represent single-stage growth curves with μ of 7·85 and 8·15 for the plagioclase and alteration, respectively.

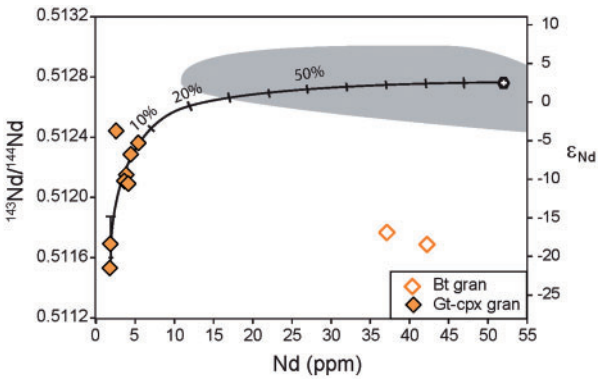


Fig. 18. Simple mixing between the least radiogenic Lashaine garnet–clinopyroxene granulite and the host basalt. Also shown are biotite–garnet granulites (open diamonds at high Nd and low $^{143}Nd/^{144}Nd$). Lashaine isotope data are from this study and Cohen *et al.* (1984), and the field of rift basalts (grey shading) is based on the compilation by Aulbach *et al.* (2011). End-member model compositions: crustal $^{143}Nd/^{144}Nd = 0{\cdot}51150$; crustal Nd concentration = 2 ppm; magma $^{143}Nd/^{144}Nd = 0{\cdot}51276$; magma Nd concentration = 52 ppm.

LREE-enriched lavas. Unradiogenic $^{87}Sr/^{86}Sr$ in these samples implies that this depletion occurred shortly after their formation in the Archean, perhaps during the 2·6 Ga metamorphic event described above.

The major and trace element compositions of the garnet–orthopyroxene and hornblende-bearing xenoliths share several key features with the two-pyroxene granulites, including superchondritic La/Nb ratios, basalt-like SiO_2/Al_2O_3 ratios, Ti depletions, and low Cs, Rb, Th and U concentrations (Table 4, Fig. 9). Positive Eu anomalies in the garnet–orthopyroxene granulites suggest some degree of plagioclase accumulation in these samples, whereas high Al_2O_3 contents, low Th/U and flat but elevated HREE patterns imply possible metamorphic concentration of garnet (Rudnick & Taylor, 1987). Variable trace element patterns in the hornblende-bearing xenoliths are more difficult to interpret beyond the first-order similarities noted above. The LREE-enriched pattern in LB04-82 is broadly similar to those in the two-pyroxene granulites, whereas the flat REE pattern and high Th/U ratio for LB04-07 may reflect preferential sampling of hornblende.

The anorthosite, LB04-27, is unique among the samples investigated here. It probably formed as an anorthite-rich cumulate, as indicated by its abundant calcic plagioclase, extremely high CaO and Al_2O_3, and positive Eu and Sr anomalies (Figs 6–9). It is unlikely to be a residue with this unusual composition. The high concentrations of incompatible trace elements in the widespread grain-boundary alteration seen in this sample (Fig. 17), coupled with its intrinsically low LREE concentrations, suggest that its REE pattern and $^{143}Nd/^{144}Nd$ may not be representative

Downloaded from http://petrology.oxfordjournals.org/ at University of Dar es Salaam on March 8, 2016

of the pre-eruptive composition. Nevertheless, the very high present-day ε_{Nd} (+9·2) is much higher than that of any modern-day rift basalts (Fig. 14b), suggesting that, if it experienced LREE addition during transport, its original ε_{Nd} must have been even higher. Conversely, considering that garnet also occurs in this sample (orthopyroxene, corundum, spinel and magnetite are the only other phases; Table 1), the original REE pattern may have been flatter in the LREE, or may even have been slightly LREE-depleted, which means that the initial ε_{Nd} may have been lower than +9·2 (i.e. the sample may have evolved with a high Sm/Nd following its formation and prior to its entrainment in the host lava). An important clue regarding the origin of this sample is the Pb isotope composition of its plagioclase, which is markedly more radiogenic than any other plagioclase analysed from the Labait granuilte xenoliths (Bellucci *et al.*, 2011). The Pb isotopic composition of this plagioclase plots close to the 550 Ma geochron (Fig. 17), suggesting that it may be a rare example of Pan-African magmatism.

Lashaine

The protoliths of the garnet–clinopyroxene granulites probably originated as plagioclase-rich cumulates in the lower crust, as suggested by Jones *et al.* (1983*b*). Features of the sample chemistry consistent with a cumulate origin include the following: (1) high Na_2O and Al_2O_3 contents that correlate with the relative proportions of plagioclase and clinopyroxene in each sample; such Na_2O and Al_2O_3 contents are similar to those seen in Proterozoic massif anorthosites and leucogabbros (Ashwal, 1993); (2) low SiO_2/Al_2O_3 ratios, which can result from plagioclase accumulation (Kempton & Harmon, 1992) (Fig. 7); (3) ubiquitous positive anomalies for Sr and Eu (Figs 10–11), both of which are compatible in plagioclase. The small amount of melt infiltration argued for above should have had only a minor effect on these aspects of the sample chemistry. A cumulate (as opposed to a restitic) origin is likely because of (1) the narrow range in whole-rock concentrations of SiO_2 and most incompatible trace elements, (2) variable HREE contents that correlate with the modal pyroxene:plagioclase ratio (samples with lower HREE such as 89-729 and 89-735 have a lower ratio), and (3) variable whole-rock concentrations of compatible elements (e.g. Sr and Eu in plagioclase, Ni in clinopyroxene), which correspond to the proportion of these phases in each sample (e.g. Rogers & Hawkesworth, 1982; Rudnick *et al.*, 1986; Dessai *et al.*, 2004). Certain features of the Lashaine xenoliths, including low concentrations of most incompatible elements and relative depletions in Cs, Rb, Th, U and Nb, are therefore likely to be primary features of cumulates and are not due to metamorphic processes.

The biotite–garnet granulites are compositionally distinct from any other granulites at Lashaine or elsewhere. They have melt-like SiO_2/Al_2O_3 ratios (Fig. 7), plot within the field of alkali basalts on Harker variation diagrams (Supplementary Data Fig. N), and have high concentrations of most incompatible trace elements and smooth trace element patterns, consistent with an origin as a crystallized melt. Indeed, their major and trace element compositions are similar to those of some potassic intraplate basalts (Figs 10 and 11) and their high Ti/V (~75) is consistent with an intraplate origin (Shervais, 1982). Ancient intrusion of intraplate magmas into the Tanzanian lithosphere was suggested by Paslick *et al.* (1995), who argued that the high time-integrated U/Pb ratios seen in the Pb isotopic composition of the modern rift basalts in Tanzania derive from lithospheric mantle that was intruded by ocean-island basalt (OIB)-like magmas >2 Ga ago. The compositions of the biotite–garnet granulites from Lashaine suggest that such magmas indeed may have intruded during the Archean.

Naibor Soito

The major element compositions of the Naibor Soito granulites overlap the field of greenstone belt lavas from the Tanzanian Craton (Fig. 6), suggesting that these granulites could be the high-pressure equivalents of the lavas, with protoliths ranging in composition from basalt to dacite. Trace-element patterns (Figs 12 and 13), with the exception of Cs, Rb, Th and U, which are notably depleted in the granulites, are also similar to those of greenstone belt lavas from the craton, which have been interpreted to have formed in a convergent margin setting (Manya, 2004; Manya *et al.*, 2007; Manya & Maboko, 2008*a*, 2008*b*; Mtoro *et al.*, 2009). In addition, the most SiO_2-rich sample, NS04-13, with 65 wt % SiO_2, has low REE contents and marked positive Eu and Sr anomalies, which suggest that this sample experienced plagioclase enrichment, either from igneous crystal accumulation or metamorphic differentiation. Although this is a composite xenolith with two distinct bands (Table 1, Fig. K), and both bands were included in the pulverized sample, the feldspar-rich band is volumetrically dominant, which may be the reason for the unusual compositional features of this sample.

Implications for the tectonic evolution of Tanzania

The protoliths of granulite xenoliths from all three localities formed as igneous rocks during the Archean. Although not precisely dated in this study, it appears that granulite-facies metamorphism, which caused depletion of Cs, Rb, Th and U, closely followed original intrusion in the Archean, leading to unradiogenic strontium, neodymium and lead (Pb in Labait feldspars has $^{206}Pb/^{204}Pb$ down to 13·5 and $^{207}Pb/^{204}Pb$ down to 14·6; Bellucci *et al.*, 2011) isotopic compositions in the present-day lower crust. At least one more phase of granulite-facies metamorphism probably occurred within the deep crust of the Mozambique Belt during the East African Orogeny,

Downloaded from http://petrology.oxfordjournals.org/ at University of Dar es Salaam on March 8, 2016

based on the high equilibration pressures of the Lashaine and Naibor Soito granulites (consistent with equilibration within the deeper portions of orogenically thickened continental crust) and the Phanerozoic ages of accessory phases dated by Blondes *et al.* (in preparation). In contrast, the lower crust of the Tanzanian Craton, as sampled by the Labait xenoliths, did not experience significant metamorphic resetting during the East African Orogeny (Bellucci *et al.*, 2011).

One sample, the Labait anorthosite LB04-27, appears to be post-Archean. Although its age has not been determined directly, its Pb isotopic composition is consistent with the protolith of this sample having intruded during the East African Orogeny (Fig. 17). If so, its intrusion did not lead to significant heating of the cratonic lower crust, as Archean Pb–Pb isochrons in alkali feldspars require temperatures that have remained lower than 600°C since the Archean (Bellucci *et al.*, 2011). With the exception of this sample, we see no evidence for juvenile additions to the lower crust since *c.* 2660 Ma. This is unusual, given the history of deformation and high-grade Pan-African metamorphism recorded in rocks currently in the upper crust of the Mozambique Belt (750–800°C, 1·2–1·3 GPa; Sommer *et al.*, 2003). Lower crustal granulites commonly record basaltic underplating preceding or coeval with high-grade metamorphism, with notable examples including granulites from the Kohistan Arc (Garrido *et al.*, 2006), northern Queensland (Rudnick *et al.*, 1986) and the North China Craton (Liu *et al.*, 2004). These syn-metamorphic lower crustal intrusions point to the important role that igneous heating plays in regional metamorphism.

If igneous intrusions did not provide heat for metamorphism in the Western Granulites of the East African Orogen, what did? Two potential sources of orogenic heat are (1) radioactive decay of heat-producing elements K, Th and U; during orogeny, radioactive heating is significant because of double-thickening of K-, Th- and U-rich crust and insulation by the mantle (England & Thompson, 1984; McLaren *et al.*, 2006); (2) incorporation of thin, hot, back-arc crust into the orogen (e.g. Currie & Hyndman, 2006; Johnson & Strachan, 2006; Hyndman & Currie, 2011).

Radioactive heating, an important heat source in long-lived orogens, seems unlikely to have been important during the East African Orogeny because of the low concentrations of heat-producing elements in the crust, as exhibited by our samples and implied by low surface heat flow in the craton and adjacent Mozambique Belt (Nyblade *et al.*, 1990). Incorporation of back-arc crust is likewise improbable based on the pre-collision reconstruction of Tanzania during the Neoproterozoic (Fritz *et al.*, 2005). In this reconstruction, which is based on detailed petrology, zircon U–Pb ages and T_{DM} ages, oceanic crust was subducted under the arc that eventually collided with Tanzania during the East African Orogeny. Arc volcanism and back-arc basin formation (represented in the Eastern Granulites exposed in eastern Tanzania) are localized solely in this terrane. The source of metamorphic heat in the Western granulites is therefore enigmatic.

CONCLUSIONS

Granulite xenoliths exhumed by Quaternary rift basalts in northern Tanzania from both the Tanzanian Craton and adjacent Mozambique Belt formed by basaltic intrusion into the lower crust during the Archean, most probably in a convergent margin setting. Intrusion was followed shortly thereafter by granulite-facies metamorphism, which led to extreme depletion in some trace elements (most notably Cs, Rb, Th and U). Some granulites (e.g. Naibor Soito, Labait two-pyroxene granulites) have whole-rock compositions remarkably similar to those of greenstone belt lavas from the Tanzanian Craton, whereas others (e.g. Lashaine, Labait anorthosite) have compositions of plagioclase-bearing cumulates for which greenstone belt equivalents are not recognized. Whereas the lower crust of the craton has been little affected by the East African Orogeny, that of the Mozambique Belt was buried to great depths in an orogenically thickened crust and later uplifted to its present position at the base of normal thickness crust (~30–40 km depth). Two incompatible element enriched biotite-bearing granulites from Lashaine derive from shallower depths than the rest of the samples and may have formed from a potassic intraplate basalt protolith in the Archean. A unique anorthosite from Labait may have formed as a cumulate during the East African Orogeny. If so, it constitutes the only evidence for juvenile crustal additions during the East African Orogeny seen within the xenolith suites.

ACKNOWLEDGEMENTS

The Tanzanian Commission of Science and Technology supplied the necessary research permits for the fieldwork. Dusty Aeiker assisted with fieldwork and with cataloging of the specimens. Phil Piccoli is thanked for help with the electron microprobe analyses; Rebecca Sproule performed the electron microprobe analyses at ANU, with help from Nick Ware. Mario Luong and Richard Ash assisted with the LA-ICP-MS U–Pb zircon dating. Sonja Aulbach and S. Saito helped with Nd isotope analyses, and Jay Kaufman and Igor Puchtel with Sr isotope analyses. Jeremy Bellucci is thanked for supplying the *in situ* analyses of Labait sample LB04-27 shown in Fig. 18. Tess Van Orden and Will Junkin carried out point counting and Will also assisted with drafting. Nelson Boniface and Chris Yakymchuk provided useful guidance in creating and interpreting psuedosections. Discussions with Madalyn Blondes, Jeremy Bellucci, Bill McDonough and Chris Yakymchuk helped to strengthen the arguments

Downloaded from http://petrology.oxfordjournals.org/ at University of Dar es Salaam on March 8, 2016

presented here. Dorrit Jacob, Pamela Kempton, Jörg Hermann and an anonymous reviewer provided many detailed and useful comments on an earlier version of this paper that helped us to improve the presentation and content. This work constitutes the MS thesis work of the first author.

FUNDING

This work was supported by the National Science Foundation (grant number EAR 0337255), the National Geographic Society (grant number 7836-05), and a Fulbright Award to R.L.R.

SUPPLEMENTARY DATA

Supplementary data for this paper are available at *Journal of Petrology* online.

REFERENCES

Ashwal, L. D. (1993). *Anorthosites*. Berlin: Springer.

Aulbach, S., Rudnick, R. L. & McDonough, W. F. (2008). Li–Sr–Nd isotope signatures of the plume and cratonic lithospheric mantle beneath the margin of the rifted Tanzanian craton (Labait). *Contributions to Mineralogy and Petrology* **155**, 79–92.

Aulbach, S., Rudnick, R. L. & McDonough, W. F. (2011). Evolution of the lithospheric mantle beneath the East African Rift in Tanzania and its potential signatures in rift magmas. In: Beccaluva, L., Bianchini, G. & Wilson, M. (eds) *Volcanism and Evolution of the African Lithosphere. Geological Society of America, Special Papers* **478**, 105–125.

Bellucci, J. J. (2011). The micron scale Pb isotopic systematics of the lower continental crust. PhD Dissertation, University of Maryland, College Park, 196 p, http://drum.lib.umd.edu/handle/1903/11688.

Bellucci, J. J., McDonough, W. F. & Rudnick, R. L. (2011). Thermal history and origin of the Tanzanian Craton from Pb isotope thermochronology of feldspars from lower crustal xenoliths. *Earth and Planetary Science Letters* **301**, 493–501.

Black, L. P., Kamo, S. L., Allen, C. M., Aleinikoff, J. N., Davis, D. W., Korsch, R. J. & Foudoulis, C. (2003). TEMORA 1: a new zircon standard for Phanerozoic U–Pb geochronology. *Chemical Geology* **200**, 155–170.

Blackburn, T. J., Bowring, S. A., Perron, J. T., Mahan, K. H., Dudas, F. O. & Barnhart, K. R. (2012). An exhumation history of continents over billion-year time scales. *Science* **335**, 73–76.

Bolhar, R., Kamber, B. S. & Collerson, K. D. (2007). U–Th–Pb fractionation in Archaean lower continental crust: Implications for terrestrial Pb isotope systematics. *Earth and Planetary Science Letters* **254**, 127–145.

Borg, G. & Krogh, T. (1999). Isotopic age data of single zircons from the Archaean Sukumaland Greenstone Belt, Tanzania. *Journal of African Earth Sciences* **29**, 301–312.

Brazier, R. A., Nyblade, A. A., Langston, C. A. & Owens, T. J. (2000). P_n wave velocities beneath the Tanzania Craton and adjacent rifted mobile belts, East Africa. *Geophysical Research Letters* **27**, 2365–2368.

Brey, G. P. & Köhler, T. (1990). Geothermobarometry in four-phase lherzolites II. New thermobarometers, and practical assessment of existing thermobarometers. *Journal of Petrology* **31**, 1353–1378.

Burton, K. W., Schiano, P., Birck, J.-L., Allègre, C. J., Rehkämper, M., Halliday, A. N. & Dawson, J. B. (2000). The distribution and behaviour of rhenium and osmium amongst mantle minerals and the age of the lithospheric mantle beneath Tanzania. *Earth and Planetary Science Letters* **183**, 93–106.

Chang, Z. S., Vervoort, J. D., McClelland, W. C. & Knaack, C. (2006). U–Pb dating of zircon by LA-ICP-MS. *Geochemistry, Geophysics, Geosystems* **7**, 14.

Chen, S., O'Reilly, S. Y., Zhou, X., Griffin, W. L., Zhang, G., Sun, M., Feng, J. & Zhang, M. (2001). Thermal and petrological structure of the lithosphere beneath Hannuoba, Sino-Korean Craton, China: evidence from xenoliths. *Lithos* **56**, 267–301.

Chesley, J. T., Rudnick, R. L. & Lee, C.-T. (1999). Re–Os systematics of mantle xenoliths from the East African Rift: Age, structure, and history of the Tanzanian craton. *Geochimica et Cosmochimica Acta* **63**, 1203–1217.

Christensen, N. I. & Mooney, W. D. (1995). Seismic velocity structure and composition of the continental crust: a global view. *Journal of Geophysical Research* **100**, 9761–9788.

Cohen, R. S., O'Nions, R. K. & Dawson, J. B. (1984). Isotope geochemistry of xenoliths from East Africa: implications for development of mantle reservoirs and their interaction. *Earth and Planetary Science Letters* **68**, 209–220.

Condie, K. C., Cox, J., O'Reilly, S. Y., Griffin, W. L. & Kerrich, R. (2004). Distribution of high field strength and rare earth elements in mantle and lower crustal xenoliths from the southwestern United States: The role of grain-boundary phases. *Geochimica et Cosmochimica Acta* **68**, 3919–3942.

Currie, C. A. & Hyndman, R. D. (2006). The thermal structure of subduction zone back arcs. *Journal of Geophysical Research—Solid Earth* **111**, doi: 10.1029/2005JB004024.

Cutten, H., Johnson, S. P. & DeWaele, B. (2006). Protolith ages and timing of metasomatism related to the formation of whiteschists at Mautia Hill, Tanzania: Implications for the assembly of Gondwana. *Journal of Geology* **114**, 683–698.

Dawson, J. B. (1977). Sub-cratonic crust and upper-mantle models based on xenolith suites in kimberlite and nephelinitic diatremes. *Journal of the Geological Society, London* **134**, 173–184.

Dawson, J. B. (1992). Neogene tectonics and volcanicity in the North Tanzania sector of the Gregory Rift Valley: contrasts with the Kenya sector. *Tectonophysics* **204**, 81–92.

Dawson, J. B. (1999). Metasomatism and melting in spinel peridotite xenoliths from Labait, Tanzania. In: Gurney, J. J., Gurney, J. L., Pascoe, M. D. & Richardson, S. H. (eds) *The J. B. Dawson Volume. Proceedings of the VIIth International Kimberlite Conference*. Red Roof Design, pp. 164–173.

Dawson, J. B. (2002). Metasomatism and partial melting in upper-mantle peridotite xenoliths from the Lashaine volcano, northern Tanzania. *Journal of Petrology* **43**, 1749–1777.

Dawson, J. B. & Smith, J. V. (1973). Alkalic pyroxenite xenoliths from the Lashaine volcano, northern Tanzania. *Journal of Petrology* **14**, 113–131.

Dawson, J. B. & Smith, J. V. (1988). Metasomatised and veined upper-mantle xenoliths from Pello Hill, Tanzania: evidence for anomalously-light mantle beneath the Tanzanian sector of the East African Rift Valley. *Contributions to Mineralogy and Petrology* **100**, 510–527.

Dawson, J. B., Powell, D. G. & Reid, A. M. (1970). Ultrabasic xenoliths and lava from the Lashaine volcano, northern Tanzania. *Journal of Petrology* **11**, 519–548.

Dawson, J. B., James, D., Paslick, C. & Halliday, A. M. (1997). Ultrabasic potassic low-volume magmatism and continental rifting in north–central Tanzania: association with enhanced heat flow.

Downloaded from http://petrology.oxfordjournals.org/ at University of Dar es Salaam on March 8, 2016

Proceedings of the Sixth International Kimberlite Conference. Russian Geology and Geophysics **38**, 69–81.

de Capitani, C. & Petrakakis, K. (2010). The computation of equilibrium assemblage diagrams with Theriak/Domino software. *American Mineralogist* **95**, 1006–1016.

Dessai, A. G. & Vaselli, O. (1999). Petrology and geochemistry of xenoliths in lamprophyres from the Deccan Traps: implications for the nature of the deep crust boundary in western India. *Mineralogical Magazine* **63**, 703–722.

Dessai, A. G., Markwick, A., Vaselli, O. & Downes, H. (2004). Granulite and pyroxenite xenoliths from the Deccan Trap: insight into the nature and composition of the lower lithosphere beneath cratonic India. *Lithos* **78**, 263–290.

Downes, H. (1993). The nature of the lower continental crust of Europe—petrological and geochemical evidence from xenoliths. *Physics of the Earth and Planetary Interiors* **79**, 195–218.

Droop, G. T. R. (1987). A general equation for estimating Fe^{3+} concentrations in ferromagnesian silicates and oxides from microprobe analyses, using stoichiometric criteria. *Mineralogical Magazine* **51**, 431–435.

Ellis, D. J. (1987). The origin and evolution of granulites in normal and thickened crusts. *Geology* **15**, 167–170.

England, P. C. & Thompson, A. B. (1984). Pressure–temperature–time paths of regional metamorphism I. *Heat transfer during the evolution of regions of thickened continental crust. Journal of Petrology* **25**, 894–928.

Fritz, H., Tenczer, V., Hauzenberger, C. A., Wallbrecher, E., Hoinkes, G., Muhongo, S. & Mogessie, A. (2005). Central Tanzanian tectonic map: A step forward to decipher Proterozoic structural events in the East African Orogen. *Tectonics* **24**, doi: 10.1029/2005TC001796.

Fritz, H., Tenczer, V., Hauzenberger, C., Wallbrecher, E. & Muhongo, S. (2009). Hot granulite nappes—tectonic styles and thermal evolution of the Proterozoic granulite belts in East Africa. *Tectonophysics* **477**, 160–173.

Fuhrman, M. L. & Lindsley, D. H. (1988). Ternary-feldspar modeling and thermometry. *American Mineralogist* **73**, 201–215.

Garrido, C. J., Bodinier, J. L., Burg, J. P., Zeilinger, G., Hussain, S. S., Dawood, H., Chaudhry, M. N. & Gervilla, F. (2006). Petrogenesis of mafic garnet granulite in the lower crust of the Kohistan paleo-arc complex (Northern Pakistan): Implications for intra-crustal differentiation of island arcs and generation of continental crust. *Journal of Petrology* **47**, 1873–1914.

Gibson, S. A., McMahon, S. C., Day, J. A. & Dawson, J. B. (2013). Highly refractory lithospheric mantle beneath the Tanzanian Craton: evidence from Lashaine pre-metasomatic garnet-bearing peridotites. *Journal of Petrology* **54**, 1503–1546.

Gilbert, M. C., Helz, R. T., Popp, R. K. & Spear, F. S. (1982). Experimental studies of amphibole stability. In: Veblen, D. R. & Ribbe, P. H. (eds) *Amphiboles: Petrology and Experimental Phase Relations. Mineralogical Society of America, Reviews in Mineralogy* **9B**, 229–353.

Green, N. L. & Usdansky, S. I. (1986). Ternary-feldspar mixing relations and thermobarometry. *American Mineralogist* **71**, 1100–1108.

Griffin, W. L., Zhang, A. D., O'Reilly, S. Y. & Ryan, C. G. (1998). Phanerozoic evolution of the lithosphere beneath the Sino-Korean Craton. In: Flower, M., Chung, S.-L., Lo, C.-H. & Lee, T.-Y. (eds) *Mantle Dynamics and Plate Interactions in East Asia*, Geodynamics series Volume 27. American Geophysical Union, pp. 107–126.

Guidotti, C. V. (1984). Micas in metamorphic rocks. In: Bailey, S. W. (ed.) *Micas. Mineralogical Society of America, Reviews in Mineralogy* **13**, 357–467.

Hasterok, D. & Chapman, D. S. (2011). Heat production and geotherms for the continental lithosphere. *Earth and Planetary Science Letters* **307**, 59–70.

Holland, T. J. B. & Powell, R. (1998). An internally constituent thermodynamic data set for phases of petrological interest. *Journal of Metamorphic Geology* **16**, 309–343.

Huang, X. L., Xu, Y. G. & Liu, D. Y. (2004). Geochronology, petrology and geochemistry of the granulite xenoliths from Nushan, east China: Implication for a heterogeneous lower crust beneath the Sino-Korean Craton. *Geochimica et Cosmochimica Acta* **68**, 127–149.

Huang, Y. M., van Calsteren, P. & Hawkesworth, C. J. (1995). The evolution of the lithosphere in Southern Africa—a perspective on the basic granulite xenoliths from kimberlites in South Africa. *Geochimica et Cosmochimica Acta* **59**, 4905–4920.

Hyndman, R. D. & Currie, C. A. (2011). Why is the North America Cordillera high? Hot backarcs, thermal isostasy, and mountain belts. *Geology* **39**, 783–786.

Johnson, M. R. W. & Strachan, R. A. (2006). A discussion of possible heat sources during nappe stacking: the origin of Barrovian metamorphism within the Caledonian thrust sheets of NW Scotland. *Journal of the Geological Society, London* **163**, 579–582.

Johnson, S. P., Cutten, H. N. C., Muhongo, S. & DeWaele, B. (2003). Neoarchaean magmatism and metamorphism of the western granulites in the central domain of the Mozambique belt, Tanzania: U–Pb SHRIMP geochronology and *PT* estimates. *Tectonophysics* **375**, 125–145.

Jones, A. P., Smith, J. V. & Dawson, J. B. (1983*a*). Glasses in mantle xenoliths from Olmani, Tanzania. *Journal of Geology* **91**, 167–178.

Jones, A. P., Smith, J. V., Dawson, J. B. & Hansen, E. C. (1983*b*). Metamorphism, partial melting, and K-metasomatism of garnet–scapolite–kyanite granulite xenoliths from Lashaine, Tanzania. *Journal of Geology* **91**, 143–166.

Julia, J., Ammon, C. J. & Nyblade, A. A. (2005). Evidence for mafic lower crust in Tanzania, East Africa, from joint inversion of receiver functions and Rayleigh wave dispersion velocities. *Geophysical Journal International* **162**, 555–569.

Kabete, J. M., McNaughton, N. J., Groves, D. I. & Mruma, A. H. (2012). Reconnaissance SHRIMP U–Pb zircon geochronology of the Tanzania Craton: Evidence for Neoarchean granitoid–greenstone belts in the Central Tanzania Region and the Southern East African Orogen. *Precambrian Research* **216**, 232–266.

Kempton, P. D. & Harmon, R. S. (1992). Oxygen-isotope evidence for large-scale hybridization of the lower crust during magmatic underplating. *Geochimica et Cosmochimica Acta* **56**, 971–986.

Kempton, P. D., Downes, H., Sharkov, E. V., Vetrin, V. R., Ionov, D. A., Carswell, D. A. & Beard, A. (1995). Petrology and geochemistry of xenoliths from the Northern Baltic shield: Evidence for partial melting and metasomatism in the lower crust beneath an Archaean terrane. *Lithos* **36**, 157–184.

Kempton, P. D., Downes, H., Neymark, L. A., Wartho, J. A., Zartman, R. E. & Sharkov, E. V. (2001). Garnet granulite xenoliths from the Northern Baltic Shield—the underplated lower crust of a Palaeoproterozoic large igneous province. *Journal of Petrology* **42**, 731–763.

Koornneef, J. M., Davies, G. R., Dopp, S. P., Vukmanovic, Z., Nikogosian, I. K. & Mason, P. R. D. (2009). Nature and timing of multiple metasomatic events in the sub-cratonic lithosphere beneath Labait, Tanzania. *Lithos* **112**, 896–912.

Koreshkova, M. Y., Downes, H., Nikitina, L. P., Vladykin, N. V., Larionov, A. N. & Sergeev, S. A. (2009). Trace element and age characteristics of zircons in granulite xenoliths from the

Downloaded from http://petrology.oxfordjournals.org/ at University of Dar es Salaam on March 8, 2016

Udachnaya kimberlite pipe, Siberia. *Precambrian Research* **168**, 197–212.

Kretz, R. (1983). Symbols for rock-forming minerals. *American Mineralogist* **68**, 277–279.

Krogh-Ravna, E. (2000). The garnet–clinopyroxene Fe^{2+}–Mg geothermometer: an updated calibration. *Journal of Metamorphic Geology* **18**, 211–219.

Last, R. J., Nyblade, A. A., Langston, C. A. & Owens, T. J. (1997). Crustal structure of the East African Plateau from receiver functions and Rayleigh wave phase velocities. *Journal of Geophysical Research—Solid Earth* **102**, 24469–24483.

Lee, C.-T. & Rudnick, R. L. (1999). Compositionally stratified cratonic lithosphere: petrology and geochemistry of peridotite xenoliths from the Labait volcano, Tanzania. In: Gurney, J. J., Gurney, J. L., Pascoe, M. D. & Richardson, S. R. (eds) *The P. H. Nixon Volume. Proceedings of the VIIth International Kimberlite Conference*. Red Roof Design, pp. 503–521.

Leeman, W. P., Menzies, M. A., Matty, D. J. & Embree, G. F. (1985). Strontium, neodymium and lead isotopic compositions of deep crustal xenoliths from the Snake River Plain: evidence for Archean basement. *Earth and Planetary Science Letters* **75**, 354–368.

Liu, Y. S., Gao, S., Jin, S. Y., Hu, S. H., Sun, M., Zhao, Z. B. & Feng, J. L. (2001). Geochemistry of lower crustal xenoliths from Neogene Hannuoba Basalt, North China Craton: Implications for petrogenesis and lower crustal composition. *Geochimica et Cosmochimica Acta* **65**, 2589–2604.

Liu, Y. S., Gao, S., Yuan, H. L., Zhou, L., Liu, X. M., Wang, X. C., Hu, Z. C. & Wang, L. S. (2004). U-Pb zircon ages and Nd, Sr, and Pb isotopes of lower crustal xenoliths from North China Craton: insights on evolution of lower continental crust. *Geochimica et Cosmochimica Acta* **211**, 87–109.

Ludwig, K. R. (2003). *ISOPLOT 3.00: A geochronological toolkit for Microsoft Excel. Berkeley Geochronology Center Special Publication*, http://www.bgc.org/isoplot_etc/isoplot.html.

Maboko, M. A. H. (2000). Nd and Sr isotopic investigation of the Archean–Proterozoic boundary in north eastern Tanzania: constraints on the nature of Neoproterozoic tectonism in the Mozambique Belt. *Precambrian Research* **102**, 87–98.

Manya, S. (2004). Geochemistry and petrogenesis of volcanic rocks of the Neoarchaean Sukumaland Greenstone Belt, northwestern Tanzania. *Journal of African Earth Sciences* **40**, 269–279.

Manya, S. & Maboko, M. A. H. (2003). Dating basaltic volcanism in the Neoarchaean Sukumaland Greenstone Belt of the Tanzania Craton using the Sm–Nd method: implications for the geological evolution of the Tanzania Craton. *Precambrian Research* **121**, 35–45.

Manya, S. & Maboko, M. A. H. (2008*a*). Geochemistry and geochronology of Neoarchaean volcanic rocks of the Iramba–Sekenke greenstone belt, central Tanzania. *Precambrian Research* **163**, 265–278.

Manya, S. & Maboko, M. A. H. (2008*b*). Geochemistry of the Neoarchaean mafic volcanic rocks of the Geita area, NW Tanzania: Implications for stratigraphical relationships in the Sukumaland greenstone belt. *Journal of African Earth Sciences* **52**, 152–160.

Manya, S., Kobayashi, K., Maboko, M. A. H. & Nakamura, E. (2006). Ion microprobe zircon U–Pb dating of the late Archaean metavolcanics and associated granites of the Musoma–Mara Greenstone Belt, Northeast Tanzania: Implications for the geological evolution of the Tanzania Craton. *Journal of African Earth Sciences* **45**, 355–366.

Manya, S., Maboko, M. A. H. & Nakamura, E. (2007). The geochemistry of high-Mg andesite and associated adakitic rocks in the Musoma–Mara Greenstone Belt, northern Tanzania: Possible evidence for Neoarchaean ridge subduction? *Precambrian Research* **159**, 241–259.

Markwick, A. J. W. & Downes, H. (2000). Lower crusal granulite xenoliths from the Arkhangelsk kimberlite pipes: petrological, geochemical and geophysical results. *Lithos* **51**, 135–151.

Markwick, A. J. W., Downes, H. & Veretennikov, N. (2001). The lower crust of SE Belarus: petrological, geophysical and geochemical constraints from xenoliths. *Tectonophysics* **339**, 215–237.

McDonough, W. F. & Sun, S.-s. (1995). Composition of the Earth. *Chemical Geology* **120**, 223–253.

McLaren, S., Sandiford, M., Powell, R., Neumann, N. & Woodhead, J. (2006). Palaeozoic intraplate crustal anatexis in the Mount Painter Province, South Australia: Timing, thermal budgets and the role of crustal heat production. *Journal of Petrology* **47**, 2281–2302.

Meert, L. G., van der Voo, R. & Aytib, S. (1995). Paleomagnetic investigation of the Neoproterozoic Gagwe lavas and Mbozi complex, Tanzania and the assembly of Gondwana. *Precambrian Research* **74**, 225–244.

Menzies, A., Fan, W.-M. & Zhang, M. (1993). Paleozoic and Cenozoic lithoprobes and the loss of >120 km of Archean lithosphere, Sino-Korean craton, China. In: Prichard, H. M., Alabaster, H. M., Harris, T. & Neary, C. R. (eds) *Magmatic Processes and Plate Tectonics. Geological Society, London, Special Publications* **76**, 71–81.

Mezger, K. & Krogstad, E. J. (1997). Interpretation of discordant U–Pb zircon ages: An evaluation. *Journal of Metamorphic Geology* **15**, 127–140.

Moecher, D. P. & Essene, E. J. (1991). Calculation of CO_2 activites using scapolite equilibria—constraints on the presence and composition of a fluid phase during high-grade metamorphism. *Contributions to Mineralogy and Petrology* **108**, 219–240.

Möller, A., Appel, P., Mezger, K. & Schenk, V. (1995). Evidence for a 2 Ga subduction zone: eclogites in the Usagaran belt of Tanzania. *Geology* **23**, 1067–1070.

Möller, A., Mezger, K. & Schenk, V. (2000). U–Pb dating of metamorphic minerals: Pan-African metamorphism and prolonged slow cooling of high pressure granulites in Tanzania, East Africa. *Precambrian Research* **104**, 123–146.

Morimoto, N., Fabries, J., Ferguson, A. K., Ginzburg, I. V., Ross, M., Seifert, F. A., Zussman, J., Aoki, K. & Gottardi, G. (1988). Nomenclature of pyroxenes. *American Mineralogist* **73**, 1123–1133.

Mtoro, M., Maboko, M. A. H. & Manya, S. (2009). Geochemistry and geochronology of the bimodal volcanic rocks of the Suguti area in the southern part of the Musoma–Mara Greenstone Belt, Northern Tanzania. *Precambrian Research* **174**, 241–257.

Nyblade, A. A. & Brazier, R. A. (2002). Precambrian lithospheric controls on the development of the East African rift system. *Geology* **30**, 755–758.

Nyblade, A. A., Pollack, H. N., Jones, D. L., Podmore, F. & Mushayandebvu, M. (1990). Terrestrial heat flow in East and Southern Africa. *Journal of Geophysical Research* **95**, 17371–17384.

Paslick, C., Halliday, A. N., James, D. & Dawson, J. B. (1995). Enrichment of the continental lithosphere by OIB melts; isotopic evidence from the volcanic province of northern Tanzania. *Earth and Planetary Science Letters* **130**, 109–126.

Pike, J. E. N., Meyer, C. E. & Wilshire, H. G. (1980). Petrography and chemical composition of a suite of ultramafic xenoliths from Lashaine, Tanzania. *Journal of Geology* **88**, 343–352.

Premo, W. R. & Loucks, R. R. (2000). Age and Pb–Sr–Nd isotopic systematics of plutonic rocks from the Green Mountain magmatic arc, southeastern Wyoming: Isotopic characterization of a Paleoproterozoic island arc system. *Rocky Mountain Geology* **35**, 51–70.

Downloaded from http://petrology.oxfordjournals.org/ at University of Dar es Salaam on March 8, 2016

Reid, A. M. & Dawson, J. B. (1972). Olivine–garnet reaction in peridotites from Tanzania. *Lithos* **5**, 115–124.

Reid, A. M., Donaldson, C. H., Brown, R. W., Ridley, W. I. & Dawson, J. B. (1975). Mineral chemistry of peridotite xenoliths from the Lashaine volcano, Tanzania. In: Ahrens, L. H., Dawson, J. B., Duncan, A. R. & Erlank, A. J. (eds) *Physics and Chemistry of the Earth*. Pergamon Press, pp. 525–543.

Rhodes, J. M. & Dawson, J. B. (1975). Major and trace element chemistry of peridotite inclusion from the Lashaine volcano, Tanzania. In: Ahrens, L. H., Dawson, J. B., Duncan, A. R. & Erlank, A. J. (eds) *Physics and Chemistry of the Earth*. Pergamon Press, pp. 545–557.

Ridley, W. I. & Dawson, J. B. (1975). Lithophile trace element data bearing on the origin of peridotite xenoliths, ankaramite and carbonatite from Lashaine volcano, N. Tanzania. In: Ahrens, L. H., Dawson, J. B., Duncan, A. R. & Erlank, A. J. (eds) *Physics and Chemistry of the Earth*. Pergamon Press, pp. 559–569.

Ritsema, J., Nyblade, A. A., Owens, T. J., Langston, C. A. & VanDecar, J. C. (1998). Upper mantle seismic velocity structure beneath Tanzania, East Africa: implications for the stability of cratonic lithosphere. *Journal of Geophysical Research* **103**, 21201–21214.

Rogers, N. W. (1977). Granulite xenoliths from Lesotho kimberlites and the lower continental crust. *Nature* **270**, 681–684.

Rogers, N. W. & Hawkesworth, C. J. (1982). Proterozoic age and cumulate origin for granulite xenoliths, Lesotho. *Nature* **299**, 409–413.

Rudnick, R. L. (1992). Xenoliths—Samples of the lower continental crust. In: Fountain, D. M., Arculus, R. & Kay, R. W. (eds) *Continental Lower Crust*. Elsevier, pp. 269–316.

Rudnick, R. L. & Fountain, D. M. (1995). Nature and composition of the continental crust: a lower crustal perspective. *Reviews of Geophysics* **33**, 267–309.

Rudnick, R. L. & Gao, S. (2003). The composition of the continental crust. In: Rudnick, R. L. (ed.) *The Crust*. Elsevier, pp. 1–64.

Rudnick, R. L. & Taylor, S. R. (1987). The composition and petrogenesis of the lower crust: a xenolith study. *Journal of Geophysical Research* **92**, 13981–14005.

Rudnick, R. L. & Taylor, S. R. (1991). Petrology and geochemistry of lower crustal xenoliths from northern Queensland and inferences on lower crustal composition. In: Drummond, B. (ed.) *The Eastern Australian Lithosphere. Geological Society of Australia, Special Publications* **17**, 189–208.

Rudnick, R. L., McDonough, W. F., McCulloch, M. T. & Taylor, S. R. (1986). Lower crustal xenoliths from Queensland, Australia: evidence for deep crustal assimilation and fractionation of continental basalts. *Geochimica et Cosmochimica Acta* **50**, 1099–1115.

Rudnick, R. L., McDonough, W. F. & Chappell, B. W. (1993). Carbonatite metasomatism in the northern Tanzanian mantle: petrographic and geochemical characteristics. *Earth and Planetary Science Letters* **114**, 463–476.

Rudnick, R. L., McDonough, W. F. & Orpin, A. (1994). Northern Tanzanian peridotite xenoliths: a comparison with Kaapvaal peridotites and inferences on metasomatic interactions. In: Meyer, H. O. A. & Leonardos, O. (eds) *Kimberlites, Related Rocks and Mantle Xenoliths, Vol. 1 (Proceedings of the Fifth International Kimberlite Conference)*. CPRM, pp. 336–353.

Rudnick, R. L., Ireland, T. R., Gehrels, G., Irving, A. J., Chesley, J. T. & Hanchar, J. M. (1999). Dating mantle metasomatism: U–Pb geochronology of zircons in cratonic mantle xenoliths from Montana and Tanzania. In: Gurney, J. J., Gurney, J. L., Pascoe, M. D. & Richardson, S. R. (eds) *Proceedings of the VIIth International Kimberlite Conference*. Red Roof Design, pp. 728–735.

Sanislav, I. V., Wormald, R. J., Dirks, P. H. G. M., Blenkinsop, T. G., Salamba, L. & Joseph, D. (2014). Zircon U–Pb ages and Lu–Hf isotope systematics from last-tectonic granites, Geita greenstone belt: implications for crustal growth of the Tanzania craton. *Precambrian Research* **242**, 187–204.

Schmitz, M. D. & Bowring, S. A. (2000). The significance of U–Pb zircon dates in lower crustal xenoliths from the southwestern margin of the Kaapvaal craton, southern Africa. *Chemical Geology* **172**, 59–76.

Schmitz, M. D. & Bowring, S. A. (2003*a*). Constraints on the thermal evolution of continental lithosphere from U–Pb accessory mineral thermochronometry of lower crustal xenoliths, southern Africa. *Contributions to Mineralogy and Petrology* **144**, 592–618.

Schmitz, M. D. & Bowring, S. A. (2003*b*). Ultrahigh-temperature metamorphism in the lower crust during Neoarchean Ventersdorp rifting and magmatism, Kaapvaal Craton, Southern Africa. *Geological Society of America Bulletin* **115**, 533–548.

Shatsky, V. S., Buzlukova, L. V., Jagoutz, E., Koz'menko, O. A. & Mityukhin, S. I. (2005). Structure and evolution of the lower crust of the Daldyn–Alakit district in the Yakutian Diamond Province (from data on xenoliths). *Russian Geology and Geophysics* **46**, 1252–1270.

Shervais, J. W. (1982). Ti–V plots and the petrogenesis of modern and ophiolitic lavas. *Earth and Planetary Science Letters* **59**, 101–118.

Sommer, H., Kroner, A., Hauzenberger, C., Muhongo, S. & Wingate, M. T. D. (2003). Metamorphic petrology and zircon geochronology of high-grade rocks from the central Mozambique Belt of Tanzania: crustal recycling of Archean and Palaeoproterozoic material during the Pan-African orogeny. *Journal of Metamorphic Geology* **21**, 915–934.

Stern, R. J. (1994). Arc assembly and continental collision in the Neoproterozoic East African Orogen: implications for the consolidation of Gondwanaland. *Annual Review of Earth and Planetary Sciences* **22**, 319–351.

Stipska, P. & Powell, R. (2005). Does ternary feldspar constrain the metamorphic conditions of high-grade meta-igneous rocks? Evidence from orthopyroxene granulites, Bohemian Massif. *Journal of Metamorphic Geology* **23**, 627–647.

Sun, S.-s. & McDonough, W. F. (1989). Chemical and isotopic systematics of oceanic basalts: Implications for mantle composition and processes. In: Saunders, A. D. & Norry, M. J. (eds) *Magmatism in the Ocean Basins. Geological Society, London, Special Publications* **42**, 313–345.

Tenczer, V., Hauzenberger, C. A., Fritz, H., Whitehouse, M. J., Mogessie, A., Wallbrecher, E., Muhongo, S. & Hoinkes, G. (2006). Anorthosites in the Eastern Granulites of Tanzania—New SIMS zircon U–Pb age data, petrography and geochemistry. *Precambrian Research* **148**, 85–114.

Tenczer, V., Hauzenberger, C., Fritz, H., Hoinkes, G., Muhongo, S. & Klötzli, U. (2014). Crustal age domains and metamorphic reworking of the deep crust in Northern–Central Tanzania: a U/Pb zircon and monazite age study. *Mineralogy and Petrology* **107**, 679–707.

Thomas, R. J., Roberts, N. M. W., Jacobs, J., Bushi, A. M., Horstwood, M. S. A. & Mruma, A. (2013). Structural and geochronological constraints on the evolution of the eastern margin of the Tanzania Craton in the Mpwapwa area, central Tanzania. *Precambrian Research* **224**, 671–689.

Tugume, F., Nyblade, A. A. & Julia, J. (2012). Moho depths and Poisson's ratios of Precambrian crust in East Africa: Evidence for similarities in Archean and Proterozoic crustal structure. *Earth and Planetary Science Letters* **355–356**, 73–81.

Vauchez, A., Dineur, F. & Rudnick, R. (2005). Microstructure, texture and seismic anisotropy of the lithospheric mantle above a mantle plume: Insights from the Labait volcano xenoliths (Tanzania). *Earth and Planetary Science Letters* **232**, 295–314.

Downloaded from http://petrology.oxfordjournals.org/ at University of Dar es Salaam on March 8, 2016

Weeraratne, D. S., Forsyth, D. W., Fischer, K. M. & Nyblade, A. A. (2003). Evidence for an upper mantle plume beneath the Tanzanian craton from Rayleigh wave tomography. *Journal of Geophysical Research—Solid Earth* **108**, 19, doi: 10.1029/2002JB002273.

Wiedenbeck, M., Alle, P., Corfu, F., Griffin, W. L., Meier, M., Oberli, F., Vonquadt, A., Roddick, J. C. & Speigel, W. (1995). Three natural zircon standards for U–Th–Pb, Lu–Hf, trace-element and REE analyses. *Geostandards Newsletter* **19**, 1–23.

Yu, J. H., Xu, X. S., O'Reilly, S. Y., Griffin, W. L. & Zhang, M. (2003). Granulite xenoliths from Cenozoic basalts in SE China provide geochemical fingerprints to distinguish lower crust terranes from the North and South China tectonic blocks. *Lithos* **67**, 77–102.

Zartman, R. E., Kempton, P. D., Paces, J. B., Downes, H., Williams, I. S., Dobosi, G. & Futa, K. (2013). Lower-crustal xenoliths from Jurassic kimberlite diatremes, Upper Michigan (USA): Evidence for Proterozoic orogenesis and plume magmatism in the lower crust of the southern Superior Provice. *Journal of Petrology* **54**, 575–608.

Zheng, J. P., Sun, M., Lu, F. X. & Pearson, N. (2003). Mesozoic lower crustal xenoliths and their significance in lithospheric evolution beneath the Sino-Korean Craton. *Tectonophysics* **361**, 37–60.

Downloaded from http://petrology.oxfordjournals.org/ at University of Dar es Salaam on March 8, 2016